[redacted]

UNCLASSIFIED

SLA-73-0565

~~Specified External Distribution Only~~

[redacted]

RS 3150 2450
THIS DOCUMENT CONTAINS
146 PAGES, COPY NO. 138
OF 138 COPIES, SERIES A
FOR DRC 3141-1

Test Report for SAMS Rain-Erosion Flights 3, 4, and 5 (U)

J. K. Cole, H. W. Church, B. W. Marshall, L. R. Rollstin

[redacted]

SANDIA SYSTEMATIC DECLASSIFICATION REVIEW	
1st Review Date: 3-06-96 Authority: ☐ ADC ☒ ADD Name: W. Layer 2nd Review Date: 3/28/96 Authority: ADD Name: RBCrawn	Determination (Circle Numbers): 1. Classification Retained 2. Classification Changed to: U 3. Contains No DOE Classified Information 4. Coordinate With: 5. Contains UCNI? 6. Comments: Input to Operator

Sandia Laboratories

SF 2900 QA(7-73)

UNCLASSIFIED

[redacted]

RECORD COPY
DO NOT TAKE FROM THIS ROOM
MICROFICHE

[redacted]

UNCLASSIFIED

Issued by Sandia Laboratories, a prime contractor to the United States Atomic Energy Commission

---

NOTICE

This report was prepared as an account of work sponsored by the United States Government. Neither the United States nor the United States Atomic Energy Commission, nor any of their employees, nor any of their contractors, subcontractors, or their employees, makes any warranty, express or implied, or assumes any legal liability or responsibility for the accuracy, completeness or usefulness of any information, apparatus, product or process disclosed, or represents that its use would not infringe privately owned rights.

UNCLASSIFIED

[redacted]

[redacted]

UNCLASSIFIED

SLA-73-0565

TEST REPORT FOR SAMS RAIN-EROSION FLIGHTS 3, 4, AND 5 (U)

RS 3150/2450

J. K. Cole, H. W. Church, and B. W. Marshall
Geophysical Fluid Dynamics Division 5644
L. R. Rollstin
Rocket Systems Division 5624

Printed October 1973

ABSTRACT (U)

Sandia Laboratories and SAMSO are cosponsoring the SAMS Program to experimentally determine the effects of naturally occurring cloud and precipitation particles upon high-speed vehicles. In 1972 three Terrier-Recruit rocket vehicles carrying carbon phenolic nosetips and forward heatshields were launched into storms at the NASA Range, Wallops Island, Virginia. All of the vehicles performed satisfactorily, except for the malfunction of the recession gage on one test. Each payload was recovered from the ocean. Meteorological samplings of each storm were made by the Meteorology Research Incorporated instrumented aircraft, the Joint Air Force/NASA weather radars and other ground-based instruments. AFCRL directed all of the meteorological sampling and its subsequent reduction and interpretation. This report presents the complete data for each flight test, including measured surface recessions and roughness, trajectory and telemetry data and meteorology data. An analysis is made to determine the significance of the observed stagnation and sidewall recessions.

A general summary is presented at the beginning of the report.

[redacted]

[redacted]

UNCLASSIFIED

[redacted]

[redacted]

UNCLASSIFIED

(Intentionally left blank)

UNCLASSIFIED

[redacted]

[redacted]

UNCLASSIFIED

ACKNOWLEDGEMENTS

This project has demanded extra effort and care and special attention by all who have been involved. Special techniques and hardware had to be developed and/or procured on very short time scales. These hurry-up activities were then followed by the inevitable waits for the proper launch conditions at Wallops Island.

The Sandia personnel, other than the authors, who have made significant contributions to the FY73 SAMS Program are:

R. D. Robinett, 9485	Program Coordination and Assistant Test Director
J. J. Bahlman, 5623 J. P. Gallagher, 5623 R. D. Fellerhoff, 5623 E. C. Rightley, 5623	Vehicle Mechanical Design and Assembly
D. W. Johnson, 5626	Recovery System
G. J. Hochrein, 5644	Analysis
J. W. Reed, 5644	Meteorological Support
R. H. Lanes, 9483 K. W. Shrock, 9483 L. P. Billmaier, 1235	Telemetry Design and Assembly
W. C. Riggan, 2411 G. F. Wright, 5628	Nosetip Recession Instrumentation
R. C. Scharrer, 9421 N. E. Corlis, 9421	Tape Recording System for Weather Radar
J. C. Reynolds, 9425	Data Reduction
W. C. Gaines, 3311	Health Physics

Further, we wish to also recognize the persons from other agencies or companies who have contributed significantly to this program:

R. M. Cunningham V. G. Plank K. R. Hardy K. Glover G. Armstrong	Air Force Cambridge Research Laboratory
D. C. Glenn	Aerospace Corporation
Lt. R. Might Maj. R. Rene	SAMSO-ABRES

UNCLASSIFIED

[redacted]

[redacted]

UNCLASSIFIED

J. C. Howard	JAFNA Radar Facility
A. Oliveras L. Boardman	Meteorology Research Inc.
R. T. Long R. S. Nock	NASA Wallops
C. M. Boettger J. M. Bauman	NOAA Weather Station

[redacted]

UNCLASSIFIED

[redacted]

CONTENTS

	Page
1. Summary	15
2. Introduction	17
2.1 Objective	17
2.2 Background	17
3. Vehicle 3 Flight Test	19
3.1 Sequence of Events	19
3.2 Meteorological Summary	21
3.3 Vehicle Performance	21
3.4 Surface Recession	22
4. Vehicle 4 Flight Test	27
4.1 Sequence of Events	27
4.2 Meteorological Summary	30
4.3 Vehicle Performance	31
4.4 Surface Recession	31
5. Vehicle 5 Flight Test	36
5.1 Sequence of Events	36
5.2 Meteorological Summary	38
5.3 Vehicle Performance	39
5.4 Surface Recession	39
6. Discussion	44
6.1 Accuracy of Measurements	44
6.1.1 Radar Tracking Data	44
6.1.2 Payload Prime Instruments	44
6.1.3 Meteorological Data	45
6.2 Nosetip Recession	45
6.3 Sidewall Recession	52
7. Conclusions	56

[redacted]

[redacted]

CONTENTS (CONT)

	Page
Appendix A. Support Functions and Facilities	57
A.1 Meteorological Support	59
A.1.1 NOAA Weather Station	59
A.1.2 Weather Radars	59
A.1.3 Sampler Aircraft	60
A.1.4 Ground-Based Instruments	60
Appendix B. Terrier-Recruit Rocket System	65
B.1 System Description	67
B.2 Aerodynamics	68
B.3 Payload	68
B.3.1 General	68
B.3.2 Payload Instrumentation and Related Systems	69
B.3.2.1 Payload Telemetry	69
B.3.2.2 Payload Beacon	70
B.3.2.3 Payload Antenna	71
B.3.2.4 Recession Instrumentation	71
B.3.3 Recovery System	71
Appendix C. Erosion Data, Vehicle 3	73
C.1 Meteorological Data	75
C.2 Vehicle 3 Performance	79
C.3 Telemetry Measurements	87
Appendix D. Erosion Data, Vehicle 4	93
D.1 Meteorological Data	95
D.2 Vehicle 4 Performance	100
D.3 Telemetry Measurements	107
Appendix E. Erosion Data, Vehicle 5	113
E.1 Meteorological Data	115
E.2 Vehicle 5 Performance	120
E.3 Telemetry Measurements	128

[redacted]

CONTENTS (CONT)

		Page
Appendix F.	Precipitation Particle Size Distributions	133
Appendix G.	Comparison of Reduced Weather Radar Data	139
Bibliography		142

[redacted]

(Intentionally left blank)

[redacted]

[redacted]

FIGURES

Figure		Page
3.2.1	Preliminary Liquid-Water Content Versus Altitude, Vehicle 3	22
3.4.1	Nosetip Installation of ^{182}Ta Source Positions, Typical for All Vehicles	23
3.4.2	Nosetip Recession, Vehicle 3	23
3.4.3	Nosetip Profile and Sidewall Roughness, Vehicle 3	24
3.4.4	Photographs of Nosetip, Vehicle 3	25
3.4.5	Heatshield Recession, Vehicle 3	26
3.4.6	Heatshield Sidewall Roughness, Vehicle 3	26
4.1.1	JAFNA S-Band Radar RHI Contoured Scan, 0956 EST, February 17, 1972	28
4.1.2	JAFNA S-Band Radar RHI Contoured Scan, 1012 EST, February 17, 1972	29
4.2.1	Preliminary Liquid-Water Content Versus Altitude, Vehicle 4	30
4.4.1	Stagnation Point Recession, Vehicle 4	32
4.4.2	Nosetip Recession, Vehicle 4	32
4.4.3	Nosetip Profile and Sidewall Roughness, Vehicle 4	33
4.4.4	Photographs of Nosetip, Vehicle 4	34
4.4.5	Heatshield Recession, Vehicle 4	35
4.4.6	Heatshield Sidewall Roughness, Vehicle 4	35
5.1.1	JAFNA-S-Band Radar RHI Contoured Scan, 1047 EST, March 22, 1972	37
5.2.1	Preliminary Liquid-Water Content Versus Altitude, Vehicle 5	38
5.4.1	Stagnation Point Recession, Vehicle 5	40
5.4.2	Nosetip Recession, Vehicle 5	40
5.4.3	Nosetip Profile and Sidewall Roughness, Vehicle 5	41
5.4.4	Photographs of Nosetip, Vehicle 5	42
5.4.5	Heatshield Recession, Vehicle 5	43
5.4.6	Heatshield Sidewall Roughness, Vehicle 5	43
6.2.1	Calculated Surface Conditions and Stagnation Recession, Vehicle 4	46
6.2.2	Calculated Surface Conditions and Stagnation Recession, Vehicle 5	46
6.2.3	Material Temperatures, Vehicle 4	47
6.2.4	Material Temperatures, Vehicle 5	47
6.2.5	Material Densities, Vehicle 4	48
6.2.6	Material Densities, Vehicle 5	48
6.3.1	Sidewall Recession	52
6.3.2	Sidewall Recession Normalized by Stagnation Recession	53
A.1.4	Map of NASA Wallops	62
B.1	Terrier-Recruit Rocket System	67
B.2	Instrumented Payload [redacted]	69
B.3	Payload Recovery System	72

[redacted]

FIGURES (CONT)

Figure		Page
C.1.1	Three Hourly Surface Weather Charts, February 3	75
C.1.2	Rain Rate Versus Time, Weighing Gages, February 3	76
C.1.3	Rain Rate Versus Time, Tipping-Bucket Gage, February 3	77
C.1.4	Rawinsonde Observation, February 3	77
C.1.5	Radar-Reflected Power Profile, February 3	78
C.1.6	Contoured Reflected Power RHI, February 3	78
C.1.7	Equivalent Liquid-Water Content Profile, February 3	79
C.2.1	Velocity Versus Time, Vehicle 3	81
C.2.2	Altitude Versus Time, Vehicle 3	82
C.2.3	Altitude-Velocity Profile, Vehicle 3	83
C.2.4	Altitude-Distance Profile, Vehicle 3	83
C.2.5	Plan Position Track, Vehicle 3	84
C.3.1	Longitudinal Acceleration Versus Time, Vehicle 3	88
C.3.2	Stagnation Point Recession Versus Time, Vehicle 3	90
C.3.3	Telemetry Signal Strength Versus Time, Vehicle 3	92
D.1.1	Three Hourly Surface Weather Charts for February 17	95
D.1.2	Rain Rate Versus Time, Weighing Gages, February 17	96
D.1.3	Rain Rate Versus Time, Tipping-Bucket Gage, February 17	97
D.1.4	Rawinsonde Observation, February 17	98
D.1.5	Radar Reflected Power Profile, February 17	98
D.1.6	Contoured Reflected Power RHI, February 17	99
D.1.7	Equivalent Liquid-Water Content Profile, February 17	99
D.2.1	Velocity Versus Time, Vehicle 4	101
D.2.2	Altitude Versus Time, Vehicle 4	102
D.2.3	Altitude-Velocity Profile, Vehicle 4	103
D.2.4	Altitude-Distance Profile, Vehicle 4	103
D.2.5	Plan Position Track, Vehicle 4	104
D.3.1	Longitudinal Acceleration Versus Time, Vehicle 4	107
D.3.2	Stagnation Point Recession Versus Time, Vehicle 4	109
D.3.3	Telemetry Signal Strength Versus Time, Vehicle 4	112
E.1.1	Three Hourly Surface Weather Charts for March 22	115
E.1.2	Rain Rate Versus Time, Weighing Gages, March 22	116
E.1.3	Rain Rate Versus Time, Tipping Bucket Gages, March 22	117
E.1.4	Rawinsonde Observation, March 22	118
E.1.5	Radar Reflected Power Profile, March 22	118
E.1.6	Contoured Reflected Power RHI, March 22	119
E.1.7	Equivalent Liquid-Water Content Profile, March 22	119

[redacted]

[redacted]

FIGURES (CONT)

Figure		Page
E.2.1	Velocity Versus Time, Vehicle 5	120
E.2.2	Altitude Versus Time, Vehicle 5	122
E.2.3	Altitude-Velocity Profile, Vehicle 5	123
E.2.4	Altitude-Distance Profile, Vehicle 5	124
E.2.5	Plan Position Track, Vehicle 5	125
E.3.1	Longitudinal Acceleration Versus Time, Vehicle 5	129
E.3.2	Stagnation Point Recession Versus Time, Vehicle 5	130
E.3.3	Telemetry Signal Strength Versus Time, Vehicle 5	131
F.1	Cumulative Mass Versus Size for Rain Drops	137
F.2	Cumulative Mass Versus Size for Snow Flakes	137
F.3	Cumulative Mass Versus Size for Ice Crystals	138

[redacted]

[redacted]

TABLES

Table		Page
4.4.1	Stagnation Point Recession, Vehicle 4	31
5.4.1	Stagnation Point Recession, Vehicle 5	39
6.2.1	Effective Erosion Coefficients Versus Time	51
6.2.2	Test Parameters at Times of Source Removals	51
6.2.3	Erosion Coefficients for Total Stagnation Recession	51
6.3.1	Effective Erosion Coefficients for Sidewall Recession	54
6.3.2	Effective Sidewall Erosion Coefficients, Flight 4	55
A.1	NASA/Wallops Support Facilities	63
B.1	Telemetry Channel Assignments	70
C.2.1	Vehicle Performance Summary for Vehicles 3, 4, and 5	80
C.2.2	Vehicle 3 Trajectory Data	85
D.2.1	Vehicle 4 Trajectory Data	105
E.2.1	Vehicle 5 Trajectory Data	126
F.1	List of Parameters for Particle Size Distributions	136

[redacted]

[redacted]

TEST REPORT FOR SAMS RAIN-EROSION FLIGHTS 3, 4, AND 5 (U)

1.0 Summary

Sandia Laboratories and the Air Force Space and Missile Systems Organization (SAMSO) are cosponsoring the SAMS (Sandia/Air Force Materials Study) Program to experimentally determine the impact effects of naturally occurring cloud/precipitation particles upon high-speed vehicles.

Vehicle 0, the first Terrier-Recruit rocket vehicle carrying a carbon-phenolic nosetip and forward heatshield, was flown through clear air in October 1970. The stagnation recession observed was 6.9 mm (0.27 inches). Essentially no sidewall recession was measured.

On March 15, 1971, Vehicle 1 was launched into a squall-line storm with a ground-rain rate of 7-21 mm/hr. The nosetip lost 10.1-10.4 cm (4.0-4.1 inches) at the stagnation point and over 3.5 mm (0.14 inches) on the sidewalls. Vehicle 2, launched on March 26, 1971, encountered a snowstorm with an equivalent ground-rain rate of 0.7-0.9 mm/hr and experienced more than 2.5 cm (1.0 inch) of stagnation recession. The payload of Vehicle 2 was lost in the ocean. These two tests through storms concluded the 1971 test series.

The 1972 series began with the launch of Vehicle 3 into a widespread storm with a ground-rain rate of 1-2 mm/hr on February 3. The vehicle performance was nominal, with the maximum velocity of 2.608 km/sec (8556 fps) occurring at 6.22 seconds. The tracking data were satisfactory, but the telemetered nosetip recession data exhibited severe signal shifts which eliminated most of the recession-vs-time data. The payload was recovered. The stagnation recession was 1.93 cm (0.76 inches), and the maximum sidewall recession was 1.07 mm (0.042 inches).

Vehicle 4 was launched on February 17, 16 minutes after a vehicle carrying an ATJ-S graphite nosetip. The ground-rain rate within ±5 minutes of the Vehicle 4 launch was 2.5-4.5 mm/hr. The vehicle performance was nominal with the maximum velocity of 2.585 km/sec (8482 fps) achieved 6.73 seconds after launch. The tracking and telemetry data were satisfactory and the payload was recovered. The measured recessions were 2.82 cm (1.11 inches) at the stagnation point and a maximum of 1.88 mm (0.074 inches) on the sidewalls.

Vehicle 5, the last vehicle of the 1972 series, was launched on March 22 in the leading part of a widespread storm. Within ±5 minutes of launch, the rain rate varied from 0.3 to 15 mm/hr. The vehicle performed nominally, achieving a maximum velocity of 2.570 km/sec (8431 fps) at 6.60 seconds. The tracking and telemetry data were satisfactory and the payload was recovered. The stagnation recession was 3.02 cm (1.19 inches) and the maximum sidewall recession was 2.16 mm (0.085 inches).

Each storm was sampled by the Meteorology Research Incorporated (MRI) instrumented Piper Aztec aircraft, the Joint Air Force/NASA (JAFNA) S-band weather radar and other ground-based instruments. The Air Force Cambridge Research Laboratory (AFCRL) directed the meteorological sampling of each storm and was responsible for its subsequent reduction and interpretation.

[redacted]

[redacted]

Aerothermal calculations were made for Vehicles 4 and 5 where the complete recession history data were available. These showed that the surface material in the nosetip stagnation region of both vehicles attained temperatures in excess of 1250°C (2280°F); however, because of insufficient time for charring to occur, material densities remained near their virgin values throughout the erosion period.

The Vehicle 4 and 5 data were further studied using the SPLAT impact erosion code and empirical erosion models where the mass loss was proportional to the particle impact velocity raised to the 2.0, 2.5, 3.0, and 3.5 powers. With each model the effective erosion coefficients required to match the observed recessions increased with time from launch. A brief examination of other flight parameters suggested that these erosion-coefficient increases may possibly correlate with the material temperatures near the surface or the type of particles impacting (i.e., rain, snow, ice). SPLAT erosion calculations to obtain the total observed stagnation recessions, assuming the mass loss to be proportional to the particle kinetic energy, required erosion coefficients of 4.7-6.5, 6.4-8.2 and 5.8-7.4 g/kJ respectively for Vehicles 3, 4, and 5.

The sidewall recessions were measured on the nosetip and heatshield of each vehicle. Comparisons of these data normalized by the respective stagnation recession produced some interesting results. For the nosetip sidewall, the Vehicle 5 recession was approximately twice that of Vehicles 3 and 4. It was immediately suspected that these differences could have resulted from differences in the particle size and type distributions in the storms or from differences in the material properties. Subsequent comparisons of the normalized heatshield sidewall recessions indicated a different ordering where the Vehicle 3 data were approximately 70 percent of those for Vehicles 4 and 5. This change in ordering suggested that these nosetip and heatshield differences must be caused primarily by differences in the material properties.

SPLAT calculations of the sidewall recessions, assuming the mass removal to be proportional to the particle kinetic energy and the sine of the impact angle, required erosion coefficients of 6.2-17.8 g/kJ to produce the nosetip sidewall data. On the heatshield these coefficients increased to values of 26.9-45.1 g/kJ. Assuming higher powers of the velocity or of the sine of the impact angle in the erosion model does not resolve these larger differences between the nosetip and heatshield recessions. These differences appear to result from the material construction. The inverted-chevron construction used in the nosetip is apparently more erosion resistant than the shingle-wrap construction of the heatshield.

[redacted]

[redacted]

2.0 Introduction

2.1 Objective

The objective of the SAMS program is to experimentally determine the effects of high-speed impacts on naturally occurring cloud/precipitation particles upon full-scale missile nosetip and heatshield materials.

2.2 Background

As described by Cole (1970), Sandia Laboratories and the Air Force Space and Missile Systems Organization (SAMSO) are cosponsoring the SAMS Program in which instrumented, high-speed rocket vehicles carrying full-scale missile hardware are flown through naturally occurring storm environments at the NASA Range, Wallops Island, Virginia. These natural environments are measured by an instrumented aircraft, by ground meteorological instruments and by the weather radars of the Joint Air Force/NASA (JAFNA) facility. The Air Force Cambridge Research Laboratory (AFCRL) is responsible for the meteorological measurements and their interpretation.

The NASA Range, Wallops Island, was selected for the SAMS Program because it exhibits a relatively frequent occurrence of the desired storm environments, possesses the support facilities required and is readily accessible geographically. Appendix A provides a detailed description of the support function and facilities at NASA Wallops.

The Terrier-Recruit two-stage, solid-propellant rocket vehicle and its instrumented payload were designed and developed by Sandia to achieve a maximum speed of 2.6-2.7 kilometers per second (8500-8900 kfps) at an altitude around 3.0 km (10.0 kft) msl with a 29.5-kilogram (65-lb) payload. The particle impact erosion experiment is performed during the ascent portion of the trajectory and the payload is subsequently recovered from the ocean by means of a parachute/flotation-bag system. Appendix B provides a detailed description of the rocket-vehicle system.

The SAMS Program began in August 1969. Two structural flight tests of the Terrier-Recruit (TR) vehicles were conducted at the Sandia Tonopah Test Range, Nevada, in the summer of 1970. A combination structural and clear-air recession test of a carbon-phenolic nosetip and front heatshield was successfully conducted at the Barking Sands Range, Kauai, Hawaii in October 1970. The measured stagnation point recession was 6.9 mm (0.27 inch).

Five TR vehicles were constructed for flight tests with carbon-phenolic nosetips and front heatshields at NASA Wallops during the winter storm period, January-March 1971. Only two of these vehicles were launched in this period. On March 15, 1971, the first vehicle intercepted a storm associated with the squall line of a rapidly moving, weak cold front. The ground precipitation rate varied between 7-21 mm/hr (0.3-0.8 in/hr) within ±5 minutes of the launch time.

The payload, including the nosetip and front heatshield, was recovered from the ocean, and the measured stagnation point recession was 10.1-10.4 centimeters (4.0-4.1 inches).

The second vehicle was launched into a widespread snowstorm on March 26, 1971. The ground precipitation rate was 0.7-0.9 mm/hr (0.03-0.04 in/hr) within ±5 minutes of the launch. The telemetry indicated that the stagnation point recession was in excess of 2.5 centimeters (1.0 inch). The

[redacted]

[redacted]

payload sank in the ocean shortly after impact, and subsequent searches were unable to locate it. The data for both of these flight tests are discussed by Cole and Robinett (1971).

[redacted]

3.0 Vehicle 3 Flight Test [redacted]

3.1 Sequence of Events

Vehicle 3 was launched into a storm at 1317 hours EST on Thursday, February 3, 1972. This flight test is designated by Sandia test number R341403 and NASA Wallops Number Q2-5297.

The launch period for the 1972 SAMS program began on January 11, 1972, at the NASA Wallops Range. Vehicle 3, carrying a carbon-phenolic nosetip and front heatshield, was mounted on the Atlantic Research Corporation (ARC) launcher at Pad 0. The ARC launcher was enclosed in a heated mobile shelter which was removed shortly before a launch attempt.

Storms which were marginally acceptable in rainrate and total cloud thickness occurred on January 11 and 13. The departure of the AFCRL C130 sampling aircraft from its home base, L. G. Hanscom Field, was delayed on January 11 by fog and on January 13 by mechanical difficulties. In each instance the storm intensity became unacceptable before the C130's arrival, and the launch attempt was cancelled.

On January 14 NASA permitted the range to start at 0500 EST in anticipation of the passage of a cold front around 1200. At the 0510 weather briefing, it was announced that the weather front and its associated storm system had accelerated and passed Wallops around 0330. The C130 arrived on schedule around 0830 and performed practice sampling runs and coordinated tests with the JAFNA radars in the remaining clouds.

The next acceptable storm reached Wallops on January 20. The C130 aircraft was preparing to support the SAMS Program in this storm when a fuel leak was discovered in one of the main wing tanks. The launch attempt was again cancelled. Since the AFCRL maintenance personnel estimated that the fuel tank would require at least 4 days to repair, the SAMS launch team returned to their respective homes. By January 25, a more thorough assessment of the C130 problem indicated the need for extensive repair at a depot, requiring 50-60 days.

The sampler aircraft is an essential element of each rain-erosion flight test, and the loss of the C130 threatened the complete cancellation of the 1972 flight test program. A search was begun immediately by SAMSO-ABRES and Aerospace Corporation personnel to find a suitable replacement aircraft. Fortunately, the Defense Nuclear Agency (DNA), then involved in airborne sampling for another project, was able to loan the services of a Meteorology Research, Inc. (MRI) sampler aircraft during the interim period required by SAMSO to contract for similar services. Thus, after only a week's delay, the launch team returned to Wallops on January 31. The MRI aircraft, a Piper Aztec, arrived at Wallops on February 1. The MRI crew decided to base their Aztec at Wallops Station and spent February 2 reading their equipment.

On February 3, the 0810 weather briefing at Wallops Station indicated a possibility of rain showers in the area beginning in the late morning. A launch attempt was scheduled for 1100 by NASA. By 1030 the Patuxent weather radar indicated that the storm was becoming less intense. Subsequent horizontal PPI scans with the ASR-7 (an S-band radar recently installed at Wallops Station) and the JAFNA S-band radar showed practically no returns within 97 km (60 miles) of Wallops. The launch time was then rescheduled for 1400.

[redacted]

At 1230 an NOAA observer alerted us that the Patuxent radar was exhibiting a strong return from a storm system 80 km (50 miles) to the WSW of Wallops. Its speed suggested that it would pass over Wallops by 1400-1430. The MRI Aztec was requested to take off by 1300. The ceiling was about 300 m (1000 ft), with a moderate rain.

The Aztec cleared Wallops Station at 1320 and immediately experienced large water leaks around the front windscreen. These leaks caused the prime aircraft radio to fail. The pilot continued the climb and switched to the backup radio. At an altitude of 2.3 km (7.5 kft) the backup radio also began to malfunction, so the Aztec returned to Wallops Station, landing at 1345. The launch countdown was stopped and recycled to T-20 minutes.

The aircraft was moved into a hanger and the MRI crew, assisted by NASA technicians, began to repair the leaking windshield and the radios. In less than an hour the windshield had been sealed and the radios returned to operational status by drying with heat guns. At 1450, the aircraft took off again and was directed to climb toward an altitude of 6.1 km (20.0 kft) while maintaining a racetrack holding pattern to the east of the south end of Assateague Island. The count was resumed at 1455.

The storm was monitored with the JAFNA S-band radar scanning over an elevation angle range of 0°-30° along the 145°T launching azimuth in RHI mode and occasionally performing a horizontal PPI scan. The RHI and PPI outputs from this radar were processed by the AFCRL contour integrator and displayed on cathode ray tubes for nearly real-time evaluation of the storm dimensions, homogeneity and intensity. The raw video data from this radar were stored also for selected scans via the photographic recording of A-scope traces and use of a video-tape recording machine. The SPANDAR S-band radar scanned the storm with a fixed azimuth, 146°T, and elevation angles of 5° and 20°. The reflectivities-versus-range A-scope measurements were displayed via an x-y plotter.

The decision to launch was made after evaluating these radar data and the continuous output from the tipping-bucket rain gage situated 150-200 m (500-660 ft) to the east of the JAFNA radar. A short hold in the countdown was made at T-1 minute to obtain a final check of the meteorological data. The tipping-bucket rain gage indicated a precipitation rate of 0.7-0.8 mm/hr (0.027-0.031 in/hr). The count was resumed and the launch occurred at 1517 EST.

The Aztec aircraft had reached an altitude of 4.5 km (15.0 kft) in the holding pattern by 1520. It was directed to proceed at 4.6 km (15.0 kft) out to the reference point K, the far end of the sampling pattern, and to make measurements enroute. The sampling pattern extended from 3 km (2 miles) to 16 km (10 miles) from the launcher along the 146°T azimuth. Level sampling runs were completed by 1615 for altitudes of 4.6 km (15 kft), 3.0 km (10.0 kft), 1.5 km (5.0 kft) and 0.3 km (1 kft). The aircraft was then requested to climb to 6.1 km (20.0 kft) to complete the sampling, but it could not do so because the climb would have jeopardized its fuel-supply safety margin. The aircraft then made two unsuccessful attempts to land at Wallops Station where the ceiling was around 61 m (200 feet), with visibilities of less than a mile. It was then given clearance to proceed to Norfolk, Virginia, where it landed around 1815.

The NASA C-54 aircraft which had been maintaining radar surveillance of the test area developed engine trouble shortly before the launch and was granted permission to land at Wallops Station. The weather prevented this landing, however, and it eventually landed at Atlanta, Georgia.

[redacted]

This C-54 departed the area before it could survey the impact zone to detect the radio beacon signal. After considerable discussion, it was decided not to send the second NASA C-54 out to search for the beacon signal that night, since it might not be able to return to Wallops Station either; the absence of both C-54's from Wallops would prevent the search and recovery operation scheduled for the next morning.

Preliminary examinations of the telemetry and tracking data indicated that everything had functioned normally except for the nosetip recession instrument. Output from this instrument showed gain shifts dependent upon the vehicle acceleration.

On Friday, February 4, the recovery operation began at 0600 and the NASA C-54 was airborne by 0715. The C-54, directed toward the impact zone, soon detected a signal at the proper carrier frequency. The signal was noisy and did not exhibit the normal amplitude modulation characteristics of the beacon. A position fix, about 6.4 km (21.0 kft) east of the impact point, was rapidly obtained on the source. The recovery helicopter was vectored to this location, where the flotation bag was visually identified. The payload was later recovered by the helicopter crew and returned to Wallops Station by 0900.

The unit was found sufficiently radioactive to warrant special handling procedures. It was then loaded into a bag and transported to the Wallops Island assembly area where it was flushed with fresh water. An examination of the radio beacon system revealed that near exhaustion of the batteries had caused the abnormal beacon signal. The payload was then packaged for shipment to Sandia Laboratories.

3.2 Meteorological Summary

The widespread storm over Wallops Island on February 3, 1972, was the result of a mass of warm, moist Gulf air being forced up over a polar air mass. Rain began falling at Wallops Island around 1300 EST and continued at a relatively constant rate of 2 mm/hr (0.08 in/hr) during the two hours before launch time. The AFCRL radar data indicated cloud tops up to 7.0 km (23.0 kft) and a melt level around 2.7 km (9.0 kft). Measurements of the storm were made both by the S-band radars and the MRI Aztec aircraft. Figure 3.2.1 presents the preliminary liquid-water content, LWC, along the vehicle trajectory versus height determined by Cunningham and Plank (1972). A more detailed description of the meteorological data is presented in Appendix C.1.

3.3 Vehicle Performance

The performance of the Terrier-Recruit booster system was nearly nominal during the flight test of Vehicle 3. The first-stage boost achieved a maximum vehicle velocity of 1.266 km/s (4154 fps) at 4.3 seconds and at an altitude of 1.320 km (4332 ft) (zero time was the time of vehicle first motion). The maximum second-stage velocity was 2.608 km/s (8556 fps) at 6.22 seconds and at an altitude of 3.041 km (9476 ft). The maximum velocity and the altitude of its occurrence were respectively within 1 percent of the nominal velocity and 13.4 m (44 ft) of the nominal altitude as predicted by the preflight trajectory simulation. The maximum first-stage acceleration was 41.9 g's at 3.4 seconds, and the maximum second-stage acceleration was 102 g's at 6.05 seconds. The vehicle roll rate was not monitored. The monitored pitch and yaw rates appeared nominal throughout the flight. Complete Vehicle 3 per[redacted] in Appendix C.2.

[redacted]

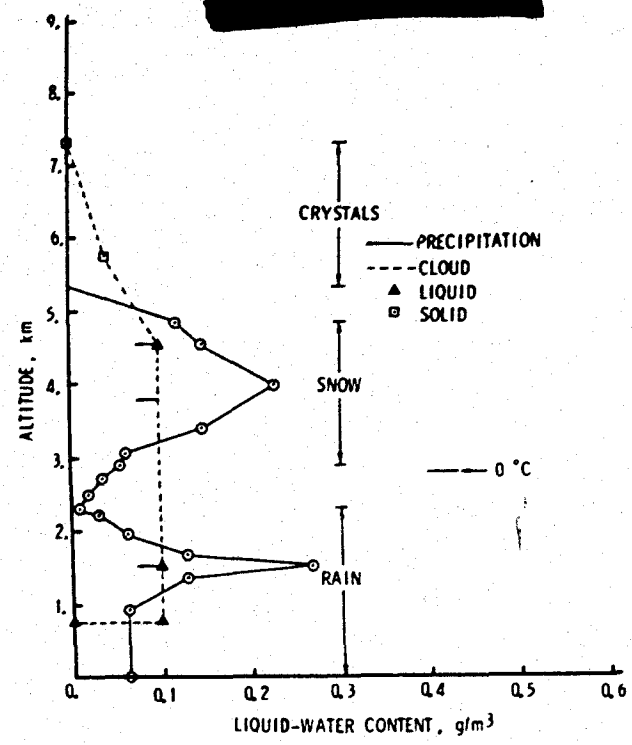

Figure 3.2.1 Preliminary Liquid-Water Content Versus Altitude, Vehicle 3

3.4 Surface Recession

A TC564 ablation detector as described by Riggan (1970) was used to detect the nosetip stagnation point recession. Eight tantalum-182 radioactive wire sources, installed at prescribed intervals along the longitudinal axis of the nosetip as shown in Figure 3.4.1, were sequentially lost as each was exposed to the high-speed air flow by the nosetip recession. The TC564 detected each source loss by the resulting decrease in total radioactivity, and this information was telemetered. Appendix B.3 provides additional information on the telemetry system and the vehicle instrumentation.

The nosetip recession data telemetered from Vehicle 3 exhibited severe signal shifts during the vehicle acceleration phases. These shifts made it impossible to determine source removal time for the first 8 seconds of the flight. A source loss was detected at 10.9 seconds. That it was source Number 3, whose location was 1.91 centimeters (0.75 inch) aft of the preflight stagnation point, was concluded only after measuring the recovered nosetip. The total stagnation point recession was 1.88-1.93 centimeters (0.74-0.76 inch). Figure 3.4.2 and 3.4.3 present the surface recessions measured on the nosetip.

Figure 3.4.4a and 3.4.4b are photographs of the nosetip when illuminated from the top and the side, respectively. Note the subtle forward-facing step that appears to spiral down the nosetip in the top-lighted photograph. Figure 3.4.4c and 3.4.4d are photomicrographs of the nosetip stagnation region. The recession measurements of the test heatshield are shown in Figure 3.4.5 and the surface roughness is illustrated in Figure 3.4.6.

[redacted]

[redacted]

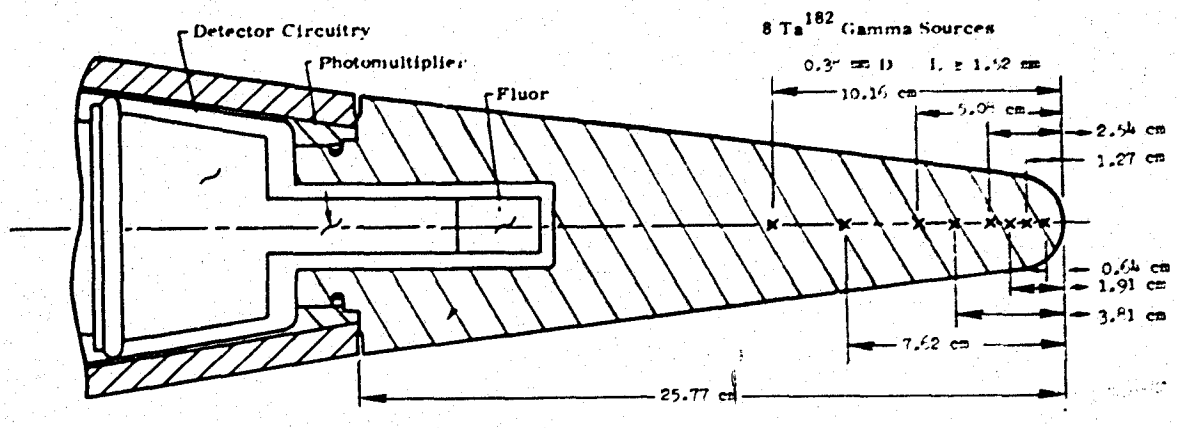

Figure 3.4.1 Nosetip Installation of ^{182}Ta Source Positions, Typical for All Vehicles

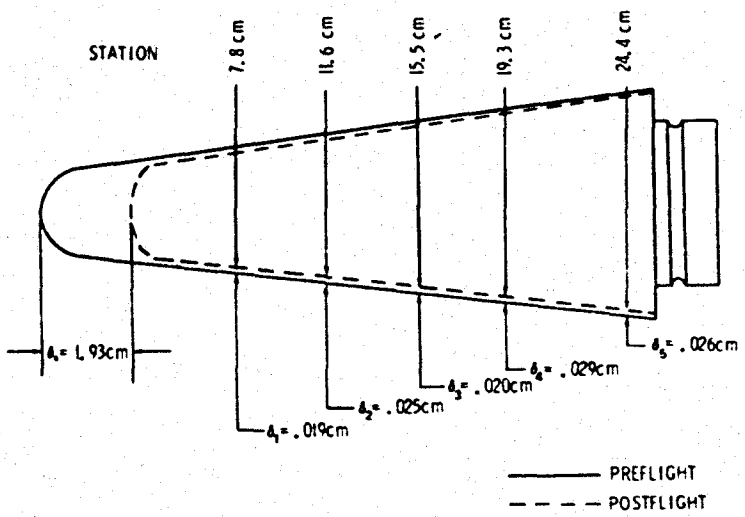

Figure 3.4.2 Nosetip Recession, Vehicle 3

[redacted]

[redacted]

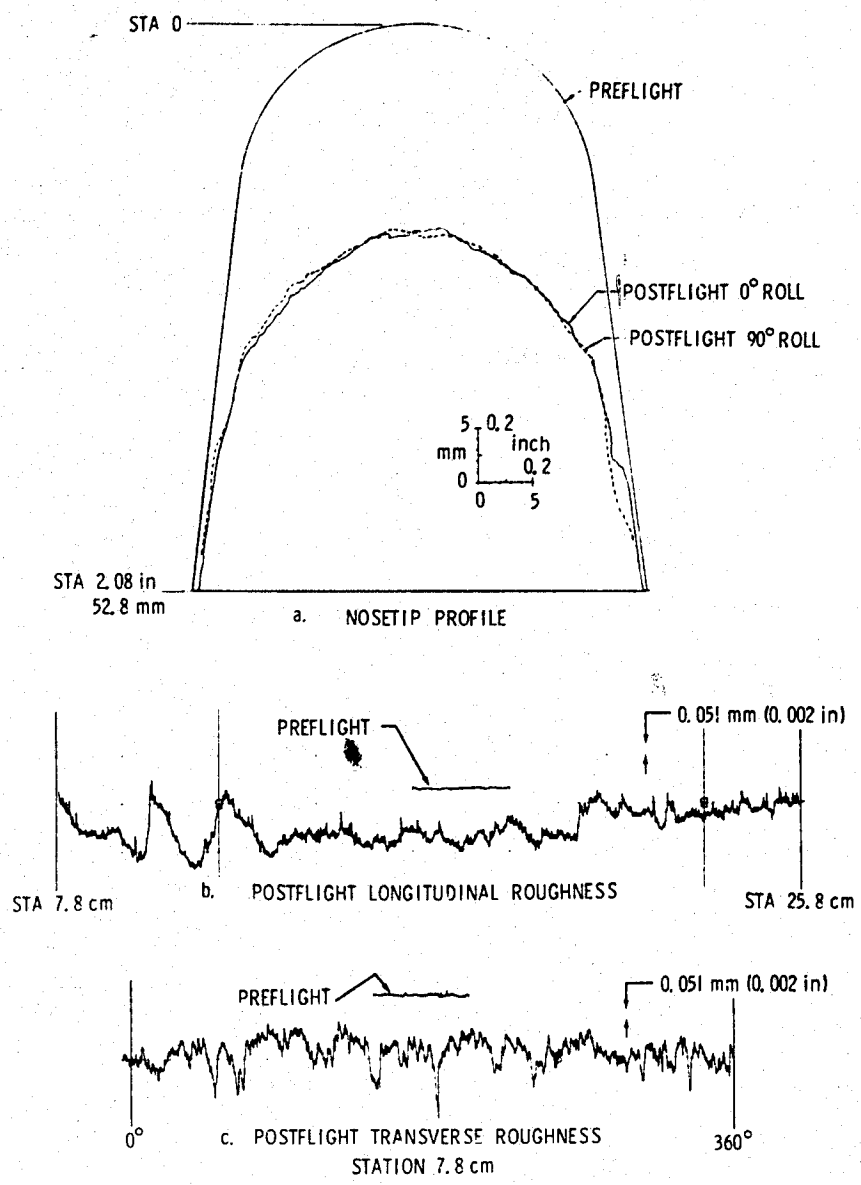

Figure 3.4.3 Nosetip Profile and Sidewall Roughness, Vehicle 3

[redacted]

[redacted]

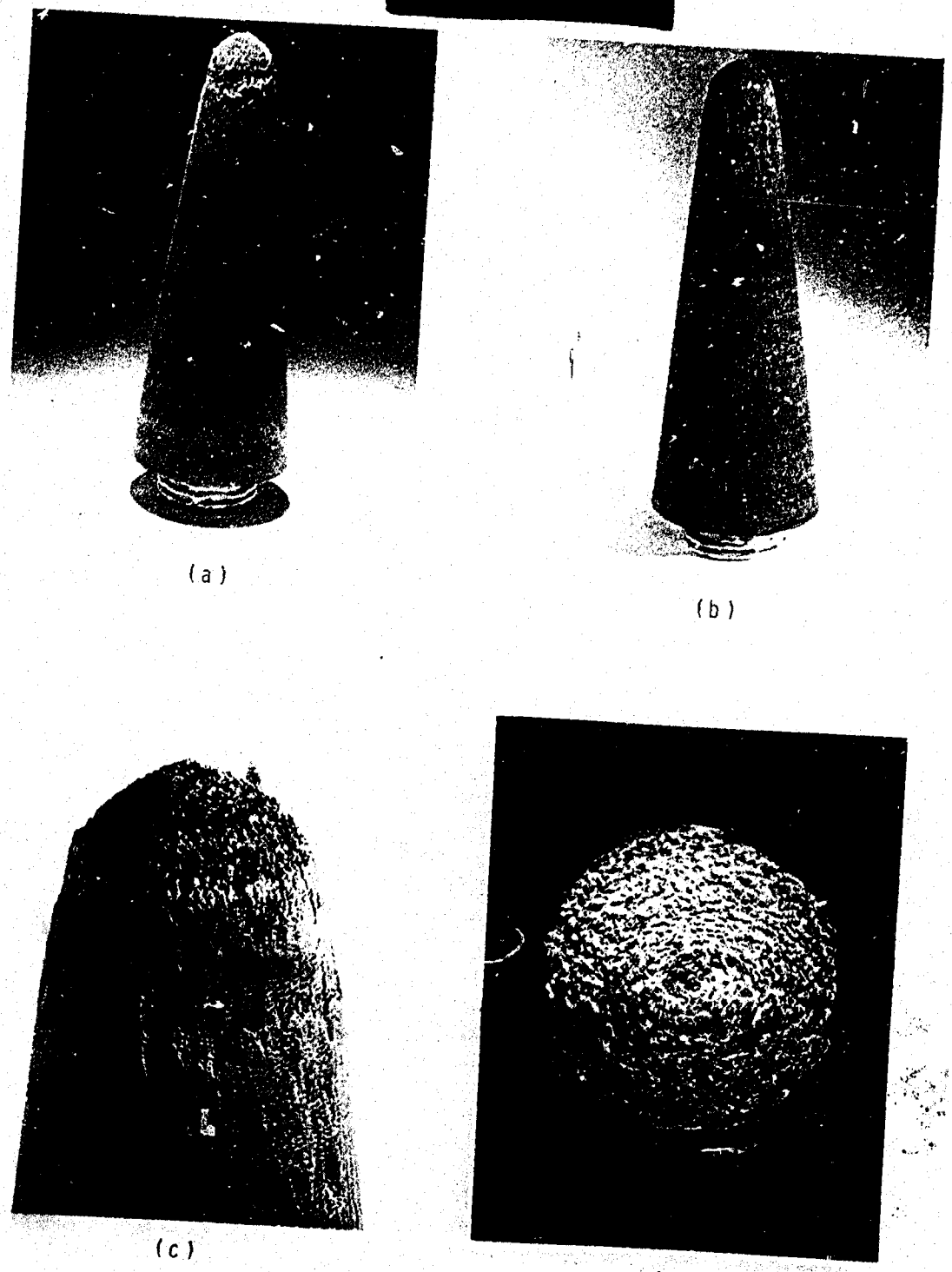

Figure 3.4.4 Photographs of Nosetip, Vehicle 3

[redacted]

[redacted]

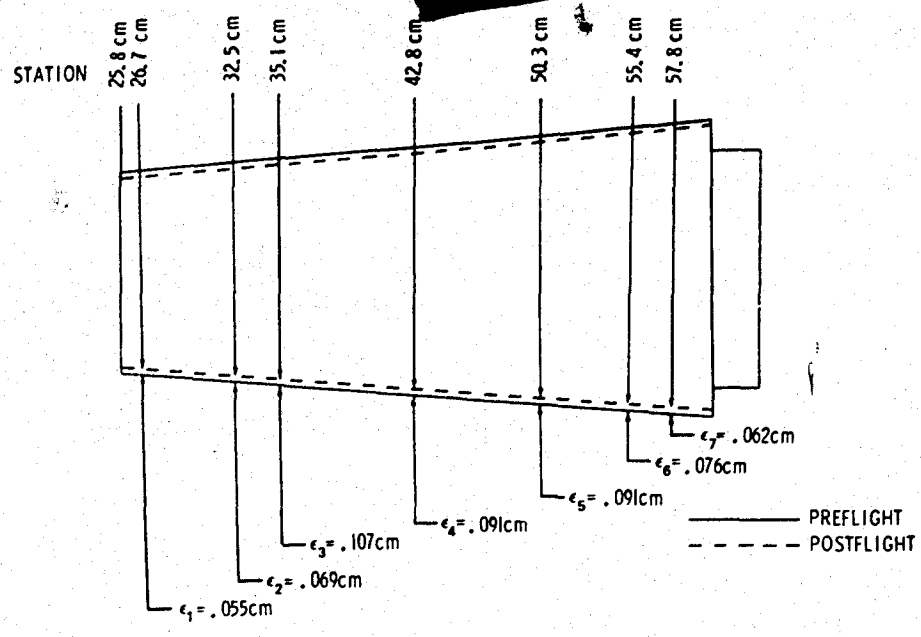

Figure 3.4.5 Heatshield Recession, Vehicle 3

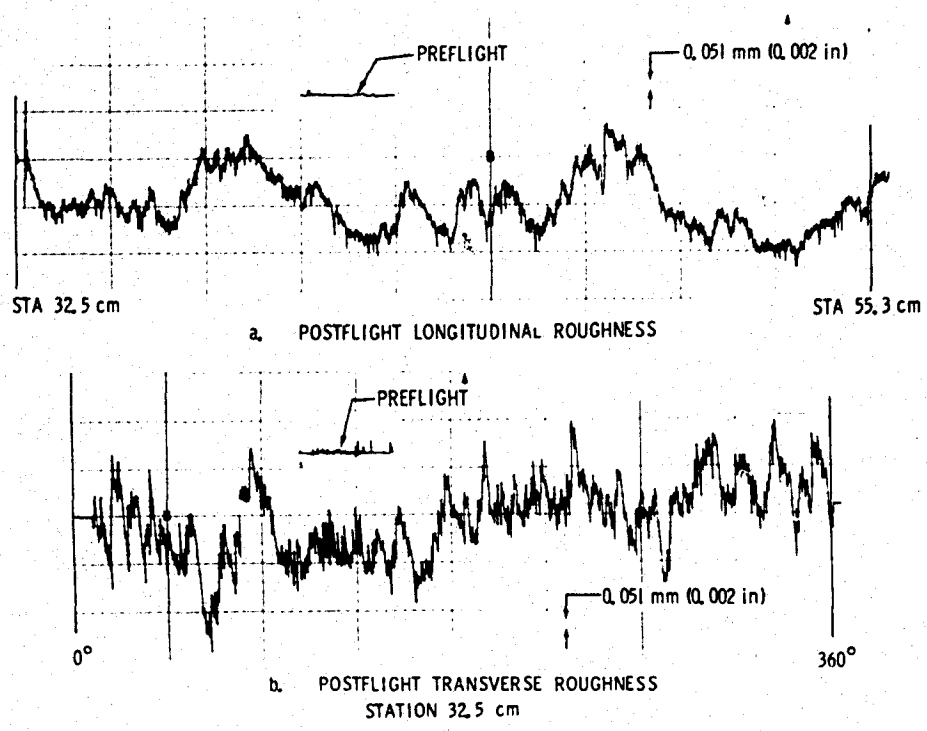

Figure 3.4.6 Heatshield Sidewall Roughness, Vehicle 3

[redacted]

4.0 Vehicle 4 Flight Test [redacted]

4.1 Sequence of Events

Vehicle 4 was launched into a storm at 1012 hours EST on Thursday, February 17, 1972. This flight test is designated by Sandia test number R341404 and NASA Wallops number Q2-5299.

A Sandia assembly team remained at Wallops after the February 3 launch and readied Vehicles 4 and 6 for the next tests. Vehicle 4, carrying a carbon-phenolic nosetip and front heatshield, was mounted on the HAD launcher at Pad 0, and Vehicle 6, carrying an ATJ-S graphite nosetip, was mounted on the Atlantic Research Corporation launcher at Pad 0. The ARC launcher, unlike the HAD launcher, is protected by a mobile building before a launch attempt.

Both test nosetips and front heatshields were enclosed in plastic bags containing a desiccant. The plastic bag covering the carbon-phenolic unit of Vehicle 4 was removed when the rocket arming was performed, before T-30 minutes, a standard procedure for the carbon-phenolic test units. The plastic bag on the graphite unit was attached to the launcher by a rip cord which split and removed the bag during the vehicle's first motion.

On Monday, February 14, the SAMS launch team reassembled at NASA Wallops and prepared to launch two vehicles sequentially into the next acceptable storm. The 0810 weather briefing gave little hope of a storm reaching Wallops before Wednesday night.

On Wednesday, the 0810 weather briefing indicated that a large storm system was moving eastward from the Gulf region, but the storm was forecast to pass completely south of Wallops and over the Atlantic Ocean on Thursday. The next prospective storm was not expected to reach Wallops before Saturday.

At 1330, Wednesday, an update summary of the meteorological situation indicated a shift toward more southerly winds at the upper atmospheric levels. The revised forecast predicted that an edge of the large storm system would pass over Wallops on Thursday. It was estimated that rain would start at Wallops around 0300 Thursday, with the heaviest rains occurring between 0800 and 1200. NASA agreed to commence operations on Thursday at 0600 so that a 0900 launch would be possible.

A weather briefing was held at 0610 on Thursday, February 17. No precipitation was occurring then or had occurred during the previous night in the Wallops vicinity. The forecast based on the previous night's soundings at 1900 hours continued to predict that some portion of the storm would pass over Wallops. The intensity and duration of this portion depended greatly on the winds at the upper levels, which would not be measured again until the 0700 soundings. The results of these soundings, which became available by 0730, showed that the upper-level winds had swung around to 230°, a more southerly direction than forecasted. These data indicated that a major part of the storm should now pass over Wallops.

The rain started around 0815 and increased rapidly to rates around 3 mm/hr. Preliminary PPI scans with the JAFNA S-band radar showed that the storm was reasonably homogeneous horizontally for distances up to 65 km (40 miles) in the direction from which it was advancing. The

[redacted]

[redacted]

extent of the storm homogeneity was monitored repeatedly to ascertain when a period of reasonably steady conditions would exist for at least 20 minutes. This would provide enough time to launch both rocket vehicles into the nearly identical meteorological environments.

The countdown was halted at 0840 to await a more homogeneous portion of the storm. The MRI Aztec aircraft was airborne by 0905. The radar on Wallops Island designated to track the Aztec could not detect a signal from the Aztec transponder as the aircraft continued its climb in the holding pattern east of Assateague Island. Over 30 minutes was consumed in trying, unsuccessfully, to establish a radar lock on the Aztec via its transponder or skin reflections. The Aztec pilot stated, however, that he could navigate satisfactorily through detection of the Snowhill VOR signal with the aircraft radio navigational equipment. With this reassurance it was decided to continue the launch attempt, and the countdown was restarted around 0930.

Continued evaluation of the JAFNA and SPANDAR radar data showed that the portion of the storm approaching Wallops was sufficiently homogeneous to permit the two flights. The tipping-bucket rain gage indicated a fairly steady precipitation rate of 2-4 mm/hr. The countdown was halted at T-2 minutes to permit the NASA C54 to complete its survey of the impact zone.

At 0954 the countdown was resumed, and Vehicle 6 was launched at 0956. Radar tracking indicated that the flight was nominal, and the Aztec crew reported that they were detecting the recovery beacon signal from the floating payload via the special radio receiver loaned to them by Sandia. Figure 4.1.1 is a contoured RHI radar scan taken along the 146°T azimuth within seconds of this launch. Radar reflected powers which fall into prescribed power (dbm) intervals after being range normalized were displayed by a given shade of gray. The contour shades used for these tests were dim gray, bright gray, white and then black as the reflected power increased. The horizontal grid line marks an altitude of 6.1 km (20,000 ft), and the vertical grid denotes 9.3 km (5 nm), 18.5 km (10 nm), and 27.8 km (15 nm) range from the JAFNA radars. For more information on this flight, see the flight-test report on ATJ-S graphite, Cole, et al (1973).

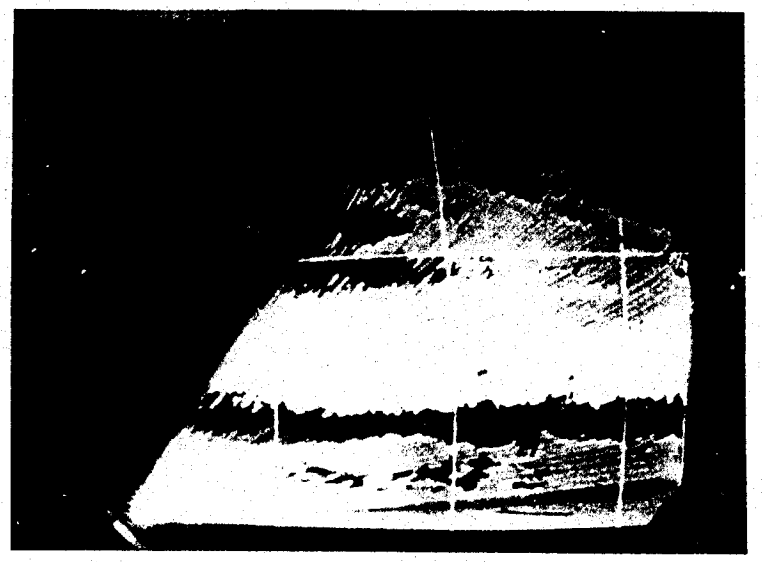

Figure 4.1.1 JAFNA S-Band Radar, RHI Contoured Scan, 0956 EST, February 17, 1972

[redacted]

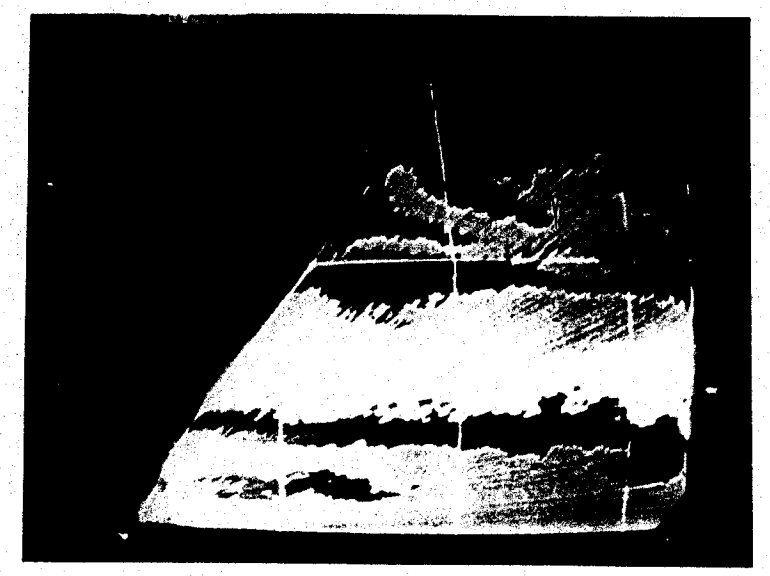

Figure 4.1.2 JAFNA S-Band Radar, RHI Contoured Scan, 1012 EST, February 17, 1972

Immediately after this launch the Pad 0 crew began the final checking and arming of the second rocket vehicle. This process was completed in about 12 minutes. Since the continued samplings of the storm with the radars and the rain gage showed it remaining reasonably steady, the countdown was started at T-2 minutes. The launch of the carbon-phenolic test unit occurred at 1012 and radar tracking of the vehicle indicated a normal flight. Figure 4.1.2 is a contoured RHI radar scan along 146°T azimuth for the second launch.

At the time of the second launch the MRI sampling aircraft was maintaining an altitude of 6.1 km (20.0 kft) in the holding pattern east of Assateague Island. It was then directed to fly to reference Point K, located 16 km (10 miles from the launcher on a 146°T azimuth, and commence sampling. The Aztec started moving toward point K but was greatly slowed by a 38-m/s (75-knot) head wind. To speed its arrival in the sampling pattern, the MRI crew was directed to sample the 6.1-km (20.0-kft) altitude enroute and then descend to 4.6 km (15.0 kft), where the head winds were not nearly so strong. The Aztec reached point K around 1035 and made a series of sampling runs from 4.6 km (15.0 kft) down to 0.3 km (1.0 kft). The aircraft then returned to Wallops Station and landed at 1110.

Shortly thereafter, the NASA C54 entered the test area and reported recovery beacon signals for both payloads. The recovery helicopter was vectored to the impact zone and returned to Wallops Station with the first payload by 1215. Meanwhile the C54 had sighted the second payload. The helicopter, after being refueled, retrieved the second payload by 1310.

The nosetips of both recovered payloads were still radioactive, since some of the ^{182}Ta sources remained. The heatshields and other components exhibited only a slight trace of radioactivity. Both units were bagged and transported to Wallops Island for fresh-water flushing and subsequent packaging for the trip to Sandia Laboratories.

 [redacted]

4.2 Meteorological Summary

A surface low-pressure system had been forecast to be in a position south of Cape Hatteras by 0700. The storm system associated with this low was expected to remain mostly south of Wallops Island as it moved out to sea. However, the upper-altitude winds became more southerly than had been forecast and caused a major portion of the large rain area associated with the storm to be directed over Wallops Island. Continuous rain was experienced from 0815 until 2000.

This storm was much deeper than the February 3rd storm, with cloud tops around 8.5 km (28.0 kft). The radar data indicated the presence of two melt levels, an unusual feature which complicated the analysis of the liquid-water content distribution.

The preliminary liquid-water content along the trajectory versus altitude as determined by Cunningham and Plank (1972) is shown in Figure 4.2.1. A more complete discussion of the meteorological data for this storm at launch time for Vehicle 4 is presented in Appendix D.1

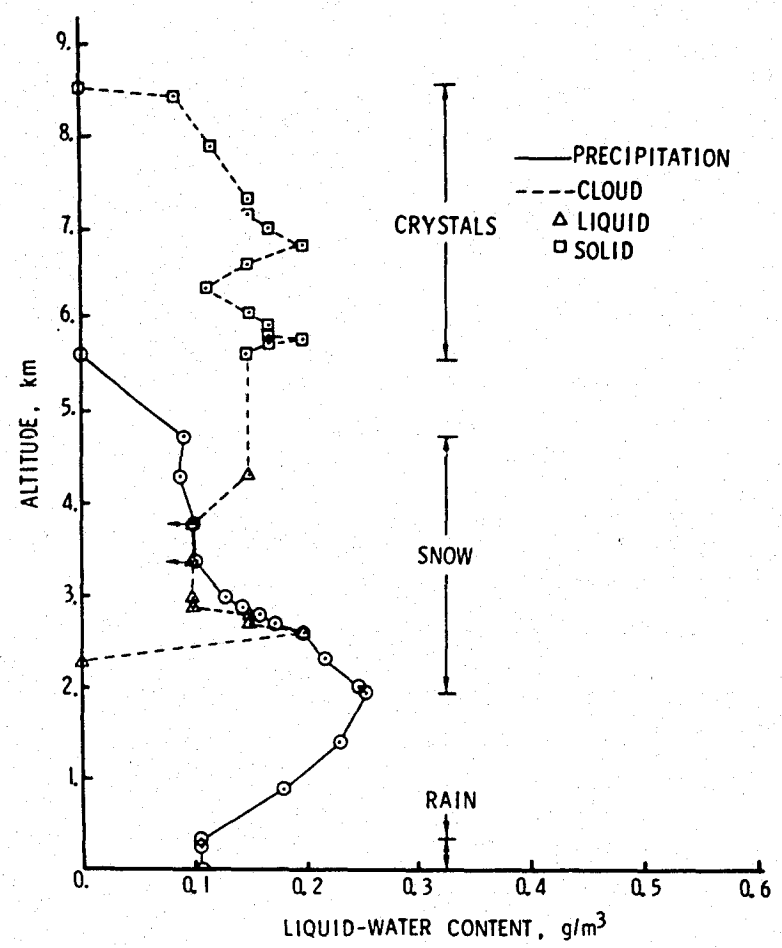

Figure 4.2.1 Preliminary Liquid-Water Content Versus Altitude, Vehicle 4

[redacted]

4.3 Vehicle Performance

The performance of the Terrier-Recruit booster system was nearly nominal during the Vehicle 4 flight test. The maximum velocity was 2.585 km/s (8482 fps) at 6.73 seconds and at an altitude of 3.057 km (10,029 ft) msl. This velocity was 1.9 percent below and the altitude 2.7 meters (9 ft) above the calculated preflight nominal values. The vehicle was cold-soaked at the ambient temperature of 3.9°C (39°F) before launch; this treatment has been found to produce performance decreases of the magnitude observed in this flight.

The maximum first-stage acceleration was 32.4 g's and the maximum second-stage acceleration was 101.8 g's. The vehicle commenced rolling at T+0.3. seconds, exceeding 400 degrees/sec from T±3.8 seconds until after parachute deployment. The pitch and yaw rates appeared normal throughout the flight. Vehicle 4 performance data are presented in Appendix D.2.

4.4 Surface Recession

The nosetip recession sensor operation was normal throughout the test. Eight ^{192}Ir radioactive sources were originally installed in the nosetip, as shown in Figure 3.4.1, and four were lost during the test. Measurements of the recovered nosetip indicated the stagnation point recession to be 2.82 cm (1.11 inches). Table 4.4.1 lists the time of loss for each source, and Figure 4.4.1 is a plot of these data. Figure 4.4.2 is a sketch showing the nosetip recession. Figure 4.4.3 shows the eroded nosetip stagnation region profile and sidewall roughness.

Figure 4.4.4a and 4.4.4b are photographs of the nosetip with the predominant lighting from the right and top, respectively. The longitudinal grooving is similar to that observed for Vehicle 3, but the stagnation region is not so severely pitted. The helical pattern can also be observed in Figure 4.4.4b, but the forward facing steps are not as evident. In Figure 4.4.4c can be seen two of the holes which were drilled radially into the nosetip to permit installation of the radioactive sources; one is on the upper left of the nosetip and the other on the lower right.

TABLE 4.4.1

Stagnation Point Recession, Vehicle 4

Source No.	Longitudinal Position (cm)	Longitudinal Position (inches)	Removal Time (sec)
1	0.64	0.25	6.45
2	1.27	0.50	7.32
3	1.91	0.75	8.49
4	2.54	1.00	10.21
5	3.81	1.50	NL*
6	5.08	2.00	NL
7	7.62	3.00	NL
8	10.16	4.00	NL

*Indicates the source was not lost.

[redacted]

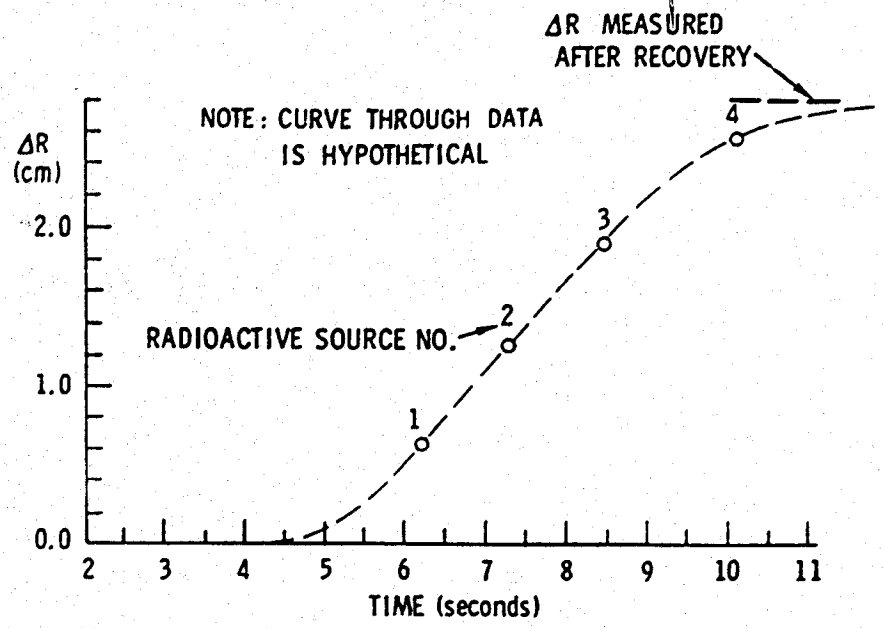

Figure 4.4.1 Stagnation Point Recession, Vehicle 4

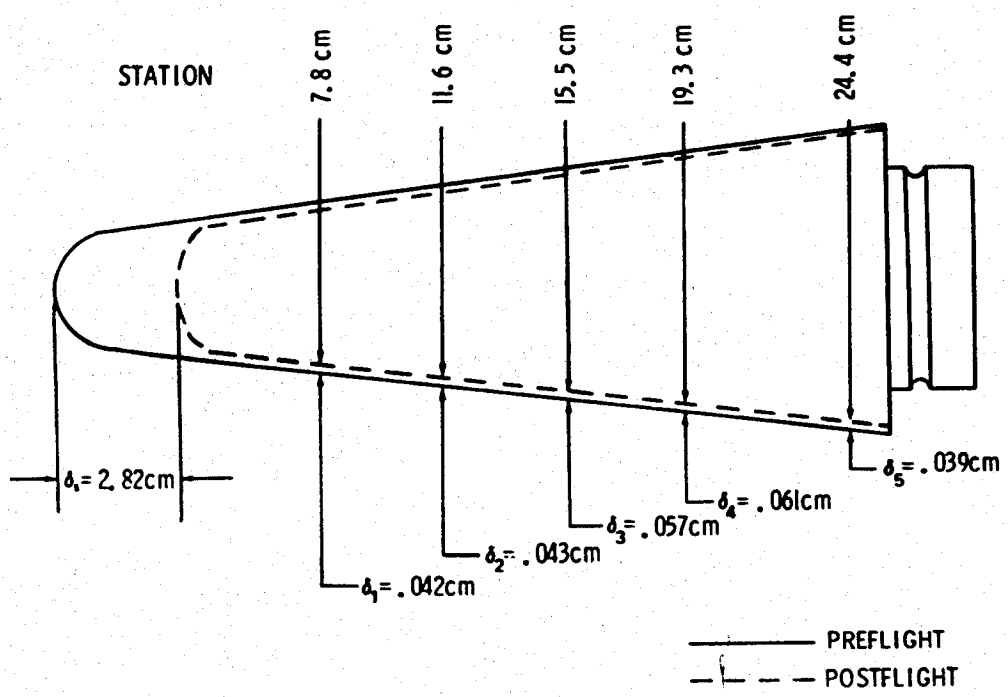

Figure 4.4.2 Nosetip Recession, Vehicle 4

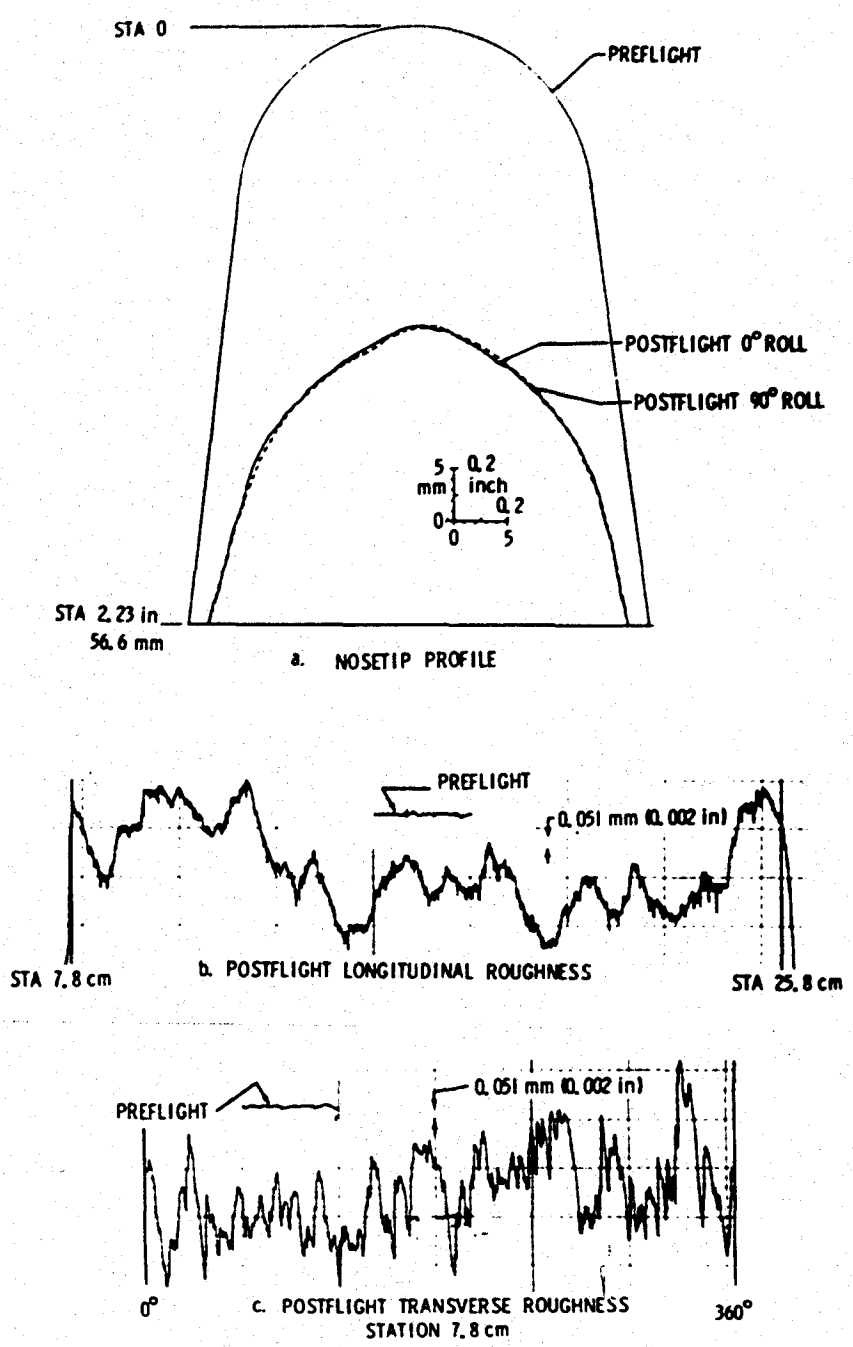

Figure 4.4.3 Nosetip Profile and Sidewall Roughness, Vehicle 4

[redacted]

(a)

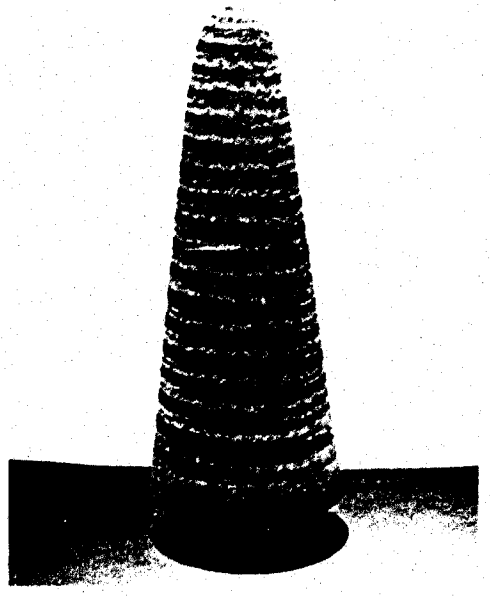

(b)

(c)

(d)

Figure 4.4.4 Photographs of Nosetip, Vehicle 4

[redacted]

[redacted]

Figure 4.4.5 is a sketch showing the measured heatshield surface recessions. Figure 4.4.6 presents the sidewall roughness measurements made on the heatshield.

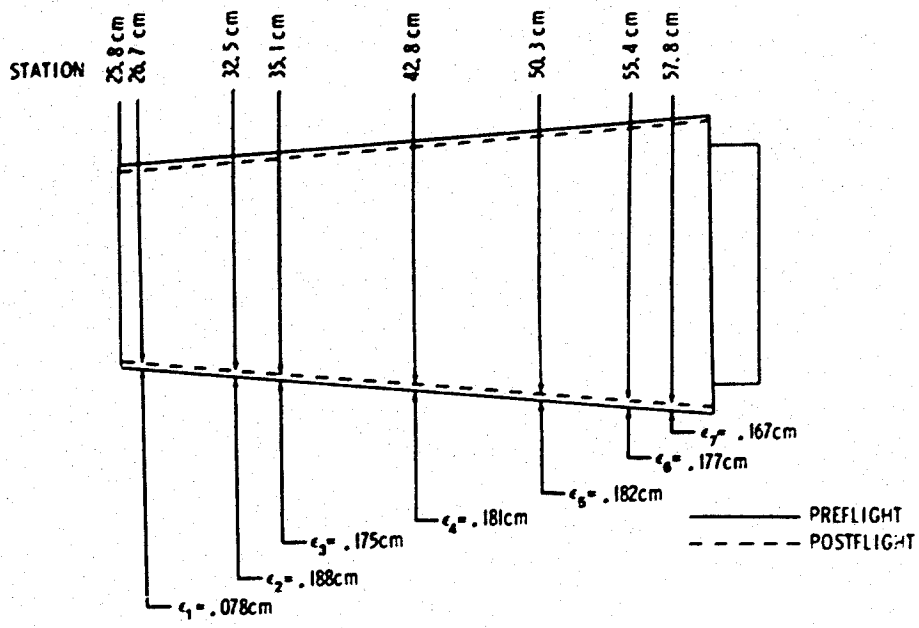

Figure 4.4.5 Heatshield Recession, Vehicle 4

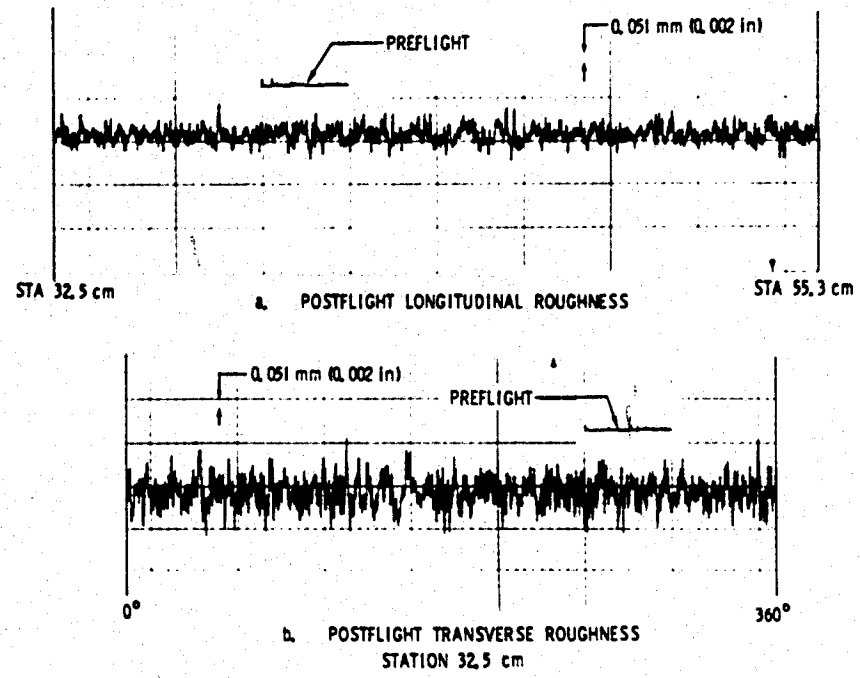

Figure 4.4.6 Heatshield Sidewall Roughness, Vehicle 4

[redacted]

5.0 Vehicle 5 Flight Test

5.1 Sequence of Events

The SAMS launch crew returned to NASA Wallops on Tuesday, March 14, 1972. Vehicle 5, carrying a carbon-phenolic nosetip and front heatshield, and Vehicle 7, carrying a ATJ-S graphite nosetip and filament-wound carbon-carbon front heatshield, were assembled and installed, respectively, on the HAD and ARC launchers at Pad 0 by Wednesday, March 15. The desire was to launch Vehicle 5 into a storm whose surface precipitation rate was less than 0.5 mm/hr and Vehicle 7 into a storm whose surface precipitation rate was 1-3 mm/hr. In both cases it was desired that the cloud tops exceed 4.6 km (15.0 kft) msl.

The weather briefings on Wednesday and Thursday forecast the gradual eastward movement of a low-pressure system from the Mississippi Valley, with the possibility of attendant showers in the Wallops area by late Thursday afternoon or evening. By 1600 EST on Thursday there were scattered showers in the area, but JAFNA radar probings indicated that the situation was unacceptable for a launch.

The 0800 briefing on Friday, March 17, revealed that 18 mm of rain had accumulated overnight, between 2130 and 0300. With the low-pressure system still situated over the Delmarva Penninsula, scattered showers were forecast to begin around noon. A launch attempt was tentatively scheduled for the afternoon.

Light rain began to fall around 1335. Subsequent radar probing indicated the storm to be somewhat cellular but adequate for a test of Vehicle 7 with the ATJ-S graphite nosetip. After verifying that the MRI sampling aircraft was aloft in the holding pattern, Vehicle 7 (R341413) was launched at 1620:38.45 EST. The results of this flight test are presented by Cole, et al (1973).

Immediately after the parachute-retarded water impact of the Vehicle 7 payload, the launch countdown for Vehicle 5 was cycled to a holding position at T-5 minutes. The meteorological conditions desired for this vehicle did not materialize, and this second launch attempt was canceled at 1705 EST.

On Monday, March 20, the JAFNA radar was forced to cancel a Clear Air Turbulence test in the mid-afternoon because of the unexpected arrival of a deep cirrus-altostratus cloud layer. A survey with the JAFNA S-band radar between the azimuths of 255°T and 360°T showed that this nonprecipitating cloud system had equivalent liquid-water contents as large as 0.2 g/m^3, a base of 2.4 km (8.0 kft) and tops up to 9.1 km (30.0 kft)-- ideal for the Vehicle 5 test.

NASA Wallops scheduled a launch attempt for 1800, based on estimates that the cloud system would overrun Wallops by then. However, the cloud layer dissipated before intercepting the flight-test azimuth, and the launch was canceled at 1830.

On Tuesday, the 0800 forecast was marginally encouraging, and a launch was scheduled for 1500. Periodic JAFNA radar probings showed a dissipating trend, and by 1300 the launch was again canceled.

On Wednesday, March 22, rain began around 0630. At the 0800 briefing the presence of a large storm system was indicated. A launch attempt was scheduled for 1000. Gusty winds accompanying the storm raised concern that the JAFNA radar [illegible] operations, causing cancellation of the launch attempt. (The attitude of the [illegible] antenna cannot be controlled at wind speeds greater than 20 m/s (40 knots) at which the antenna must be operated to a vertical store position and locked.) The winds remained below the critical level and the countdown proceeded. The MRI Aztec aircraft took off and climbed to an altitude of about 8.7 km (28,000 kft) while maintaining a holding pattern east of Assateague Island.

Vehicle 5 was launched at 1048:00 EST, when the cloud tops were about 8.2 km (27.0 kft) and the rain rate at Pad 0 was about 0.5 mm/hr. Figure 5.1.1 shows the JAFNA RHI scan through the storm at 1047 EST.

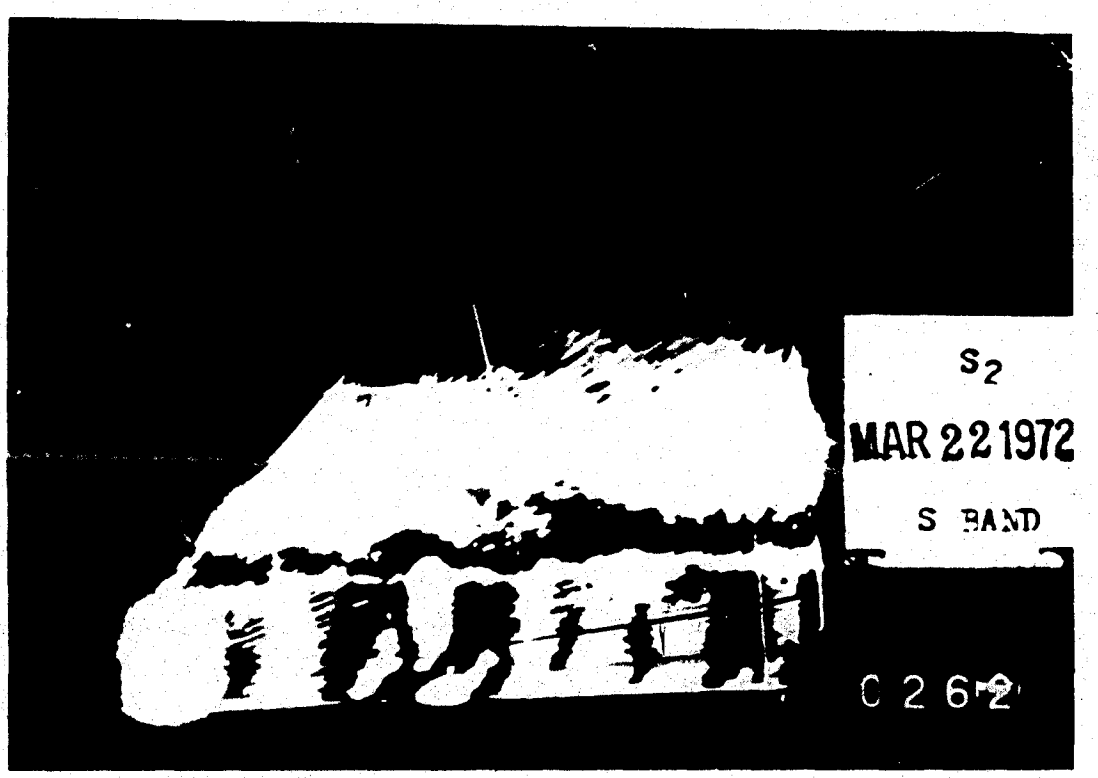

Figure 5.1.1 JAFNA S-Band Radar RHI Contoured Scan, 1047 EST, March 22, 1972

Coordinated meteorological sampling operations with the radar and aircraft began immediately after launch. Following these sampling operations, the recovery aircraft were directed to the floating payload by the Wallops radar. The helicopter, although it picked up the payload, was forced to land at Wallops Island because of heavy rain squalls and fog over the normal landing site at Wallops Station. After the squall line passed, the helicopter successfully returned the payload to Wallops Station. The nosetip was found to be radioactive, and the payload was bagged and taken to the Pad 0

assembly building, where it was flushed with fresh water and packaged for shipment to Sandia Laboratories.

5.2 Meteorological Summary

On March 22, 1972, an occluded front extended southeastward from Buffalo to Philadelphia. From there, the warm front extended east-southeastward out to sea, and the cold front extended south and southwestward just to the east of the Appalachian Mountains. Vehicle 5 was launched into the prefrontal storm associated with the cold front. Light rain began at Wallops Island at 0835, with surface winds gusting to 20 m/s (40 knots). The precipitation rates were initially somewhat unsteady, varying between 0.3 and 3.5 mm/hr. By 1035 they had steadied around a rate of 0.5 mm/hr. Four minutes after the launch, the rates measured at Pad 0 increased to 15.2 mm/hr as a convective rain cell passed.

Coordinated measurements of the storm were made by the S-band radars and the Aztec aircraft. The preliminary liquid-water content distribution derived from these data by Cunningham and Plank (1972) is shown in Figure 5.2.1. Appendix E.1 presents a more complete discussion of the meteorological data.

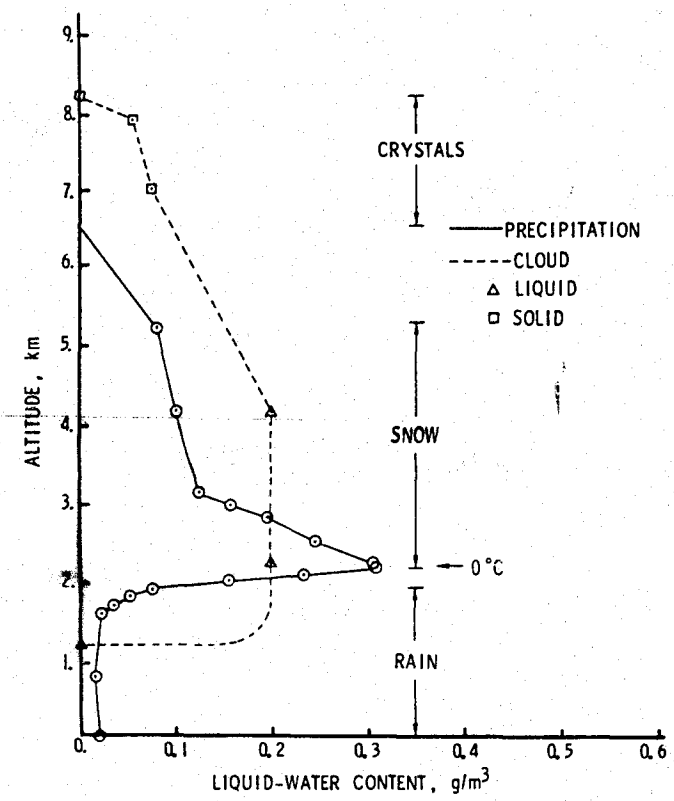

Figure 5.2.1 Preliminary Liquid-Water Content Versus Altitude, Vehicle 5

[redacted]

5.3 Vehicle Performance

The performance of the Terrier-Recruit booster system during the flight of Vehicle 5 was nearly nominal. The maximum velocity achieved was 2.470 km/sec (8431 fps) at 6.60 seconds and at an altitude of 3.129 km (10265 ft) msl. The maximum velocity was 2.5 percent below and the altitude of its occurrence 74.7 m (245 ft) above the calculated preflight nominal values. These differences probably were due to the boosters being cold-soaked at 10°C (50°F) before launch and to the fact that this Recruit had 1 percent less than the nominal propellant charge.

The maximum acceleration experienced during the Terrier boost was 36.0 g's and the maximum acceleration during Recruit boost was 101.0 g's. The roll rate was not monitored on this test, but the measured pitch and yaw rates indicated a normal flight. Vehicle 5 performance data are presented in Appendix E.2.

5.4 Surface Recession

The nosetip recession sensor functioned properly throughout the flight. Eight ^{182}Ta radioactive sources were installed in the nosetip before the test, as shown in Figure 3.4.1. Four sources were lost during the flight, and 3.02 cm (1.19 inches) of stagnation point recession was measured on the recovered nosetip. Table 5.4.1 indicates the removal times for each source and Figure 5.4.1 is a plot of these data. The nosetip recession as measured after recovery is indicated in Figure 5.4.2, and the nosetip profile and sidewall roughness measurements in Figure 5.4.3.

TABLE 5.4.1

Stagnation Point Recession, Vehicle 5

Source No.	Longitudinal Position (cm)	Longitudinal Position (inches)	Removal Time (sec)
1	0.64	0.25	6.35
2	1.27	0.50	7.00
3	1.91	0.75	7.81
4	2.54	1.00	9.15
5	3.81	1.50	NL*
6	5.08	2.00	NL
7	7.62	3.00	NL
8	10.16	4.00	NL

*Indicates the source was not lost.

Photographs of the recovered nosetip are presented in Figure 5.4.4. Figures 5.4.4a and 5.4.4b show the nosetip when illuminated from the side and top, respectively. Note the irregular profile of the conical sidewall. The helical surface pattern is readily observed in Figures 5.4.4c and 5.4.4d.

Figure 5.4.5 shows the heatshield surface recession. Figure 5.4.6 shows sidewall roughness measurements made at two locations on the heatshield.

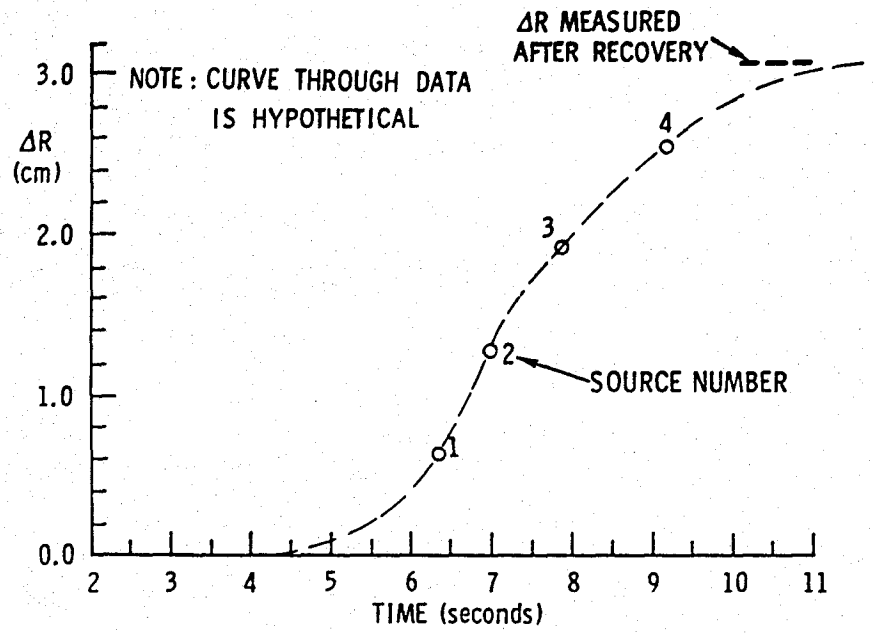

Figure 5.4.1 Stagnation Point Recession, Vehicle 5

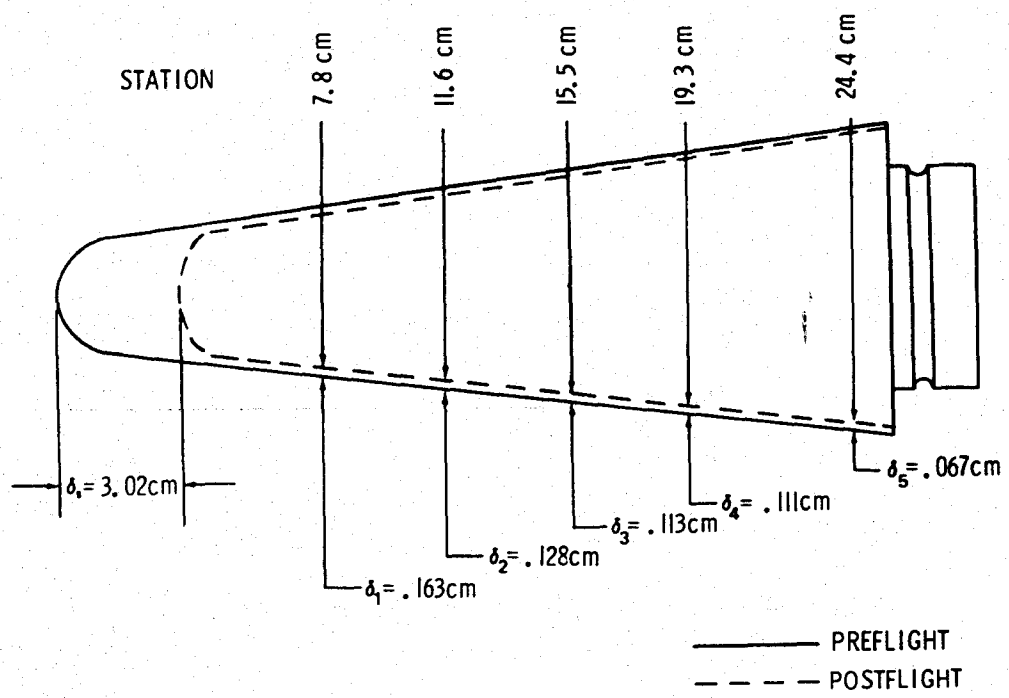

Figure 5.4.2 Nosetip Recession, Vehicle 5

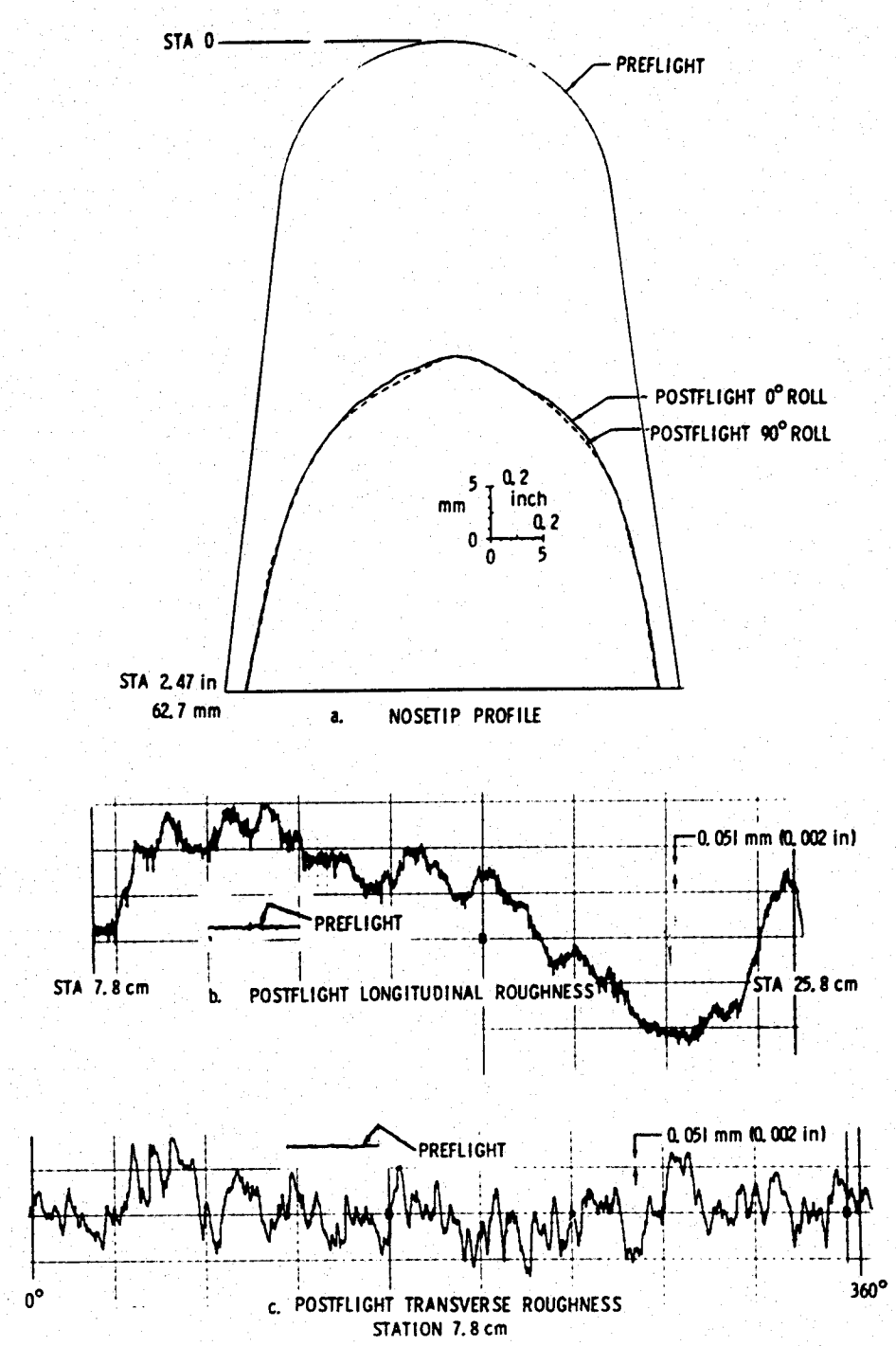

Figure 5.4.3 Nosetip Profile and Sidewall Roughness, Vehicle 5

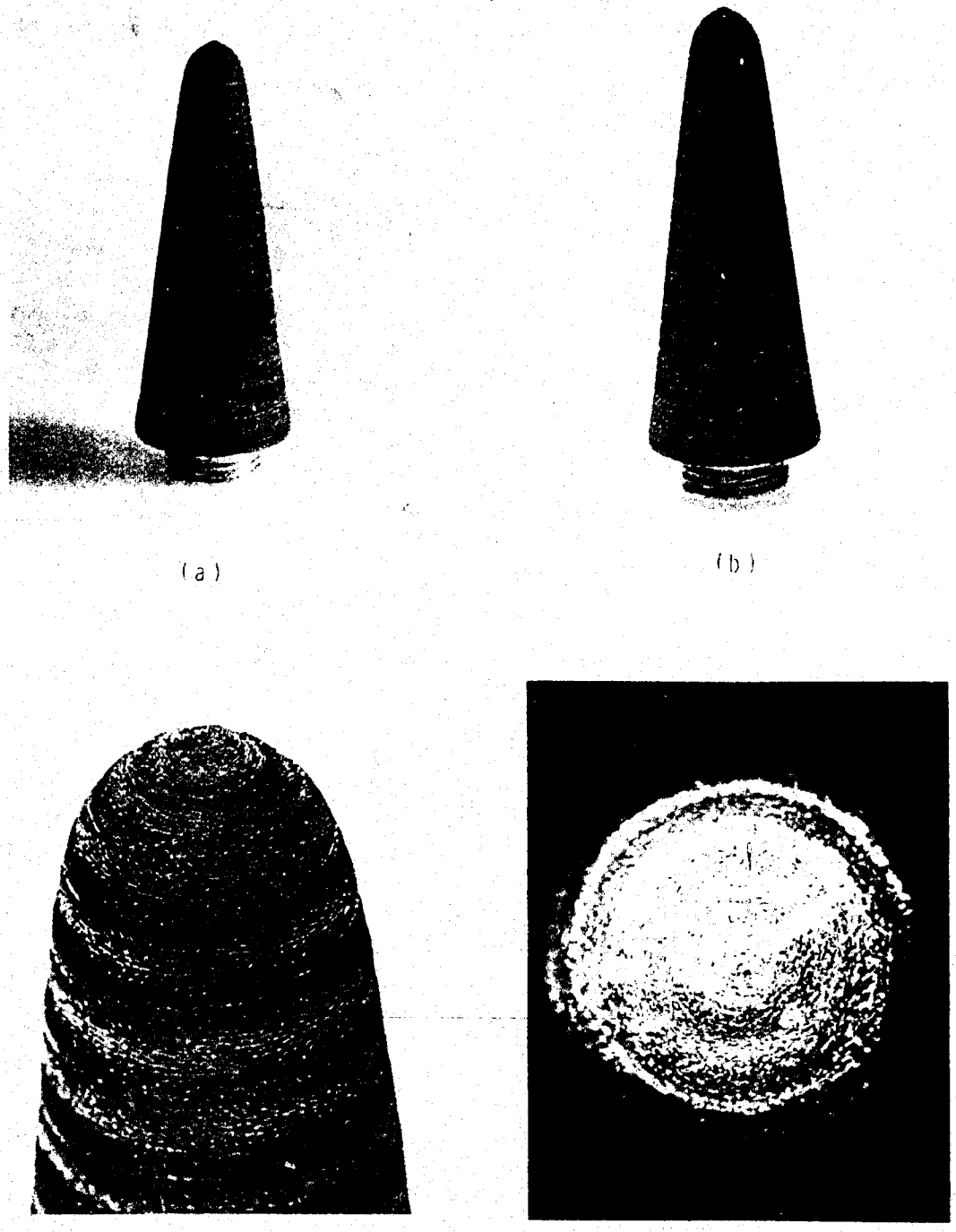

Figure 5.4.4 Photographs of Nosetip, Vehicle 5

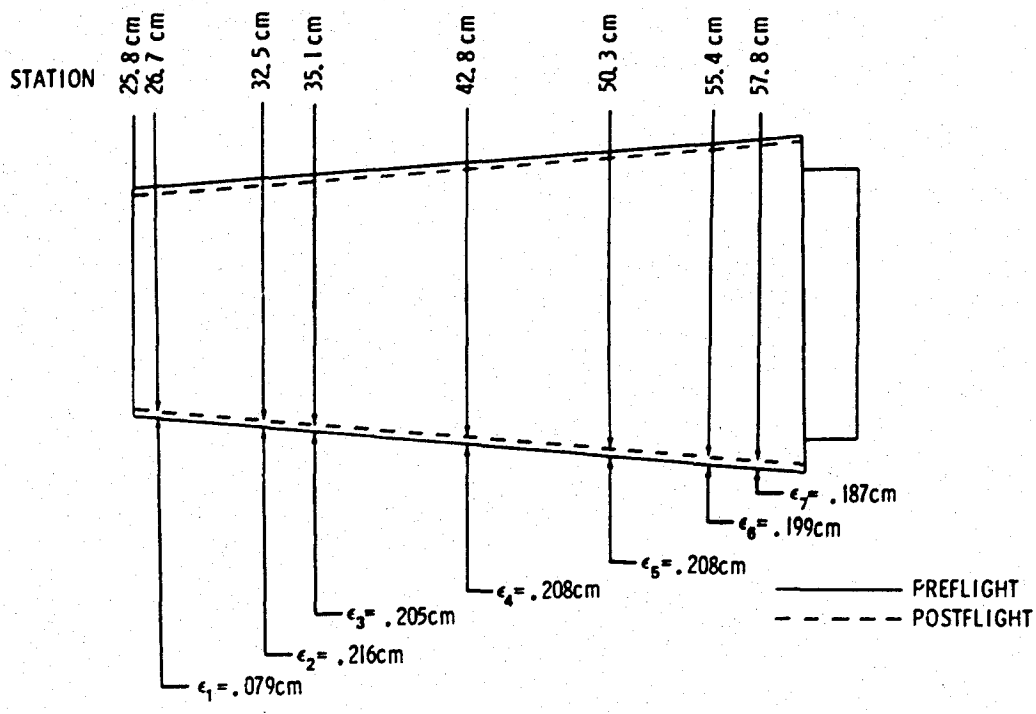

Figure 5.4.5 Heatshield Recession, Vehicle 5

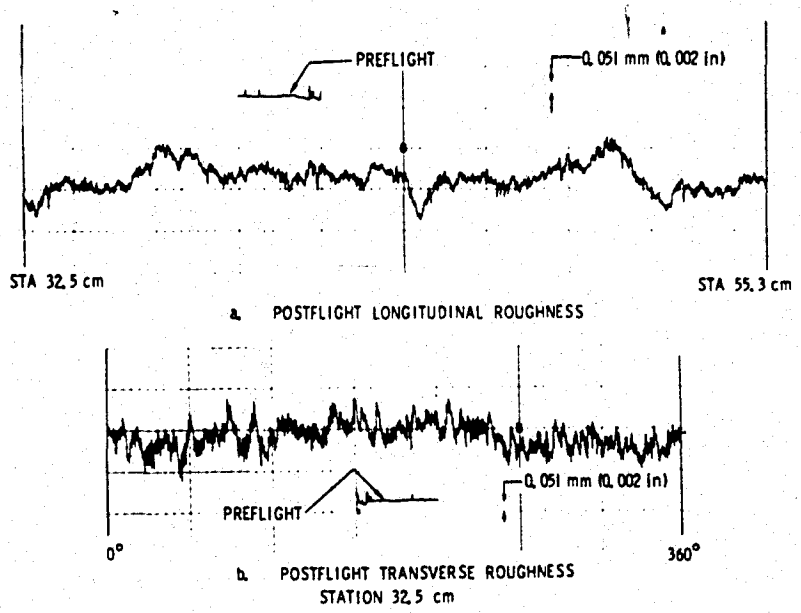

Figure 5.4.6 Heatshield Sidewall Roughness, Vehicle 5

6.0 Discussion

6.1 Accuracy of Measurements

6.1.1 Radar Tracking Data

NASA Wallops used two C-band radars to simultaneously track each rocket vehicle. The Wallops Station Handbook (1964) states that the accuracies for the AN/FPQ-6 radar are range ± 4.6 m (15 ft) and angle ± 0.05 mils. For the AN/FPS-16, they are range ± 4.6 m (15 ft) and angle ± 0.1 mil.

At an altitude of 12.2 km (40.0 kft), which insures that the vehicle has passed through all of the storm system, the vehicle range is about 23.2 km (76.0 kft). This translates into a maximum radar uncertainty of ± 30.4 m (100 ft) in the plane perpendicular to the radar beam and ± 4.6 m (15 ft) in range.

6.1.2 Payload Prime Instruments

The prime instruments in the payloads are the longitudinal servo-accelerometer and the TC-564 recession gage. The servo-accelerometer is stated to have an accuracy better than ± 1.0 percent over its acceleration range of -50 to +150 g's. Signal conditioning and subsequent telemetering reduce these accelerometer data to an estimated accuracy of ± 2 percent. The vehicle velocity histories obtained from integrating these acceleration data and from the radar data have been found to agree within ± 1.8 percent for all the Terrier-Recruit flights at Wallops Island.

The stagnation point recession history is obtained through the observation of ^{182}Ta source removal times, a knowledge of the original locations of the sources in the nosetip, and the assumption that the stagnation region of the nosetip has receded to each source location at its removal time. The accuracy of the recession measurement depends directly upon how well each of these can be determined.

The time for a given source removal is taken to be the point at which the first change is noted in the telemetered output from the TC564 recession sensor. The response of the TC564 and the telemetry band width permit this time to be determined to within ± 0.001 second.

The longitudinal locations of the 0.76 ± 0.025-mm (0.030 ± 0.001-inch) diameter holes were measured for each nosetip to within ± 0.025 mm (0.001 inch). The largest variation in hole location for the sources lost on Vehicles 3, 4, and 5 was 0.076 mm (0.003 inch) for source 2, Vehicle 5. The others were within ± 0.025 mm (0.001 inch) of their nominals. The ^{182}Ta source wires were 0.38 mm (0.015 inch) in diameter. This offered the possibility of a 0.18 - 0.20-mm (0.007 - 0.008-inch) shift of source positioning within each hole; x-ray photographs of each nosetip indicated the positioning of each source within its hole so that the amount of the shift could be determined to within ± 0.051 mm (0.002 inch).

The removal of a source before the surface recedes to the source's position appears to offer the largest uncertainty in the recession measurement. A simple erosion calculation indicates that a 0.75-1.52-mm (0.030-0.060-inch) deep hemispherical crater could be produced by the impact at 2.5 km/sec (8.2 kft/sec) of a 1-mm (0.040-inch) diameter water drop. Thus a source might be

eroded out of the nosetip as much as 0.76-1.52 mm (0.030-0.060 inch) before the surrounding surface recedes to that point. It is therefore concluded that the maximum uncertainty band for recession data is ± 0.001 second in removal time and -1.5 mm to +0.13 mm (-0.060 to + 0.005 inch) in surface position.

6.1.3 Meteorological Data

The final meteorological assessment of each storm depends upon the integration of numerous sources of meteorological data. The prime sources are the data from the ground-based instruments, the weather radar, the radiosondes and the instrumented aircraft. The accuracy of these meteorological data, now being evaluated by AFCRL and SAMSO, will be disclosed in one of their future reports. Preliminary results of their study suggest that the liquid-water content versus height is being determined to an accuracy of ± 30 percent for the rain regions, ± 50 percent for the snow region, and ± 100 percent for the ice regions.

6.2 Nosetip Recession

The stagnation point recession data obtained during the storm-penetration flights of Vehicles 3, 4, and 5 were examined for possible correlations of the effective erosion coefficients with other test parameters. Since the TC564 recession gage on Vehicle 3 malfunctioned during the test, only the removal of the third ^{182}Ta source was detected. The final stagnation point recession was measured on the recovered payload. These limited data, though useful for determining the total integrated effect of the storm, could not be used to determine variations of the erosion coefficient during the test.

The recession data obtained for Vehicles 4 and 5 were sufficiently complete to make a closer examination practical. The CMA (charring material and thermochemical ablation) code developed by the Aerotherm/ACUREX Corporation was used to estimate the temperature and density profile histories of the material in the nosetip region for Vehicles 4 and 5. For these calculations, the code was employed inversely where the surface recession was forced to occur as observed experimentally, but the vehicle's nose radius remained constant at its preflight value. The code then computed the temperature and density profiles and the aerothermal ablation recession. For these calculations, the aerodynamic heating was specified from the vehicle flight-trajectory. Figures 6.2.1 and 6.2.2 show, respectively, the surface conditions and the aerothermal ablation calculated for Vehicles 4 and 5. Also included in each figure are the actual recession data (the numbered circles) and the forced recession history (the curve passing through the circles).

These calculations indicate similar material histories for both tests. The material began to char, but then reverted to a hot, nearly virgin density state during the period of maximum erosion. Figures 6.2.3 and 6.2.4 show the nosetip temperature histories of Vehicles 4 and 5 for positions 0, 0.05 mm (0.002 inch), 0.11 mm (0.0045 inch) and 0.20 mm (0.008 inch) below the surface. Figures 6.2.5 and 6.2.6 are companion plots showing the material-density histories.

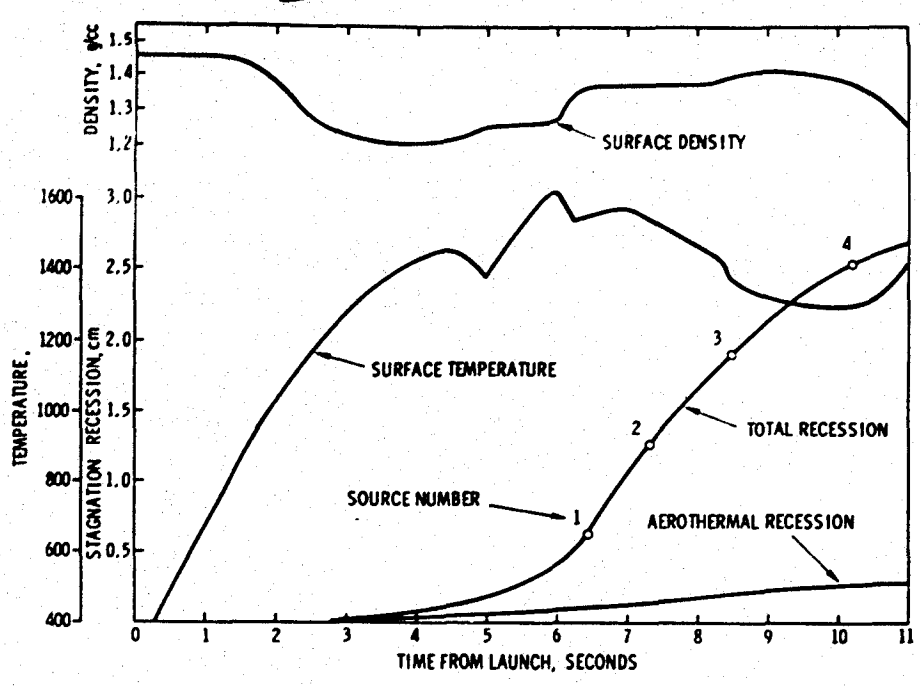

Figure 6.2.1 Calculated Surface Conditions and Stagnation Recession, Vehicle 4

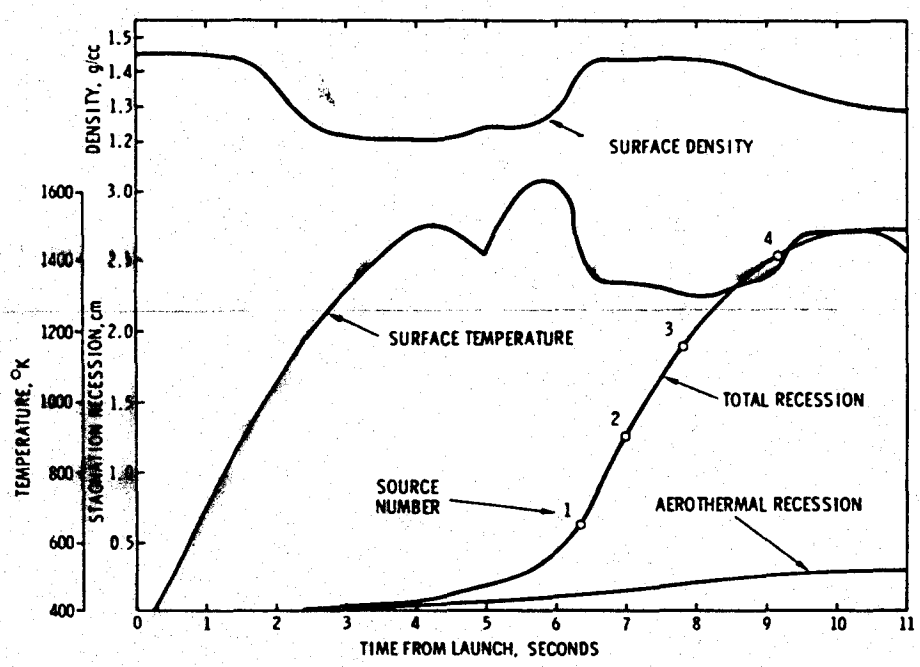

Figure 6.2.2 Calculated Surface Conditions and Stagnation Recession, Vehicle 5

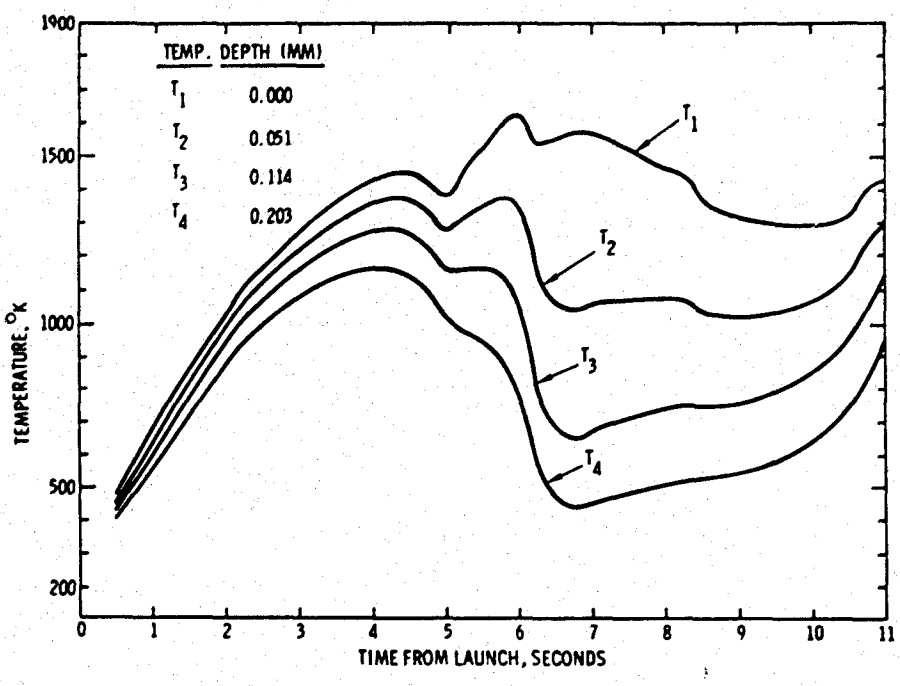

Figure 6.2.3 Material Temperatures, Vehicle 4

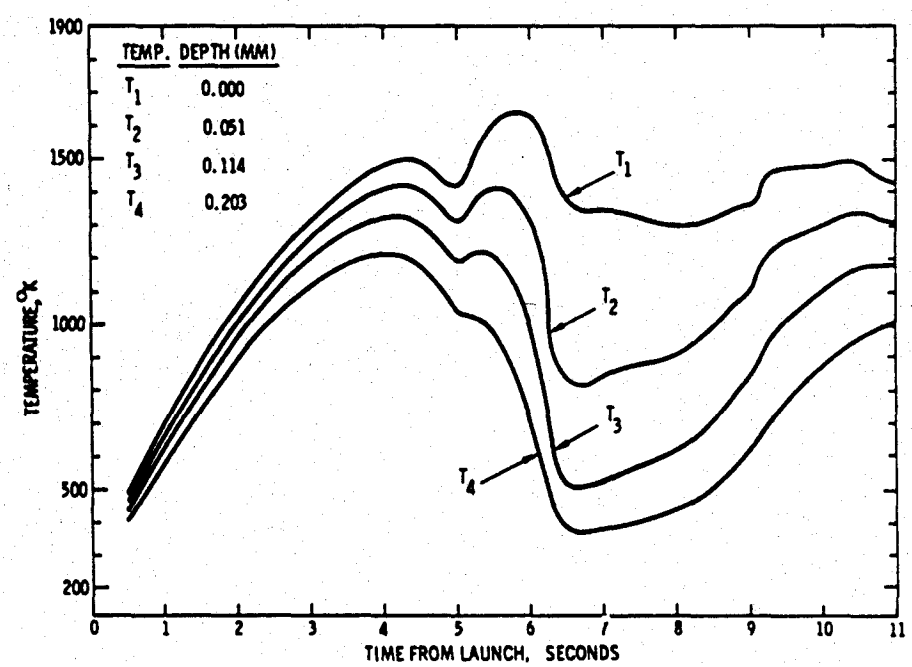

Figure 6.2.4 Material Temperatures, Vehicle 5

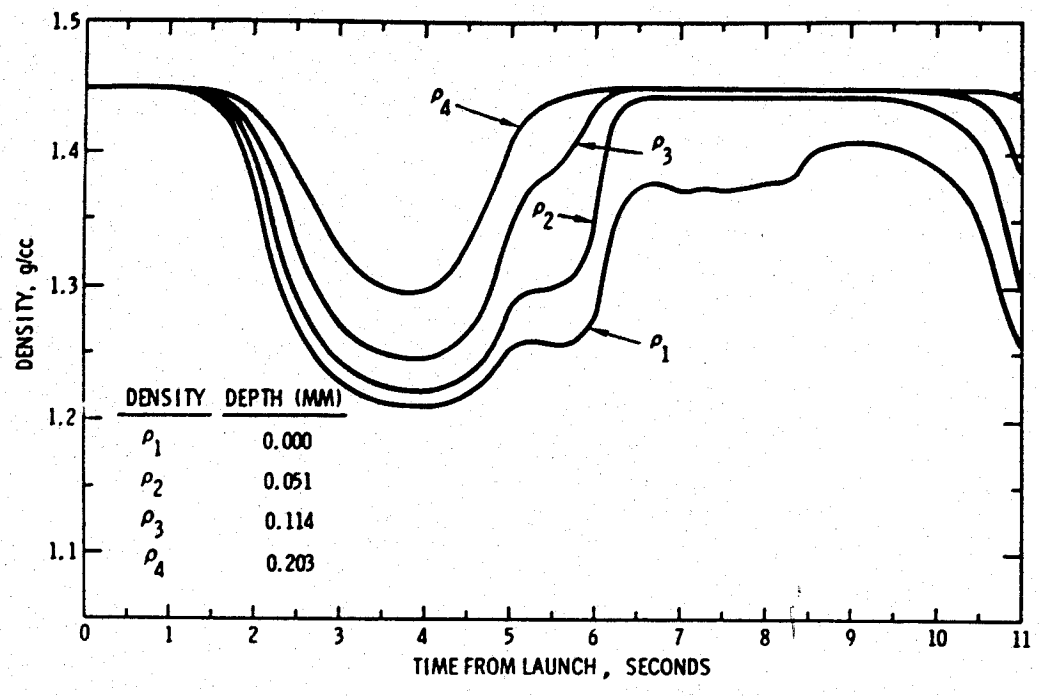

Figure 6.2.5 Material Densities, Vehicle 4

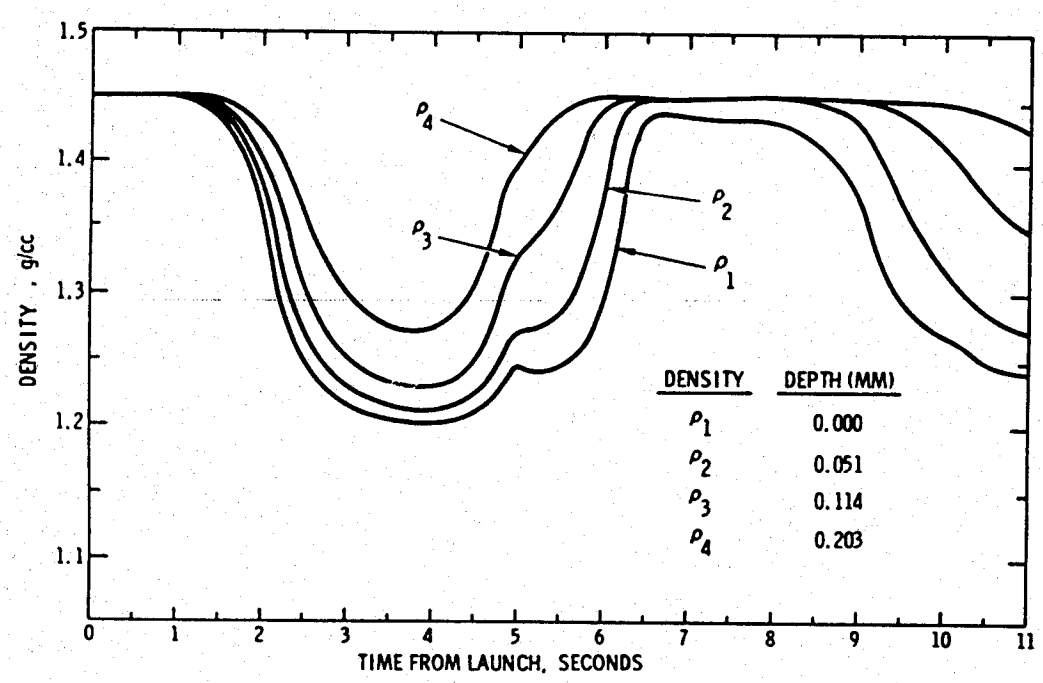

Figure 6.2.6 Material Densities, Vehicle 5

The SPLAT code, described by Cole and Ellis (1970), was then used to calculate the effective erosion coefficients for the intervals between successive ^{182}Ta source removals. This code accounts for the effects of particle deflection and/or deceleration in the shock layer and for liquid-particle breakup. The erosion model currently employed in the code is:

$$\dot{R} = \frac{K}{2} \frac{LWC}{\rho_{AB}} V_I^2 \left(\frac{V_I}{V_R}\right)^{N-2} V_\infty A_{DIV} \sin^{P+1} (\Phi)$$

where

$\dot{R}$ = recession rate normal to the surface

K = erosion coefficient

LWC = liquid-water content

ρ_{AB} = density of the material being impacted

V_I = particle impact velocity

V_R = reference velocity

V_∞ = particle freestream velocity

A_{DIV} = correction for divergence of particle mass density for particle impacts on conical sidewalls, A_{DIV} = 1 for normal impacts

Φ = angle of oblique impacts on conical sidewalls, for normal impact $\Phi = 90^\circ$.

N = velocity exponent

P = exponent for oblique impacts

Note that the reference velocity is given only to make the ratio V_I/V_R nondimensional. Thus, when V_I is in kilometers per second, V_R = 1.0 km/sec.

The liquid-water content (LWC) distributions used for each SPLAT calculation were the nominal distributions for precipitation and cloud particles, as presented by Cunningham and Plank (1970) in their preliminary evaluation of the FY71-72 SAMS meteorological data. The distributions for Vehicles 4 and 5 are shown respectively in Figures 4.2.1 and 5.2.1. Because no particle-size distributions have been published for these storms, the LWC for precipitation-size and cloud-size particles were assumed to exist totally in 1-mm- and 25-μm-diameter particles, respectively. Marshall and Palmer (1948) present a number of observations of particle-size distribution which substantiate that the diameters used are reasonable for the mean mass diameters of precipitation and cloud particles.

For the SPLAT calculations, the nose was assumed to possess a constant radius throughout each trajectory. The preflight nosetips had a 16.5-mm (0.65- inch) radius, while the recovered nosetips exhibited nose shapes which were more conical, with a tip radius of 5-7 mm (0.2-0.3 inch). This shape deviation causes the SPLAT calculations with a nose radius of 16.5 mm to underpredict both the particle impact velocities and the recession. Likewise, calculations with the smaller radius overpredict both. The nose-radius effect is minimal for the 1-mm particles, which lose less than 3 percent of their impact velocity in the shock layer associated with a 16.5-mm nose radius and only 1.5 percent for a 5-mm nose radius. The resulting variation in surface recession is less than 14 percent, even assuming that the erosion is proportional to $V^{3.5}$. The nose shape change

greatly affects the impact velocities of the 25-μm-diameter particles, which are computed to lose about 50 percent of their velocity when the nose radius is 16.5 mm and about 18 percent for a radius of 5 mm.

The trajectory data measured in each flight were employed for these SPLAT calculations. Effective erosion coefficients (K) were derived for each velocity model by comparing the calculated recession due to particle impact with the portion of the observed recession attributable to particle impact. To obtain this latter quantity, the nominal recession history observed by the successive losses of ^{182}Ta sources was reduced by the amount due to aerothermal ablation as calculated by the CMA code and shown in Figures 6.2.1 and 6.2.2. Material-density variations were also accounted for by using the time average of the material at the surface for the intervals between source removals.

SPLAT computations with both nose radii produced erosion results which bracketed the actual erosion situation. Table 6.2.1 shows the effective erosion coefficient ranges required to obtain the observed recession between each successive source removal for velocity exponents of 2.0, 2.5, 3.0, and 3.5. In each case the lower bound in K resulted from the calculation with a nose radius of 5 mm and the upper bound with a radius of 16.5 mm. The effective K increases with time for both flights.

It may be possible to correlate the effective K variations with other test parameters. To aid the study of these possibilities, Table 6.2.2, which lists pertinent parameters, has been included. Study of this table suggests that K can be fairly successfully correlated with the particle type and with subsurface material temperatures. Additional data from laboratory experiments and/or flight tests with significantly different trajectories are needed to clarify the dependence of the particle erosion upon any of these parameters.

The overall K derived from comparisons of the SPLAT calculations with the final measured nosetip recession, are shown in Table 6.2.3. As in the previous study, the aerothermal ablation was subtracted from the total recession to obtain the portion attributable to the particle-impact erosion. The material density was assumed to be 1.30 g/cm^3.

TABLE 6.2.1

Effective Erosion Coefficients Versus Time

Vehicle	Time Interval (seconds)	K (g/kJ) N = 2.0	2.5	3.0	3.5
4	0 - 6.45	5.0 - 5.0	3.9 - 3.9	2.9 - 2.9	2.2 - 2.2
	6.45 - 7.32	5.9 - 6.2	3.8 - 4.5	[illegible] - 3.0	1.5 - 2.0
	7.32 - 8.49	6.5 - 8.5	4.3 - 6.0	3.0 - 4.2	1.9 - 2.9
	8.49 - 10.21	10.3 - 24.2	7.8 - 24.2	5.9 - 21.8	18.2
	10.21 -	7.1 - 14.3	6.1 - 17.2	5.1 - 17.2	[illegible]
5	0 - 6.35	4.2 - 5.5	3.1 - 4.0	2.2 - 2.9	1.6 - 2.1
	6.35 - 7.00	5.0 - 6.8	3.6 - 4.6	2.4 - 3.1	1.3 - 2.1
	7.00 - 7.81	5.5 - 7.0	3.8 - 4.8	2.0 - 3.4	1.6 - 2.4
	7.81 - 9.15	6.8 - 10.7	4.9 - 8.6	3.5 - 6.2	2.4 - 4.6
	9.15 -	11.0 - 19.7	8.5 - 15.3	6.7 - 15.3	5.4 - 13.0

TABLE 6.2.2

Test Parameters at Times of Source Removals

Vehicle Number	Time (seconds)	Particle Type	(N/m^2)	$\Delta T/\Delta Z$ $(^oK/m)$	Temperature (^oK) 0.000*	0.051	0.114	0.203	Density ($g/m^3 \cdot 10^{-6}$) 0.000	0.051	0.114	0.203
4	0	Rain	0	0	300	300	300	300	1.449	1.449	1.449	1.449
	6.45	Snow	$2.69 \cdot 10^6$	$9.51 \cdot 10^6$	1544	1061	706	467	1.367	1.439	1.449	1.449
	7.32	Snow	$2.49 \cdot 10^6$	$9.41 \cdot 10^6$	1544	1067	694	472	1.372	1.441	1.449	1.449
	8.49	Transition	$1.59 \cdot 10^6$	$6.45 \cdot 10^6$	1367	1039	744	528	1.399	1.443	1.449	1.449
	10.21	Crystals	$0.89 \cdot 10^6$	$3.94 \cdot 10^6$	1300	1100	894	678	1.375	1.427	1.446	1.449
5	0	Rain	0	0	800	300	300	300	1.449	1.449	1.449	1.449
	6.35	Snow	$2.65 \cdot 10^6$	$10.50 \cdot 10^6$	1428	894	589	433	1.397	1.449	1.449	1.449
	7.00	Snow	$2.60 \cdot 10^6$	$9.84 \cdot 10^6$	1344	844	528	378	1.435	1.448	1.449	1.449
	7.81	Snow	$1.93 \cdot 10^6$	$8.20 \cdot 10^6$	1306	889	600	428	1.433	1.448	1.449	1.449
	9.15	Transition	$1.18 \cdot 10^6$	$5.03 \cdot 10^6$	1428	1172	906	661	1.343	1.413	1.446	1.449

*Distance from surface at stagnation point in millimeters.

TABLE 6.2.3

Erosion Coefficients for Total Stagnation Recession

Vehicle	K(g/kJ) N = 2.0	2.5	3.0	3.5
3	5.7 - 8.9	3.9 - 6.1	2.6 - 4.1	1.8 - 2.7
4	6.4 - 10.0	4.6 - 7.3	3.3 - 5.2	2.3 - 3.7
5	6.0 - 11.7	4.2 - 8.2	2.9 - 5.7	2.0 - 3.9

[redacted]

6.3 Sidewall Recession

In addition to the stagnation point recession, the recession from the sides of both the nosetip and the heatshield also was measured. Postflight diameter measurements were made at five locations along the nosetip and at seven locations along the heatshield. These dimensions were subtracted for the original heatshield and nosetip dimensions to determine the amount of material removed. Figure 6.3.1 is a plot of the thickness of material removed from the sides as a function of the axial distance along the body. A maximum of 2.1 mm (0.083 inch) was lost from the sidewall during Flight 5, with 1.9 mm (0.075 inch) and 1.0 mm (0.040 inch) lost from Flights 4 and 3, respectively. These losses are in contrast to essentially no sidewall recession for a similar clear-air flight. For both the nosetip and the heatshield, the maximum mass loss occurred during Flight 5 and the minimum occurred during Flight 3 at all stations along the body. This order corresponds to that observed for the stagnation point recession.

Based on these data, the erosion of the heatshield sidewall is significantly greater than that of the nosetip sidewall. This response may result from several factors. First, the cone half-angle of the nosetip is $7^{\circ}7'$, while that of the heatshield is 9°. It has been shown experimentally that the surface recession of most materials decreases as the impact angle decreases. Reinecke, McKay, and Waldaman (1972) indicate a dependence on impact angle according to the relationship $G = \varphi(\sin^{1.6}\theta)$. The ratio $(\sin 9^{\circ}/\sin 7.12^{\circ})^{1.6}$ does not account for the observed difference. The reduced effectiveness of the impacts at the lower angle on the nosetip sidewall may be due to the raindrops' tendency to skip off the surface.

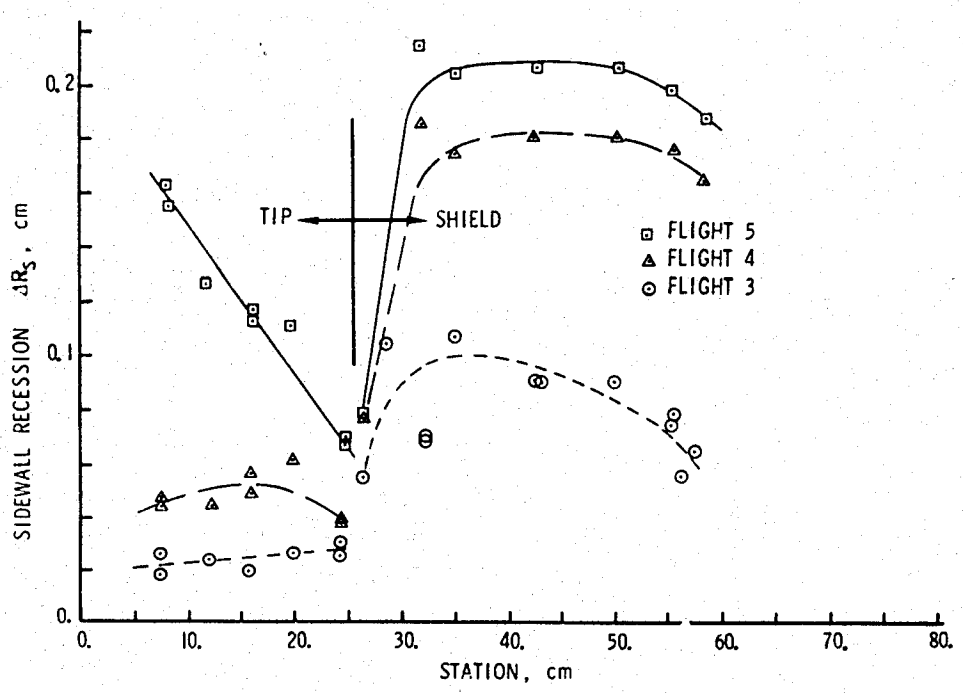

Figure 6.3.1 Sidewall Recession

[redacted] UNCLASSIFIED

Another possible explanation for the increased erosion of the heatshield is a difference in construction between the two sections. Both are carbon phenolic, but the nosetip is a forward-facing, inverted-chevron construction while the heatshield is a shingle-wrapped construction.

Figure 6.3.2 shows the measured radius decrease of the cone sides divided by the measured stagnation point recession and plotted as a function of the axial distance along the model. Since the trajectories of the three flights are nominally the same, one would expect this normalized value to be constant for all flights. For the heatshield section, the values are nominally the same for Flights 4 and 5, but for Flight 3 the ratio is significantly lower. No definite explanation for this can be offered, but two possibilities are the differences between the heatshields material construction and/or the differences in the storms. Storms 4 and 5 were taller, and both possessed more cloud-size particulate and higher average liquid-water content. In addition, a larger portion of the storm reportedly consisted of snow and ice crystals.

For the nosetip, the sidewall-to-stagnation-point recession ratios are higher for Flight 5, while the ratios are nominally the same for Flights 3 and 4. Since this is not the same ordering for the heatshields, one discounts the possibility that the different storm structures cause the difference in the erosion response for the three flights. Therefore the difference in the normalized sidewall erosion apparently results mainly from differences in the material construction between nosetips and between heatshields.

Sidewall recessions for both the nosetip and the heatshield were calculated with the use of the SPLAT code. These calculations were made for the proper half-angles of the nosetip and heatshield sidewalls.

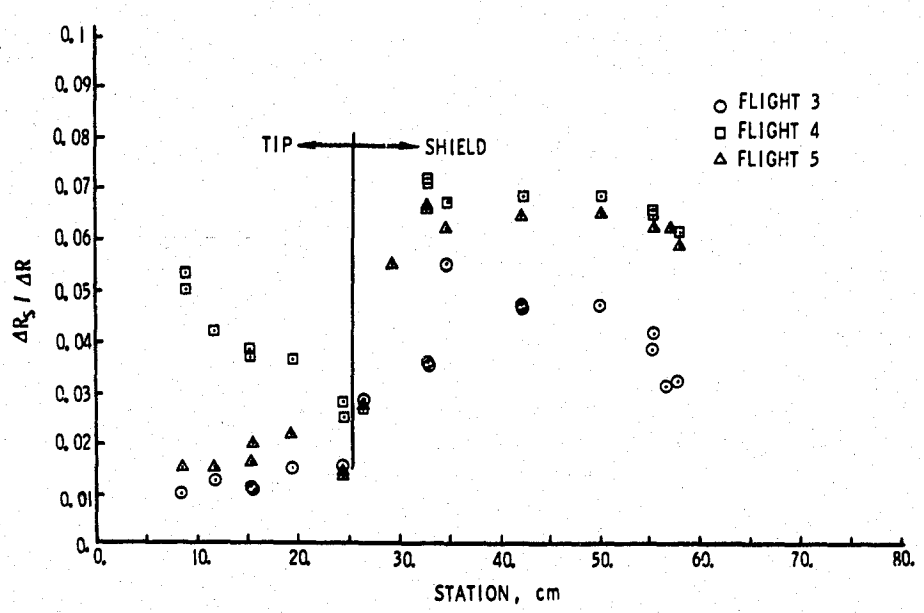

Figure 6.3.2 Sidewall Recession Normalized by Stagnation Recession

Table 6.3.1 presents the effective erosion coefficient values required to obtain the measured recession values assuming a velocity dependence of 2.0 and an angular erosion dependence of sin θ. Since only the final recession value was determined for the sidewall, only an overall erosion coefficient for the entire flight can be inferred. As shown before in Table 6.2.3, the overall erosion coefficients for the stagnation point recession for Flights 3, 4, and 5 are 6.5, 8.2, and 7.4 g/kJ, respectively. For the nosetip sidewall recession, the erosion coefficients vary from 6.2 to 6.9, 7.3 to 10.4, and from 12.1 to 17.8 g/kJ for Flights 3, 4, and 5, respectively. Thus for Flights 3 and 4, the sidewall effective erosion coefficients are similar to the stagnation. values. For Flight 5, however, the coefficient is significantly higher for the sidewall recession, indicating that the nosetip experienced greater sidewall erosion. The explanation for this is not clear, since the stagnation recession on Flights 4 and 5 was essentially the same.

For all three flights, the effective erosion coefficients for the heatshield sidewall are significantly higher than those for the nosetip, based on either stagnation or sidewall recession of the nosetip. Thus the heatshields are clearly less resistant to low-angle oblique impacts than the nosetip. On the aft section of the shield, nearly constant erosion coefficients of approximately 40 g/kJ are obtained for Flights 4 and 5 and values near 20 g/kJ for Flight 3. Near the nosetip-heatshield junction, the erosion coefficient is significantly reduced to values from 12 to 14 g/kJ for all three flights.

TABLE 6.3.1

Effective Erosion Coefficients for Sidewall Recession*

Station (cm)	Flight 3	Flight 4	Flight 5
19.3	6.2	10.4	17.8
24.4	6.9	7.3	12.1
25.8	TIP/SHIELD JUNCTION		
26.7	12.7	14.9	14.5
28.5	25.1	23.9	--
32.5	17.0	37.4	40.8
35.0	26.9	36.2	39.8
42.6	23.4	39.7	43.0
50.2	24.5	41.6	45.1
55.3	21.5	41.9	44.1
57.9	17.0	40.0	42.0

*Assumed u^2 velocity dependence and sin θ dependence

One explanation which immediately comes to mind, in considering the high erosion of the nosetip sidewall compared to that which would be expected based on stagnation point recession, is the assumed angular dependence for oblique impact effects. Experimentally determined values of the nosetip sidewall recession are consistently between sin θ and $\sin^2 \theta$, with $\sin^{1.6} \theta$ as a typical value.

[redacted]

Table 6.3.2 presents the effective erosion coefficients for Flight 4 for both $\sin\theta$ and $\sin^2\theta$ distribution and velocity dependence of 2.0, 2.5, 3.0, and 3.5. For equal velocity dependence, the coefficients are larger in all cases for the $\sin^2\theta$ dependence. Therefore, increasing the angular dependence from $\sin\theta$ to a value typical of that determined experimentally does not explain the high nosetip sidewall recession. For equal angle dependence, the calculated erosion based on a velocity dependence of 2.5, 3.0, or 3.5 is higher than for a dependence of 2.0. While this increase is significant, it cannot account for the observed recession when one recognizes that experimental data indicate that a velocity dependence of 3.0 or 3.5 is too high in this velocity regime.

The SPLAT calculations predict that the thickness of material eroded from the sidewall of a cone increases as one moves from the base of the cone toward the stagnation region. The measured data shown in Figure 6.3.1 are not inconsistent with this trend, but the scatter is such that the calculated trend cannot be positively verified.

One interesting feature of Figure 6.3.1 and Table 6.3.2 is the apparent low erosion of the heatshield immediately behind the joint between the nosetip and the heatshield. Apparently the change from a $7^\circ 7'$ to a 9° cone half-angle sufficiently affects the flow over the cone to partially deflect particles from the forward end of the heatshield. For all three flights, the erosion coefficient at the forward region of the heatshield was of the same order as the nosetip sidewall.

TABLE 6.3.2

Effective Sidewall Erosion Coefficients, Flight 4

	Erosion Coefficient, g/kJ							
Station	$G \sim u^{2.0}$		$G \sim u^{2.5}$		$G \sim u^{3.0}$		$G \sim u^{3.5}$	
Station	$\sin\theta$	$\sin^2\theta$	sin	$\sin^2\theta$	$\sin\theta$	$\sin^2\theta$	$\sin\theta$	$\sin^2\theta$
24.4	10.4	67.6	5.1	36.4	3.5	24.9	2.4	16.9
25.8	TIP/SHIELD JUNCTION							
26.7	14.9	108.2	10.4	74.8	8.7	51.1	4.8	34.5
32.5	37.4	272.9	26.2	1[illegible]9.2	18.0	127.7	12.2	86.6
35.0	36.2	259.8	25.0	179.0	17.1	121.9	11.6	82.3
42.6	39.7	283.9	27.4	195.1	18.7	132.6	12.7	89.3
50.2	41.6	296.4	28.7	203.3	19.6	137.9	13.2	92.8
55.3	41.9	297.6	28.8	203.8	19.6	138.2	13.2	92.8
57.9	40.0	283.8	27.5	194.3	18.7	131.7	12.6	88.5

[redacted]

7.0 Conclusions

1. Three Terrier-Recruit rocket vehicles carrying carbon-phenolic nosetips and heatshields were successfully tested in storms at Wallops Island during the FY72 SAMS Program. Adequate radar tracking data were obtained for each vehicle. Although difficulties were experienced with the telemetered nosetip recession data on the first test, the other data telemetered for the first flight and all of the telemetry data for the other two were satisfactory. All three instrumented payloads, test nosetips and heatshields were recovered from the ocean.

2. Stagnation point recessions were measured to be 1.93 cm (0.76 inch), 2.82 cm (1.11 inches) and 3.02 cm (1.19 inches) respectively for Vehicles 3, 4 and 5. Erosion calculations, assuming the mass loss to be proportional to the particle impact kinetic energy, required erosion coefficients of 4.7-6.5, 6.4-8.2 and 5.8-7.4 g/kJ respectively to match the observed recessions.

3. Aerothermal calculations for Vehicles 4 and 5 showed that the surface material in the nosetip stagnation regions attained temperatures over 1250°C (2280°F), but nearly virgin material densities remained throughout the erosion period.

4. Study of the Vehicle 4 and 5 data indicated that the effective erosion coefficients increased with time. A brief examination suggested that either the near-surface material temperatures or the type of impacting hydrometeors offers possible correlations with these trends. More laboratory experiments and flight tests with different trajectories will be required to further investigate these phenomena.

5. The nosetip sidewall recession data, normalized by the respective stagnation recessions, revealed the Vehicle 5 sidewall recession to be about twice that of Vehicles 3 and 4. Comparisons of the normalized heatshield sidewall recessions indicated a different ordering where Vehicle 3 data were about 70 percent of those for Vehicles 4 and 5. This change in relative ordering between the nosetip and heatshield suggests that variations in material properties among the nosetips and the heatshields were responsible.

6. Sidewall erosion calculations, assuming the mass removal to be proportional to the particle impact kinetic energy and the sine of the impact angle, showed that erosion coefficients of 6.2-17.8 g/kJ were required to produce the observed nosetip sidewall recessions. On the heatshield these coefficients increased to values of 26.9-45.1 g/kJ. These differences between the sidewall recession of the nosetips and the heatshields apparently result from the difference in construction of the materials. The inverted-chevron construction used in the nosetip is more erosion resistant than the shingle-wrap construction of the heatshield.

[redacted]

APPENDIX A

SUPPORT FUNCTIONS AND FACILITIES

[redacted]

[redacted]

(Intentionally left blank)

[redacted]

APPENDIX A

SUPPORT FUNCTIONS AND FACILITIES

A.1 Meteorological Measurements and Support

A.1.1 NOAA Weather Station

The National Weather Service (NWS) of the National Oceanic and Atmospheric Administration (NOAA) operates a weather station with forecast and observation services available 5 days a week, with some additional observation activities on a 7-day-a-week basis. Formal daily weather briefings were provided at 0810 EST, with other consultations available during normal work days on request.

Detailed synoptic weather analyses and forecasts for up to 36 hours were generally presented at the briefings, with 2-to-5-day outlooks also provided. Information of particular interest to the SAMS program included present and forecast positions and trajectories of fronts, cyclones and anticyclones, precipitation regions, and intensification trends of any of these. All of these forecasts represented critical information needed to help decide when to stage a rocket-firing attempt.

Among the equipment used by NWS to provide current weather data was a facsimile recorder connected to the WSR-57 weather radar at Patuxent River. This set provided useful information on precipitation cell distribution within a 125-nautical-mile radius of Patuxent.

Of the routine measurements made by NWS, the ones of particular interest were hourly rainfall collection, at both the station and the Island facility, and upper-air soundings consisting of pressure, temperature, relative humidity, and wind versus altitude.

A.1.2 Weather Radars

The weather radars used for the 1972 flight tests consisted of the Joint Air Force/NASA S-band (JAFNA) radar and the NASA S-band (SPANDAR) radar located about 2 miles west of the island launch area and a NASA S-band (ASR-7) radar located on Wallops Station at Building N-159. The ASR-7 was used exclusively in a horizontal sweep (PPI) mode with a 60-mile range. Its PPI output, transmitted to the JAFNA site via a microwave relay was displayed on a conventional television screen, permitting continual assessment of the storms large scale features. The data from this radar were not recorded.

The JAFNA radar was used for both horizontal (PPI) and vertical (RHI) scans before T-15 minutes. After T-15 minutes the JAFNA radar went exclusively to RHI scans along the 146°T azimuth. The reflectivity data from the JAFNA radar were recorded directly on videotape by an Ampex FR-900 recorder and, in reflectivity-versus-range scope form, on 35-mm photographic film. An electronic apparatus, described by Glover (1972) as a digital video integrator (see Appendix F) was used to average, range-normalize, and contour the radar reflectivity data. This

information was output on a cathoderay tube in nearly real-time RHI displays in which preselected intensity bands of reflectivity were represented by a prescribed shade of gray. These contoured displays were recorded on 35-mm photographic film. A more detailed description of the JAFNA radar is contained in Facilities for Atmospheric Research, No. 11, December 1969, published by NCAR Facilities Laboratory, Boulder, Colorado.

The SPANDAR radar was used as a supplementary instrument. Fixed in azimuth at 146°T and at an elevation angle of 5° or 20°, it made scans in range only. The reflectivity-versus-range (A-scope) data obtained were displayed via an inking pen recorder.

A.1.3 Sampler Aircraft

Airborne sampling of the storm system was initially scheduled to be performed by the AFCRL C130, as it was during the 1971 test series. However, the C130 suffered a major breakdown in January 1972 and was replaced by an instrumented Piper Aztec through a Defense Nuclear Agency (DNA) contract with Meteorology Research, Inc., Altadena, California. The Aztec was equipped with the following instruments of prime interest to this project: (1) an air-temperature sensor, (2) a J-W hot-wire LWC sensor for cloud droplets (<40 μm diameter), (3) a formvar film-particle replicator for liquid particles with diameters of 8-70 μm and ice particles with dimensions of up to 200-300 μm, and (4) a foil impactor for particles with diameters > 150 μm. The air temperature, J-W output, aircraft altitude and a time base were recorded by an oscillograph. Observer and pilot comments were recroded by a standard tape recorder.

The MRI Aztec operated from Wallops Station. A typical flight plan called for the aircraft to take off at T-1 hours and climb toward its maximum altitude (~ 20,000 ft) after reaching a race-track holding pattern east of the southern tip of Assateague Island. The aircraft carried a C-band radar transponder, which aided NASA radar in identifying and tracking the Aztec through its flight operations around Wallops.

When a vehicle launch occurred, the aircraft was directed to proceed to the test area, where a systematic altitude-changing sampling pattern was flown in the vicinity of the vehicle's trajectory. After completing the sampling operation, the aircraft returned to Wallops Station or an alternate, depending on the local landing conditions.

A.1.4 Ground-Based Instruments

The primary meteorological instruments used to help quantify the character and intensity of rain storms were weighing rain gages, tipping-bucket rain gages, and recording raindrop-size distribution meters, or "distrometers." The NWS operated standard 8-inch-diameter weighing/recording rain gages at Wallops Station and at the Island Meteorological Facility (IMF). In general these were used to record total daily collection; in addition, the record from the IMF was tabulated on the basis of hourly collections by NWS.

Applied Physics Laboratory (APL) operated similar weighing rain gages at JAFNA, at the launch site, and at the old Coast Guard Station shown in Figure A.1.4. They also operated tipping-bucket rain gages at the launch site and JAFNA. The data from these latter gages were transmitted by hardwire directly to JAFNA, where they were recorded by a multichannel recorder. All of the

[redacted]

rain gages were modified to increase their sensitivity and resolution by adding large collecting funnels (25-1/4 inches in diameter, or 10 times the original area). The gears in each weighing gage were changed so that the chart drum made a revolution every 6 hours.

The drop distrometers were of Swiss design, supplied on loan through AFCRL. The transducer consisted of a 10-cm-diameter disc mounted to intersect falling drops at the ground. The momentum of each drop was converted to electrical impulses through a pair of coils concentric to a magnet extending downward from the disc. Signals were recorded continuously on magnetic tape and later processed by digital computer to yield drop spectra, rainfall rate, calculated radar reflectivity, LWC, and median diameters.

The rain gages and distrometers were designed for operation in rain, not snow. Some raingage data could be retrieved from snow if it could be determined that snow melted on contact with the funnel; however, distrometer response to snow is essentially unknown.

The potential-gradient meter, or field mill, measured the atmospheric electric field due to space charge accumulation in air and on cloud and precipitation particles. The sensor was mounted within 100 feet of the launch pad, just inland from the sand sea wall. The strip chart recorder, installed in the block house, was used to measure possible electrical effects produced by and on the rocket fired into stormy weather. Its record should indicate lightning strikes that might have a damaging effect on the rocket. The record was also used to monitor the electrical features of the storm before firing.

[redacted]

[redacted]

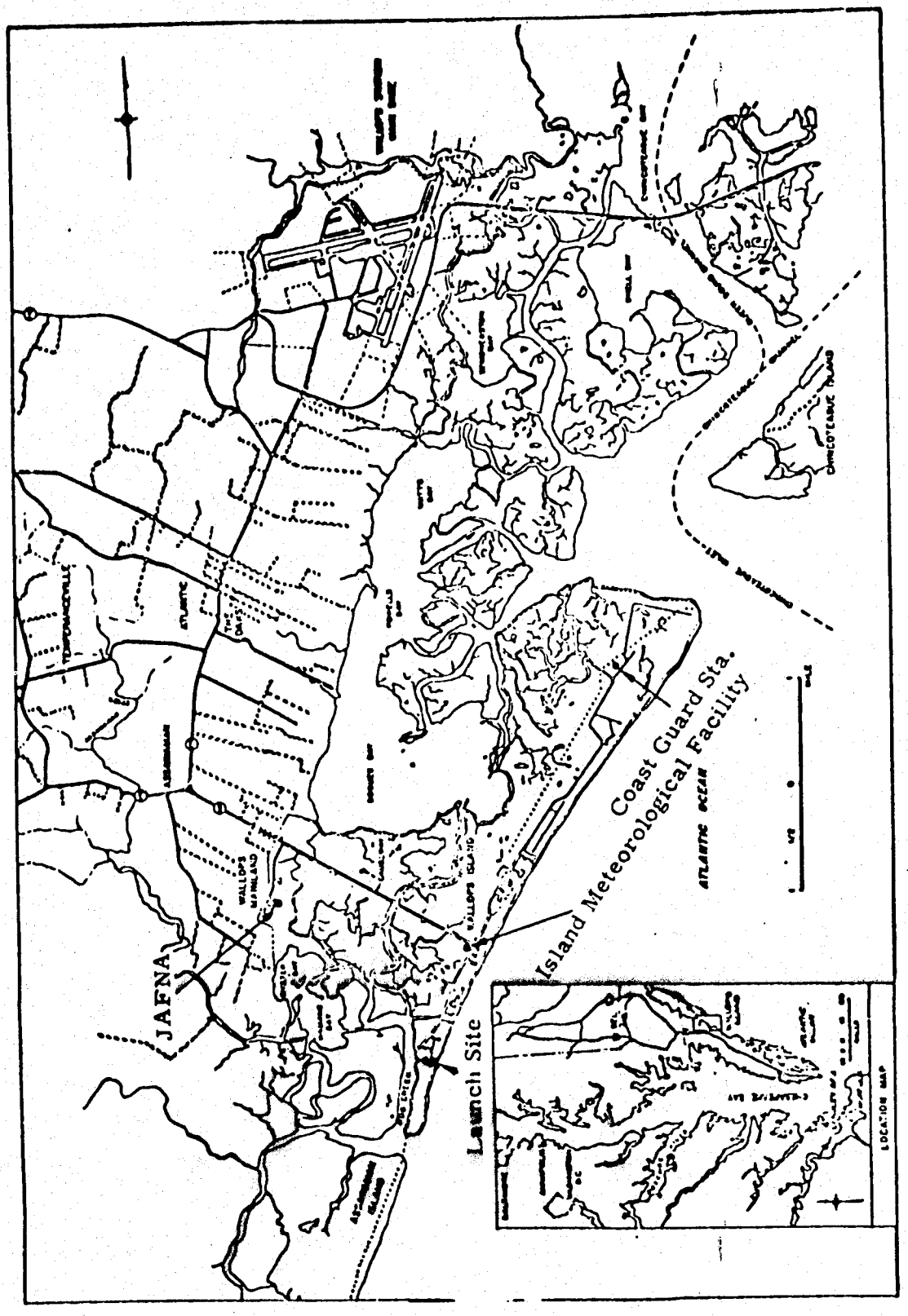

Figure A.1.4 Map of NASA Wallops

[redacted]

TABLE A.1

NASA Wallops Support Facilities

Facility	Function	Location	Data	Description
Radar				
AN/FPQ6	Payload tracking	Wallops Mainland Lat. 37.86°N Long. 75.51°W	a. Analog plot b. Digital listing	C-band instrumentation radar 29' parabolic ant. -113 dbm sensitivity
AN/FPS 16	Payload tracking	Wallops Island Lat. 37.84°N Long. 75.49°W	a. Analog plot b. Digital listing	C-band instrumentation radar 12' parabolic ant. -110 dbm sensitivity
SPANDAR	Cloud reflectivity	Wallops Mainland Lat. 37.85°N Long. 75.51°W	a. A-scope plot.	S-band instrumentation radar 60' parabolic ant. -117 dbm sensitivity
JAFNA/S	Could reflectivity	Wallops Mainland Lat. 37.86°N Long. 75.51°W	a. A-scope photo. b. Contoured or non-contoured RHI/PPI reflectivity photo.	S-Band Radar Atmospheric Research Facility 60' parabolic ant. -112 dbm sensitivity
JAFNA/X	Could reflectivity	Wallops Mainland Lat. 37.86°N Long. 75.51°W	a. Signal strength vs range plot b. Pointing angles	X-Band Radar Atmospheric Research Facility 30' solid parabolic ant. -106 dbm sensitivity
AN/MPS19	a. A/C track b. Wind balloon c. Clood reflectivity (coarse) d. Radiosonde receiver	Wallops Mainland Wallops Island	a. Analog plot b. Digital listing	S-Band Tracking Radar 10' parabolic ant.
Telemetry	Telemetry receiving, [illegible] demodulation, and display	Wallops Station	a. Analog tape recording b. Oscillograph recording	a. P-band, medium gain, self tracking receiving antenna: 18 db gain. b. Multi-band, high gain, self tracking, receiving antenna 60' parabolic 28 db gain (2nd shot only) c. Misc. demodulation, decommutation, and display
Recovery				
C-54	a. Radar controller search A/C b. Recovery beacon D.F. receiver			
Bell 204 Helicopter	a. Recovery of floating payload			a. Contract aircraft from Petroleum Helicopters

[redacted]

TABLE A.1 (cont)

Facility	Function	Location	Data	Description
Physical				
Launcher Pad Zero	Rocket launching facility	Pad O Wallops Island Lat. 37.83°N Long. 75.49°E	AZ/EL readout	a. HAD Launcher b. ARC Launcher (Enclosed before launch) attempt)
Z-40	Blockhouse	Adjacent to Pad O, Wallops Island	-	-
Z-41	Assembly building	Adjacent to Pad O, Wallops Island	-	-

[redacted]

[redacted]

UNCLASSIFIED

APPENDIX B

TERRIER-RECRUIT ROCKET SYSTEM

UNCLASSIFIED

[redacted]

[redacted]

(Intentionally left blank)

[redacted]

APPENDIX B

TERRIER-RECRUIT ROCKET SYSTEM

B.1 System Description

The Terrier-Recruit is a two-stage solid-propellant rocket system (Figure B.1). The first-stage motor is a Mark 12 Mod 0 Advanced Terrier booster and the second-stage motor is a TE-M-29-1 Recruit. The standard 11.5-inch-diameter Recruit nozzle is extended to an exit-plane diameter of 16 inches for greater propulsive efficiency. Four M5E1 Nike aluminum fins are installed in the Terrier fin adapter to aerodynamically stabilize the complete Terrier-Recruit system. A 9.2-degree half-angle conical flare is attached to the Recruit motor for second-stage stabilization.

The interstage adapter is an aluminum-alloy blowout diaphragm with a design pressure differential of 65 psi for diaphragm collapse. This type of interstage adapter allows the second stage to ignite and the first stage to separage during tailoff of the Terrier motor. This adapter design, which has a good effective modulus of rigidity, does not degrade the vehicle's aeroelastic properties. The Terrier/Recruit payload, attached to the second-stage motor with a vee-band clamp, is explosively released at the time of payload separation.

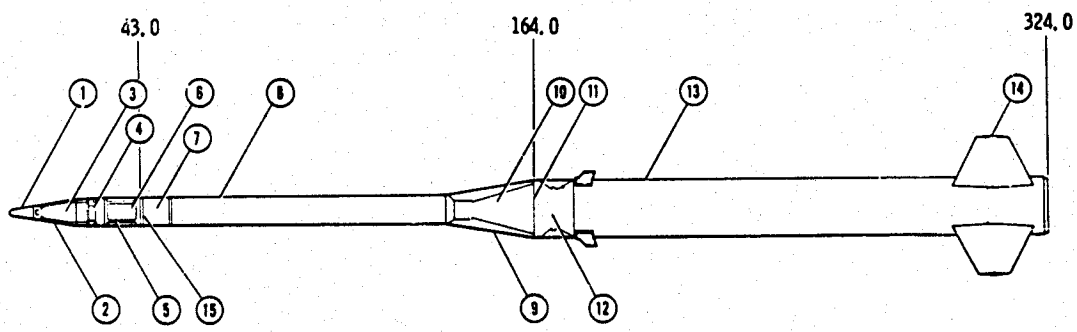

Dimensions in Inches
(Nose is station 0.0)

① NOSE TIP	⑥ RECOVERY SYSTEM	⑪ BLOW-OUT DIAPHRAM
② HEAT SHIELD	⑦ PAYLOAD ADAPTER	⑫ INTERSTAGE ADAPTER
③ INSTRUMENTATION/TM SYSTEM	⑧ RECRUIT MOTOR	⑬ TERRIER MOTOR
④ C-BAND TRANSPONDER	⑨ FLARE	⑭ FIN (2.5 FT^2)
⑤ TM ANTENNA	⑩ EXTENDED NOZZLE	⑮ SEPARATION BAND

Figure B.1 Terrier-Recruit Rocket System

The Terrier-Recruit system requires thermal protection because of the extreme aerodynamic heating environment during flight. The maximum cold-wall stagnation heating rate calculated for a nominal flight is 2120 Btu/ft^2-sec. The leading edge of each first-stage fin is protected with a stainless-steel cap. The maximum cold-wall heating rates on the conical section of the payload aft of the heatshield and on the cylindrical section of the payload are calculated to be 440 and 240 Btu/ft^2-sec, respectively. The maximum rate on the flare is 550 Btu/ft^2-sec. The conical section of the payload is protected with shingle-wrapped phenolic-glass tape (0.2 inch in total thickness), and the cylindrical section of the payload and the Recruit motor are protected with 0.050-inch thickness of an epoxy- and silicone-based low-temperature ablator.* The flare, machined from an aluminum-alloy casting, is protected with a 0.050-inch-thick phenolic-glass shingle wrap and an 0.20-inch-thick overcoat of the DE-350 ablative material. A fiberglass batting is placed around the Recruit nozzle to protect the flare from radiant heating. Maximum flare temperature observed during a Terrier-Recruit flight test was 275°F.

B.2 Aerodynamics

Four double-wedge M5E1 Nike fins, of 2.5-ft^2 platform area per panel, are employed to aerodynamically stabilize the Terrier-Recruit first-stage vehicle. The Nike fins cause less weight and drag penalty than do the standard Terrier fins (3.5 ft^2 per panel), and give adequate stability to the first-stage configuration. The minimum static margin for the complete Terrier/Recruit system, computed from wind-tunnel data, is 16 percent of the body length and occurs at Terrier burnout.

A 9.2-degree half-angle conical flare, expanding from 9 to 18 inches in diameter, is used to aerodynamically stabilize the Recruit second-stage vehicle. A minimum static margin of 6 percent of body length (from wind-tunnel data) occurs as the Recruit separates from the Terrier; the margin at maximum velocity is 15 percent. Angles of attack observed from flight data on the second stage have been 1.0 degree at Recruit separation and 0.1 degree at maximum velocity.

Aerodynamic flow disturbances along the second-stage vehicle are kept minimal. No initial protuberances exist, all payload joints are smooth, and the umbilical recess is covered with a spring-loaded door. Postflight inspection of the recovered payload and a retrieved Recruit motor indicates that the vehicle's external surface remains relatively smooth, with no peeling of ablative material.

B.3 Payload

B.3.1 General

The payload structure consists of an aluminum conical frustum and cylinder which are covered by heatshields of glass phenolic and DE-350, respectively. To this is added a test nosetip and heatshield, which make the final configuration approximately a sphere-cone-cylinder. The payload structure contains the nosetip recession instrument, the flight-dynamics instruments, thermal sensors,

*DE-350, Sparesyl, a product of the Dyna-Therm Corp., Los Angeles, California.

the vehicle sequence controls and monitors, a radar transponder and antennas, a telemetry system and antenna, a parachute recovery system and the electrical power supplies. Figure B.2 shows the payload.

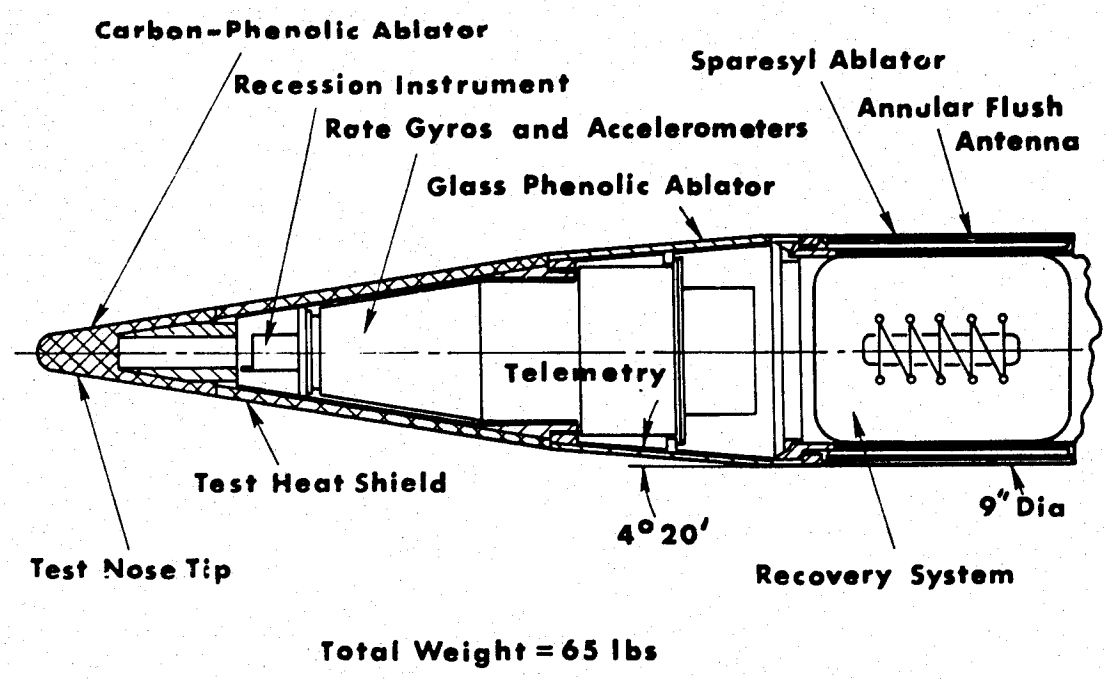

Figure B.2 Instrumented Payload

B.3.2 Payload Instrumentation and Related Systems

B.3.2.1 Payload Telemetry

The telemetry system employed is a PAM/FM/FM system, transmitting on 248.6 MHz. The transmitter is a conic CTM-402 utilizing a nominal 500-kHz bandwidth and radiating a nominal 2-watt signal.

In addition to the channels listed in Table B.1, the video band from dc to 20 kHz is utilized to transmit a standardized pulse rate proportional to the raw count rate at the output of the photomultiplier in the recession instrument.

The primary instrumentation consists of a scintillator-photomultiplier sensor that views gamma-ray sources located within the nosetip, and that, together with an axial accelerometer, affords time histories of velocity and nosetip recession. The balance of the instrumentation provides vehicle dynamics, thermal, and diagnostic information. Times are correlated by recording a NASA time-code signal on the telemetry magentic tapes.

TABLE B.1

Telemetry Channel Assignments

Subcarrier	Information
30.0 kHz ± 7.5%	Nosetip recession (8 sources)
40.0 kHz ± 7.5%	Acceleration, longitudinal (X-axis)
70.0 kHz 15%	PAM 30 ch x 80 frames/sec
Chan 1	Zero cal
Chan 2	Full-scale cal
Chan 3, 18	Rate, X-axis ± 400°/S
Chan 4, 19	Rate Z-axis ± 90°/S
Chan 5, 20	Rate, Y-axis ± 90°/S
Chan 6, 21	Acceleration, X-axis -50 to ± 150 g
Chan 7, 22	Acceleration, Y-axis ± 50 g
Chan 8, 23	Acceleration, Z-axis ± 50 g
Chan 9, 24	Nosetip recession
Chan 10, 25	Bridgewire, fire signal monitor
Chan 11	Temp No. 1
Chan 12	Temp No. 2
Chan 13	Temp No. 3
Chan 14	Temp No. 4
Chan 15	Capacitor bank voltage
Chan 16	TLM voltage monitor
Chan 17	22 V regulator monitor
Chan 26	Timer monitor
Chan 27	Separation/baroswitch monitor
Chan 28	G-switch monitor
Chan 29, 30	Frame sync

The telemetry system is operated from blockhouse power supplies or self-contained batteries by means of a latching power-control relay. The 28-volt, 1.2-amp/hr, nickel-cadmium, sealed-cell batteries have a life of about 1/2 hour under their nominal 2-ampere load. They are charged through umbilical circuits at a constant 120-milliamp rate for 16 hours. The system is operated for a minimum of 3 to 5 minutes from ground power before launch to allow stabilization of the sensors. At approximately T_o minus 2 minutes, the system is switched to internal power in preparation for launch.

B.3.2.2 Payload Beacon

A C-band radar transponder is used to enhance radar tracking; the beacon operates whenever the telemetry system is on. The transponder employed is a Motorola Model SST-171C with the following characteristics:

RCVR frequency	5690 MHz ± 3 MHz
SENS . DBM	-65 min.
Xmtr. frequency	5765 MHz ± 3 MHz
Transponder delay	2.0 μsec ± 0.09 μsec
Reply pulse width	0.5 μsec ± 0.1 μsec
Peak power output	400 watts min. at 1 kHz rep. rate
Double pulse spacing	6.0 μsec. ± 0.25 μsec.

B.3.2.3 Payload Antenna

The VHF telemetry antenna is a cavity-backed annular slot located in the payload recovery section at vehicle station 33.91 inches. Polarization is predominantly linear along the longitudinal dimension of the vehicle, resulting in a nearly symmetrical pattern about the roll axis.

The C-band beacon antenna is an array of three right-hand circularly polarized helices equally spaced about the circumference of the payload at station 31.1 inches.

B.3.2.4 Recession Instrumentation

The nosetip recession sensor, TC564, uses a scintillator/photomultiplier system to detect eight radioactive ^{182}Ta sources installed at prescribed locations in the nosetip. As the nosetip undergoes surface recession during the flight, the sources are sequentially exposed and swept away by the airstream. The sensor notes the loss of each by a decrease in the measured radioactivity, and this information is telemetered. The ^{182}Ta sources are located in each nosetip as shown in Figure 3.4.1.

The TC564 has two outputs: a filtered dc voltage as the main output, and a secondary output consisting of a pulse train with a variable repetition rate. Both outputs are proportional to the intensity of the incident gamma; that is, the number of sources present. The pulse train output is used to baseband modulate (0-20 kHz) the telemetry transmitter. The dc output modulates subcarrier oscillators, as described in Section B.3.2.1.

The dc output voltage level of the TC564, at any particular time, indicates total radiation from the nosetip sources. With no gamma sources in place (zero gamma input), the TC564 output will be near +5 volts. With maximum gamma input (all eight sources in place), the output voltage will be near zero. Thus maximum radioactivity is indicated by zero volts, and, as sources are removed, the signal moves toward +5 volts, indicating less radioactivity. The output signal is filtered with a time constant of approximately 0.1 second; however, it will still move about the average level in a manner dictated by the statistical nature of the radioactive decay in the sources and the relative position of the fluor and the sources.

B.3.3 Recovery System

The payload recovery system is actuated by a baroswitch closure as the payload descends through an altitude of 15,000 feet MSL. The rear cover of the payload is ejected after a 16-second delay and the first-stage 3-foot guide-surface parachute is deployed. A pyrotechnic timer then gives a 10-second delay before releasing the main canopy, a 6-foot guide-surface parachute. A dual-compartment 3.5-cubic-foot ram-air flotation bag is attached to the vent of the main canopy and is

inflated concurrently with it. A one-way valve located in the mouth of the flotation bag prevents unintentional deflation of the bag. Figure B.3 shows the deployed system. Salt-water switches are closed at water impact to activate a radio beacon and an acoustic pinger. The radio beacon transmits an AM signal at a frequency of 252.4 or 258.5 MHz and has a life of about 22 hours. The acoustic pinger transmits a 30-kHz signal and has a 7-day life. Handling loops are attached around the circumference of the flotation bag to facilitate its recovery.

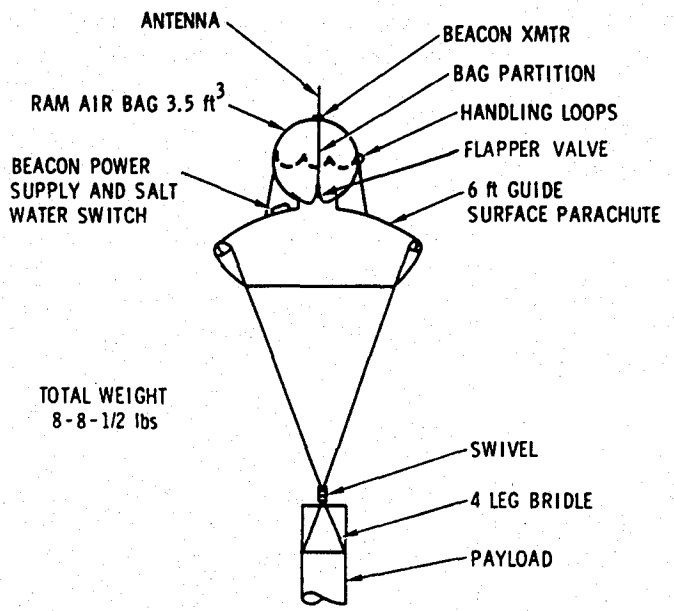

Figure B.3 Payload Recovery System

[redacted]

APPENDIX C

EROSION DATA, VEHICLE 3

[redacted]

(Intentionally left blank)

[redacted]

APPENDIX C

EROSION DATA, VEHICLE 3

C.1 Meteorological Data, Vehicle 3

Synoptic Weather Situation

A well developed winter cyclone was centered at 0700 EST over lower Michigan, with a surface-pressure trough and associated cold front extending southward into the Gulf of Mexico near Biloxi, Mississippi. A quasi-stationary front extending eastward along the 30th parallel through the Florida panhandle had shown signs of a closed low (1005 mb) circulation forming on it near Tallahassee. By 1300 EST (see Figure C.1.1 for surface charts), in association with the approaching and deepening 500-mb trough aloft, the surface low center over Florida had moved to Charleston, S.C., and by 1400 was near Fayetteville, N.C., with a central pressure of 999 mb and a well developed rain shield extending some 500 km (300 miles) to the east and north. Winds aloft had backed around from 250° at 0700 to 215° by shot time, giving rise to a wide area of air-mass lifting as the warm, moist Gulf air from the south was carried northward over the existing polar air mass.

Analysis

Rain began falling at Wallops Island around 1300 and had reached a rate of 2 mm/hr by 1320. Except for a decrease in the rate around 1340 (Figure C.1.2), the rain intensity remained remarkably constant for almost 2 hours preceding launch time. The rate reached 3.5 mm/hr just before shot time and, as later became evident, was in the process of rapidly dropping during shot time to values slightly less than 1 mm/hr.

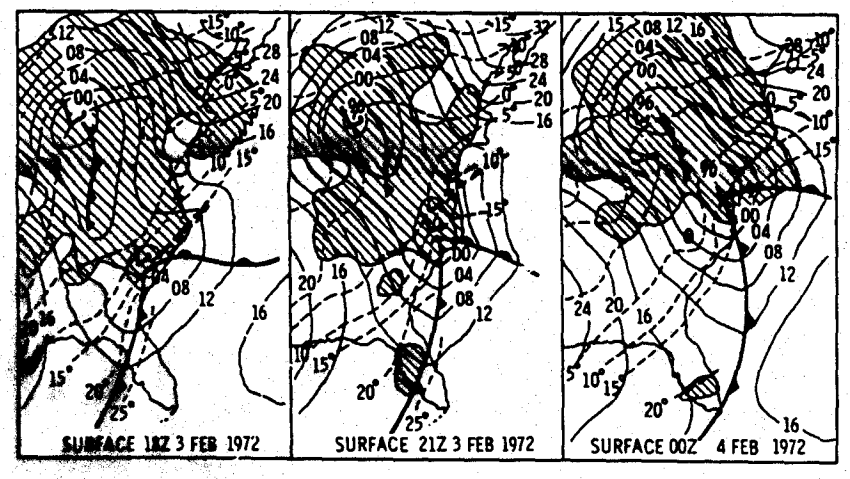

Figure C.1.1 Three Hourly Surface Weather Charts, February 3

[redacted]

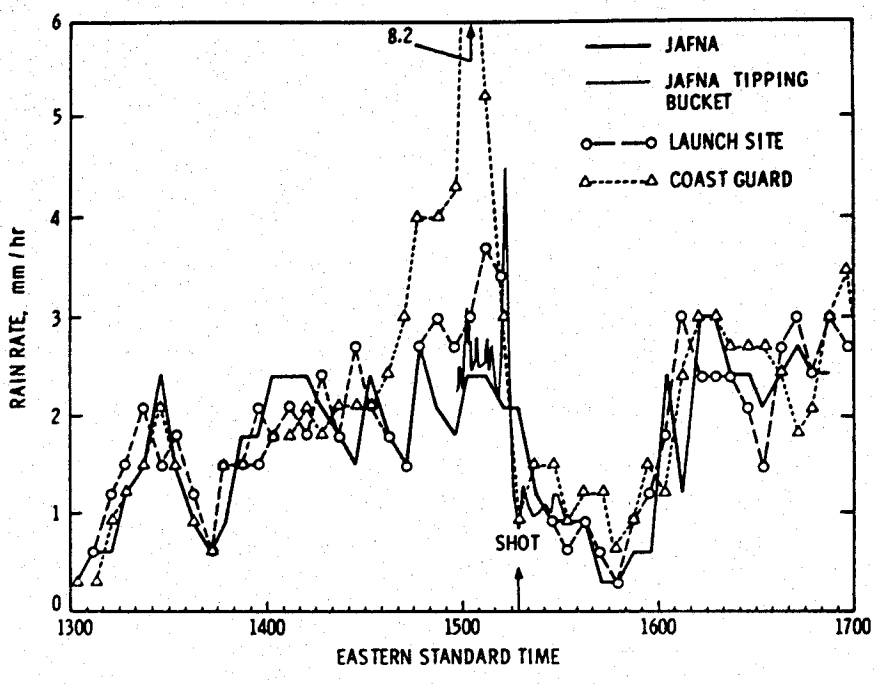

Figure C.1.2 Rain Rate Versus Time, Weighing Gage, February 3

On the first two charts of Figure C.1.1 a heavy dashed line is shown extending to the northeast from the storm center over Carolina; this feature, north of the advancing warm front, is a trough line probably caused by a wave of the quasi-horizontal frontal surface propagating ahead of the warm front. It is likely that the interruption in the rain rate which occurred at shot time was related to this mesoscale weather feature. It would take a careful watch of weather-search PPI scopes and hourly weather reports to be able to detect the approach of such a system.

The rawinsonde balloon, released at 1537 (T + 20 minutes) to record temperature, humidity and wind versus altitude (Figure C.1.4), showed the melt level at 2.75 km (9.0 kft) altitude, while the sampling aircraft indicated melting at 3.10 km (10.2 kft). The JAFNA-S-band radar indicated an enhanced-reflectivity layer, probably due to melt, at 2.5 km (8.2 kft). Figure C.1.5 shows radar-reflected power profiles normalized to 1.85-km (1-nmi) range versus height along the rocket trajectory. Two profiles are shown, one derived from the digitized tape-recorded data, and the other as derived by AFCRL from the video integrator-contoured RHI photographs. See Appendix G for a discussion of the difference between these profiles and for some comments on confidence limits. Figure C.1.6 shows a computer-contoured RHI from the tape-recorded data.

By using the radar reflectivity-liquid water content (Z-M) relations and the best estimates of hydrometeor-type-versus-altitude description supplied by AFCRL from analysis of aircraft and radar data, the digitized radar reflectivity data were converted to equivalent liquid-water content and are shown as LWC versus altitude along the trajectory in Figure C.1.7. As expected, the -8 to -10 db bias in reflected power makes a significant difference in inferred equivalent liquid-water content.

[redacted]

UNCLASSIFIED

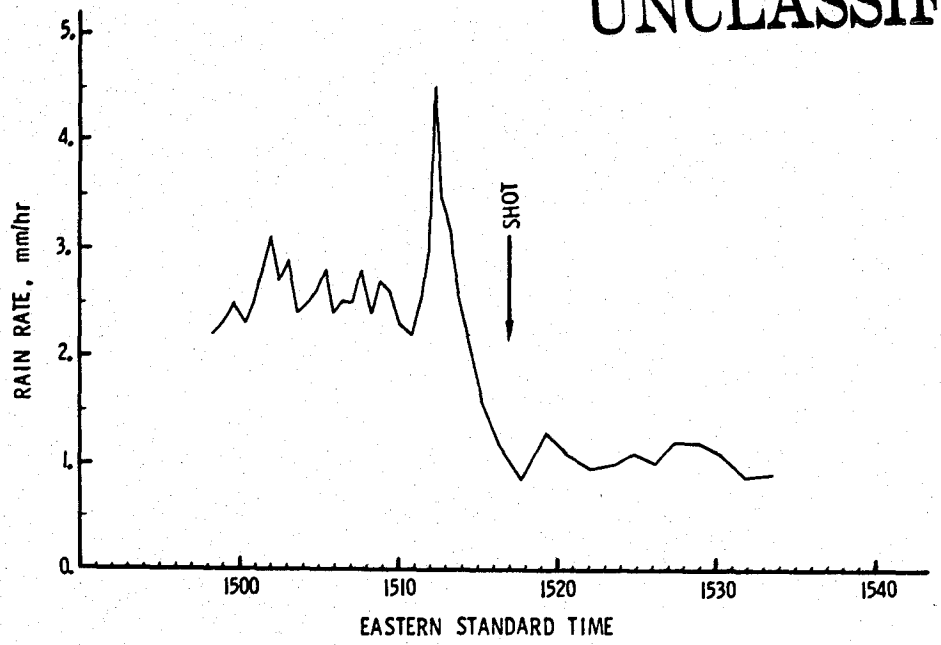

Figure C.1.3 Rain Rate Versus Time, Tipping-Bucket Gage, February 3

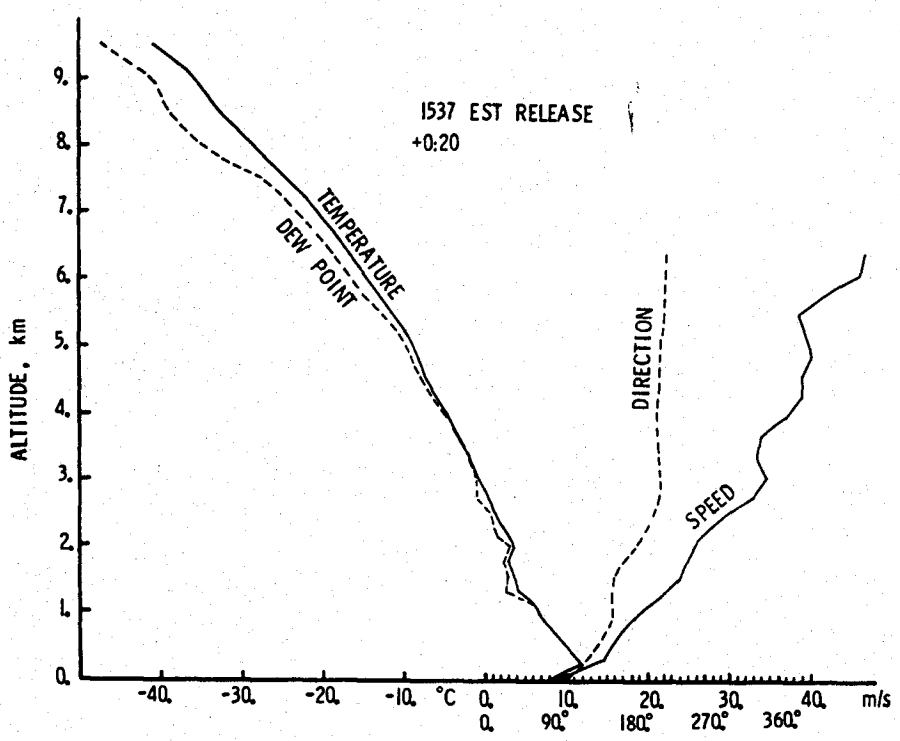

Figure C.1.4 Rawinsonde Observation, February 3

UNCLASSIFIED [redacted]

[redacted]

UNCLASSIFIED

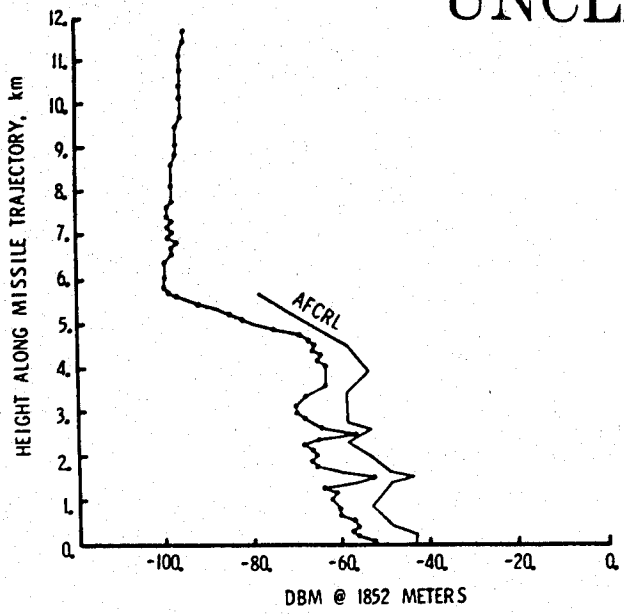

Figure C.1.5 Radar-Reflected Power Profile, February 3

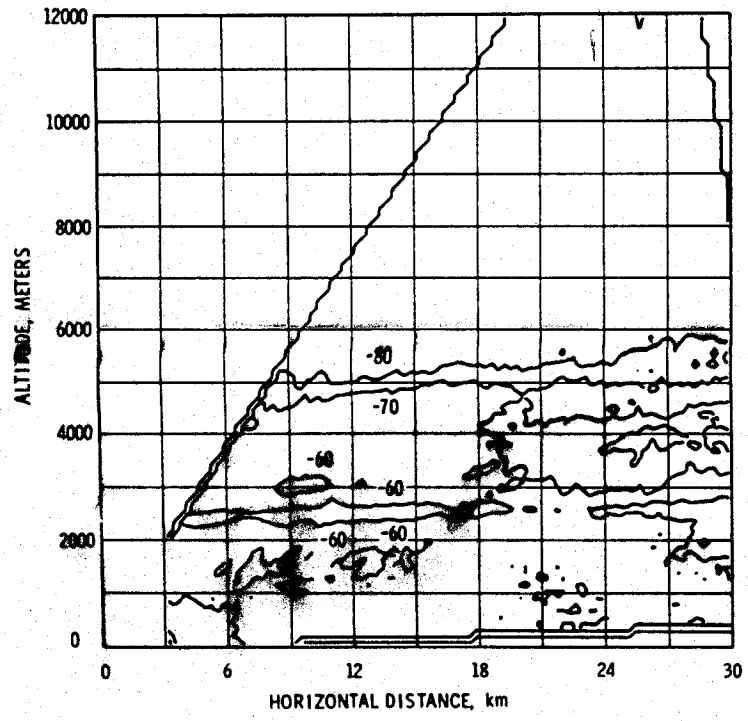

Figure C.1.6 Contoured Reflected Power, February 3

[redacted] UNCLASSIFIED

[redacted]

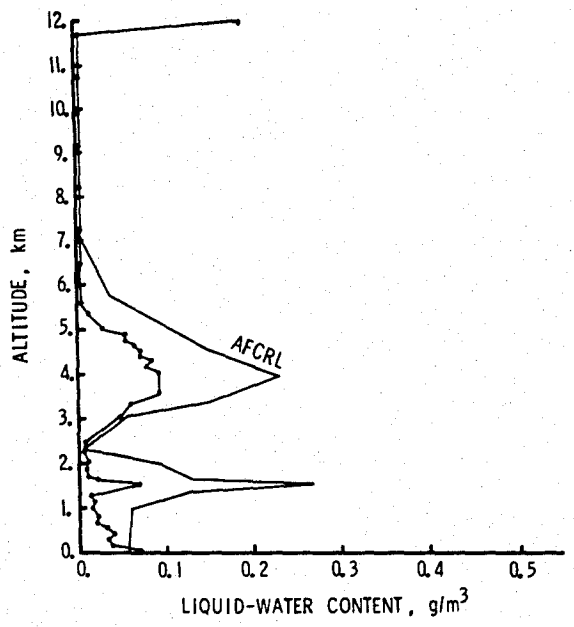

Figure C.1.7 Equivalent Liquid-Water Content Profile, February 3

C.2 Vehicle 3 Performance

The performance of the Terrier-Recruit booster system was nominal during the flight test of Vehicle 3. Vehicle tracking data from the NASA FPQ-6 C-band radar and the telemetered accelerometer data were combined to determine accurate velocity and position histories. The maximum velocity for the test was 2.608 km/sec (8556 fps), only 1 percent below the preflight nominal value. The altitude at maximum velocity was 3.041 km (9976 ft) msl, within 13.4 meters (44 ft) of the nominal altitude for maximum velocity. The vehicle flight path angle was nominal at the time of maximum velocity. The vehicle roll rate was not monitored on this flight, but the monitored pitch and yaw rates were nominal. The event history for this flight test, as well as for Vehicles 4 and 5, is presented in Table C.2.1. The measured velocity-time, altitude-time, and altitude-velocity plots are presented along with the preflight nominals in Figures C.2.1, C.2.2, and C.2.3, respectively. The elevation and plan tracking data are presented with the preflight nominals in Figures C.2.4 and C.2.5. Table C.2.2 contains a tabulation of the trajectory data for Vehicle 3.

Launcher corrections of +1.8 degrees in elevation and +2.5 degrees in azimuth were made to the nominal launcher 35-degree elevation angle and 146°T azimuth angle. An offset in the southwesterly direction, evident in the plan track of Figure C.2.5, resulted from the radar tracking data being reduced for the coordinates of the HAD launcher at Pad 0, rather than for those of the ARC launcher from which the vehicle was launched. The ARC launcher is located 99 m (325 ft) to the southwest of the HAD launcher. The nominal launch azimuth of 146°T was originally determined as the azimuth of the JAFNA radar to the ARC launcher.

[redacted]

UNCLASSIFIED

TABLE C.2.1

Vehicle Performance Summary for Vehicles 3, 4, and 5

Event	Vehicle 3			Vehicle 4			Vehicle 5			Preflight Trajectory Simulation (nominal)		
	Time sec	Altitude ft msl (km msl)	Velocity ft/sec (km/sec)	Time sec	Altitude ft msl (km msl)	Velocity ft/sec (km/sec)	Time sec	Altitude ft msl (km msl)	Velocity ft/sec (km/sec)	Time sec	Altitude ft msl (km msl)	Velocity ft/sec (km/sec)
First-Stage Maximum Velocity	4.3	4332	4154	4.9	4797	4007	4.7	4775	4040	4.6	4642	4195
		(1.320)	(1.266)		(1.462)	(1.221)		(1.455)	(1.231)		(1.415)	(1.279)
Second-Stage Ignition	4.56	4887	4121	5.05	5089	3993	4.89	5168	4019	4.81	5055	4136
		(1.489)	(1.256)		(1.551)	(1.217)		(1.575)	(1.225)		(1.541)	(1.261)
Second-Stage Maximum Velocity	6.22	9976	8556	6.73	10029	8482	6.60	10265	8431	6.41	10020	8645
		(3.041)	(2.608)		(3.057)	(2.585)		(3.129)	(2.570)		(3.054)	(2.635)
Apogee	39.	45860	1020	38.5	44260	1040	39.	45880	1035	39.	45690	1035
		(13.977)	(0.311)		(13.490)	(0.317)		(13.984)	(0.315)		(13.926)	(0.315)
Payload Separation	57.	41280	880.	62.5	35200	875.	54	42680	880.	59.	40330	820
		(12.582)	(0.268)		(10.728)	(0.267)		(13.008)	(0.268)		(12.292)	(0.250)
Baroswitch Operation	129.	14560	355.	118.	15500	335.	127.	15040	325	121.	16000	331
		(4.438)	(0.108)		(4.724)	(0.102)		(4.584)	(0.099)		(4.877)	(0.101)
Pilot Chute Deployment	145.	9860	300.	134.	10700	305.	143	10120	305.	137.	10920	305.
		(3.005)	(0.091)		(3.261)	(0.093)		(3.084)	(0.093)		(3.328)	(0.093)
Main Chute Deployment	155.	7740.	185.	144.	8620	175.	155	7840	185.	147.	8910.	172.
		(2.359)	(0.056)		(2.627)	(0.053)		(2.390)	(0.056)		(2.716)	(0.052)
Impact	294.	0	50.	302.	0	50.	301.	0.	50.	310.	0.	51.
			(0.015)			0.015			(0.015)			(0.016)
T_o, EST	1517:00.35			1012:00.3			1048:00.2					

UNCLASSIFIED

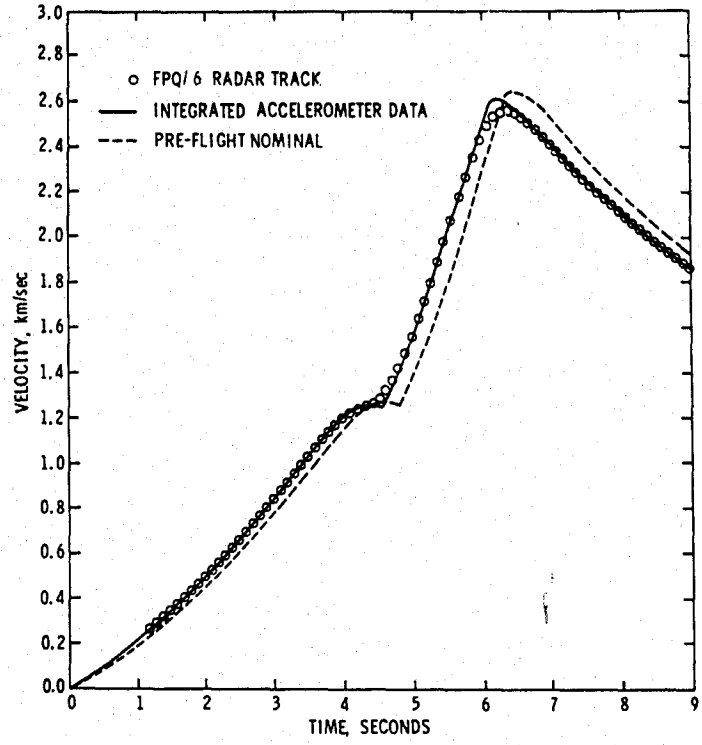

Figure C.2.1a Velocity Versus Time, Vehicle 3

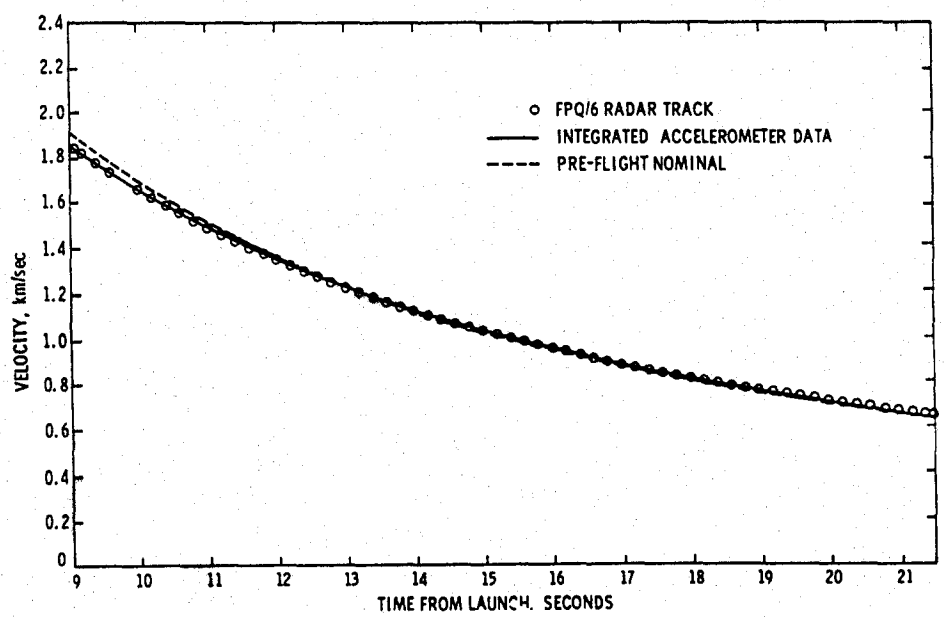

Figure C.2.1b Velocity Versus Time, Vehicle 3

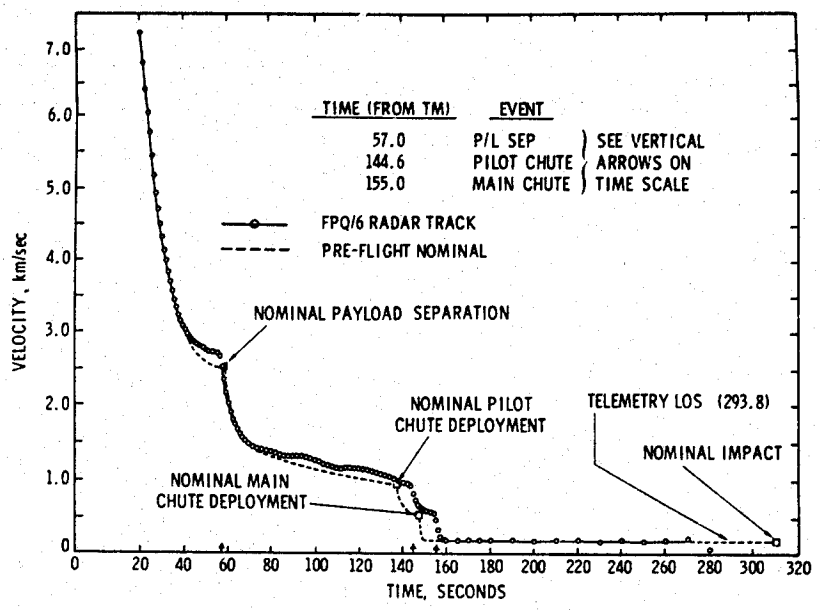

Figure C.2.1c Velocity Versus Time, Vehicle 3

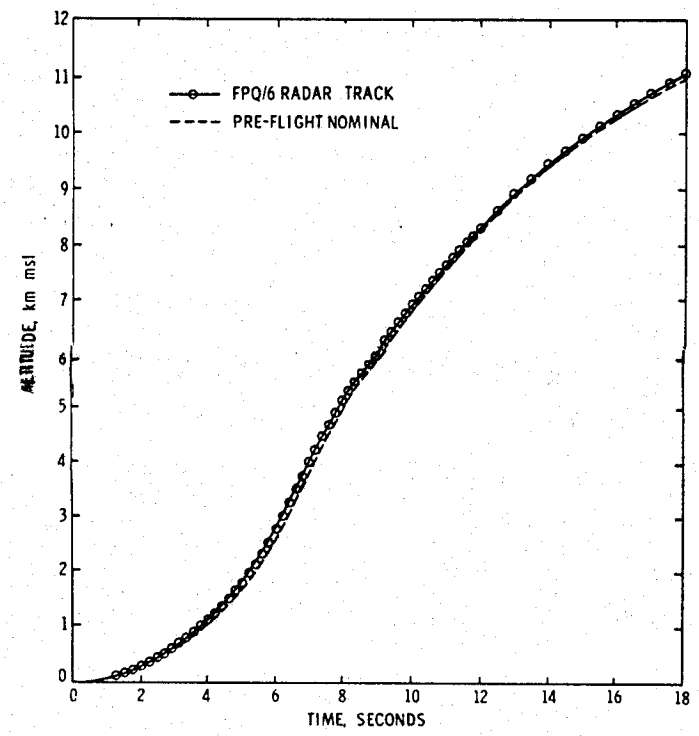

Figure C.2.2 Altitude Versus Time, Vehicle 3

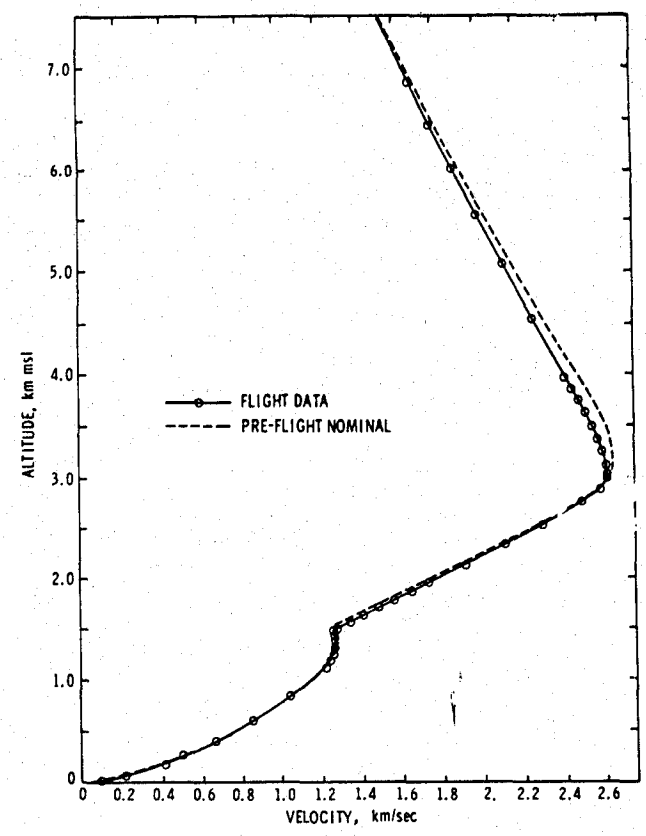

Figure C.2.3 Altitude-Velocity Profile, Vehicle 3

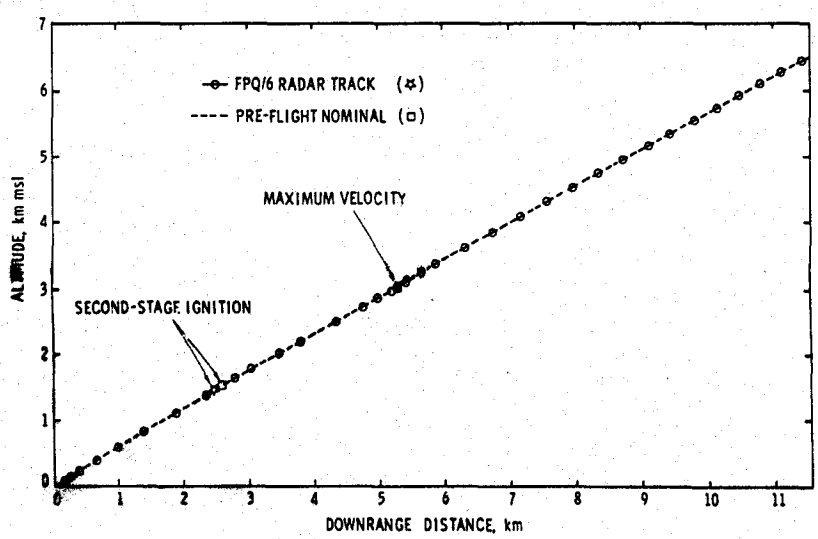

Figure C.2.4a Altitude-Distance Profile, Vehicle 3

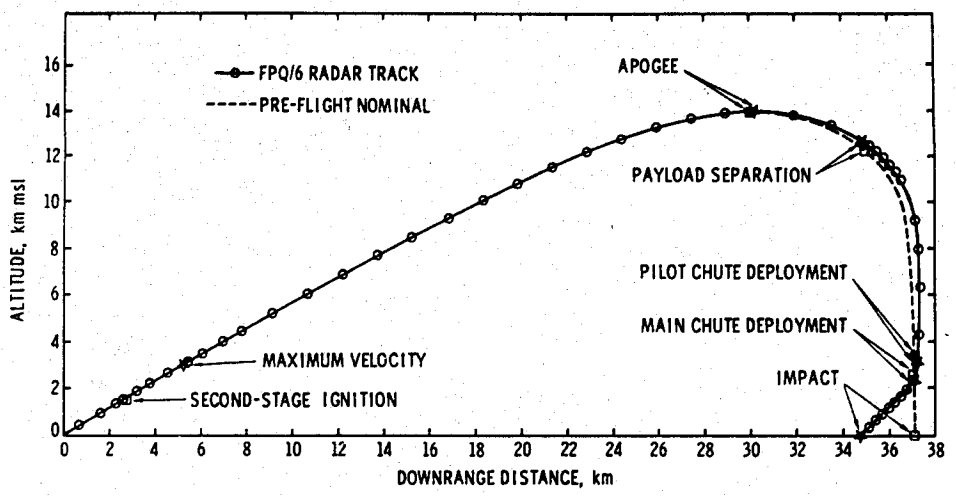

Figure C.4.2b Vehicle 3 Trajectory

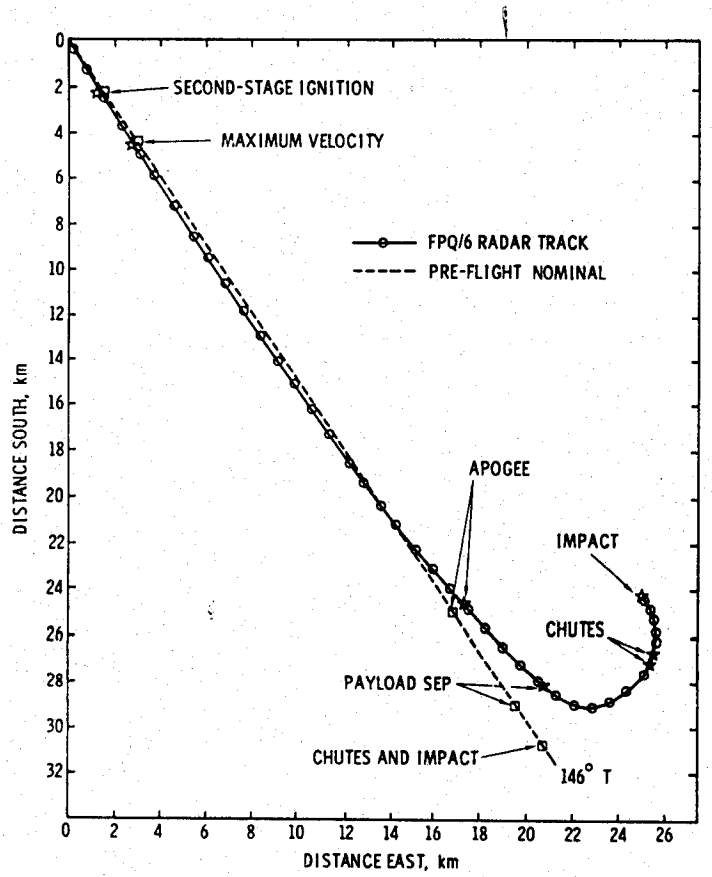

Figure C.2.5 Plan Position Track, Vehicle 3

TABLE C.2.2a

Vehicle 3 Trajectory Data

Time From T_o (sec)	Altitude (ft msl)	Velocity (ft/sec)	Ground Range (ft)
0.5	40	320	67
1.0	180	722	301
1.7	642	1,358	1,072
2.0	879	1,656	1,441
2.5	1,376	2,201	2,248
3.0	2,011	2,794	3,310
3.5	2,795	3,432	4,645
4.0	3,722	4,002	6,243
4.3	4,332	4,154	7,291
4.5	4,756	4,138	8,011
4.56	4,887	4,121	8,232
4.6	4,974	4,186	8,381
4.8	5,429	4,622	9,160
5.0	5,917	5,115	10,010
5.2	6,447	5,677	10,952
5.4	7,028	6,279	11,994
5.6	7,664	6,908	13,143
5.8	8,357	7,516	14,399
6.0	9,105	8,144	15,755
6.1	9,496	8,452	16,464
6.22	9,976	8,556	17,332
6.3	10,300	8,538	17,917
6.5	11,117	8,405	19,381
7.0	13,112	7,894	22,927
7.5	14,974	7,386	26,254
8.0	16,701	6,913	29,371
8.5	18,313	6,492	32,300
9.0	19,821	6,099	35,050
9.5	21,234	5,743	37,644
10.0	22,562	5,421	40,093
11.0	24,988	4,866	44,606
12.0	27,154	4,402	48,686
13.0	29,096	4,006	52,404
14.0	30,848	3,665	55,810
15.0	32,437	3,367	58,944
16.0	33,879	3,107	61,840
17.0	35,183	2,876	64,530
18.0	36,370	2,674	67,041
19.0	37,452	2,496	69,390
20.0	38,444	2,341	71,596

TABLE C.2.2b

Vehicle 3 Trajectory Data

Time From T_o (sec)	Air Density ($lbsm/ft^3$)	Sound Speed (ft/sec)	Dynamic Pressure ($lbsf/ft^2$)	Mach Number
0.5	.0771	1100.6	123.	.291
1.	.0765	1103.4	620.	.654
1.7	.0753	1105.2	2158.	1.229
2.	.0739	1108.0	3149.	1.495
2.5	.0727	1107.0	5473.	1.988
3.	.0714	1103.7	8662.	2.531
3.5	.0698	1100.8	12777.	3.118
4.	.0679	1096.9	16900.	3.648
4.1	.0674	1095.7	17368.	3.716
4.2	.0671	1095.0	17726.	3.765
4.3	.0667	1094.8	17886.	3.794
4.4	.0663	1094.6	17805.	3.798
4.5	.0658	1094.3	17509.	3.781
4.56	.0655	1094.2	17287.	3.766
4.6	.0654	1094.1	17809.	3.826
4.7	.0650	1093.7	19556.	4.023
4.7	.0644	1093.2	21380.	4.228
4.9	.0638	1092.8	23399.	4.445
5.0	.0633	1092.3	25737.	4.683
5.1	.0626	1092.0	28252.	4.935
5.2	.0620	1092.0	31052.	5.199
5.4	.0608	1092.0	37252.	5.750
5.6	.0595	1090.0	44125.	6.338
5.8	.0582	1088.3	51093.	6.906
6.0	.0567	1086.7	58442.	7.494
6.1	.0558	1085.7	61947.	7.785
6.2	.0552	1084.6	62769.	7.887
6.22	.0550	1084.3	62570.	7.891
6.3	.0544	1083.5	61628.	7.880
6.4	.0537	1082.7	60068.	7.836
6.5	.0529	1081.7	58076.	7.770
6.6	.0523	1080.1	56154.	7.696
6.7	.0516	1078.9	54090.	7.612
6.8	.0508	1077.8	51911.	7.524

[redacted]

TABLE C.2.2b (CONT)

Time From T_o (sec)	Air Density ($lbsm/ft^3$)	Sound Speed (ft/sec)	Dynamic Pressure ($lbsf/ft^2$)	Mach Number
6.9	.0502	1077.3	49941.	7.427
7.0	.0495	1076.6	47936.	7.332
7.5	.0464	1070.0	39337.	6.903
8.0	.0438	1067.3	32529.	6.477
8.5	.0415	1062.1	27181.	6.112
9.0	.0395	1056.0	22834.	5.776
9.5	.0377	1050.3	19323.	5.468
10.	.0360	1045.6	16441.	5.185
11.	.0333	1033.3	12253.	4.709
12.	.0311	1022.6	9365.	4.305
13.	.0291	1013.6	7257.	3.952
14.	.0274	1004.1	5720.	3.650
15.	.0261	994.0	4598.	3.387
16.	.0249	983.7	3735.	3.158
17.	.0238	975.0	3066.	2.950
18.	.0228	968.2	2534.	2.762
19.	.0218	963.5	2111.	2.591
20.	.0211	958.8	1797.	2.442

C.3 Telemetry Measurements

The launch time for Vehicle 3 was 1517:00 EST. The onset of the first-stage acceleration, as indicated by the longitudinal accelerometer, was at 1517:00.35 EST. A maximum acceleration of 41.9 g's was reached at T+3.4 seconds. The vehicle deceleration reached 8.7 g's maximum before second-stage ignition.

The second stage was ignited at T+4.55 seconds, and a maximum acceleration of 102 g's occurred at T+6.05 seconds. The vehicle deceleration reached 33.2 g's maximum at T+6.8 seconds. Figure C.3.1 shows the longitudinal acceleration history for the first 60 seconds of the test.

Payload separation occurred at T+57 seconds. The baroswitch which initiates the recovery-system deployment began to close at T+123.73 seconds, pilot-parachute deployment began at T+144.59 seconds, and the main parachute was deployed at T+154.95 seconds. Loss of the telemetry signal occurred at T+293.75 seconds, 1521:54.1 EST.

[redacted]

[redacted]

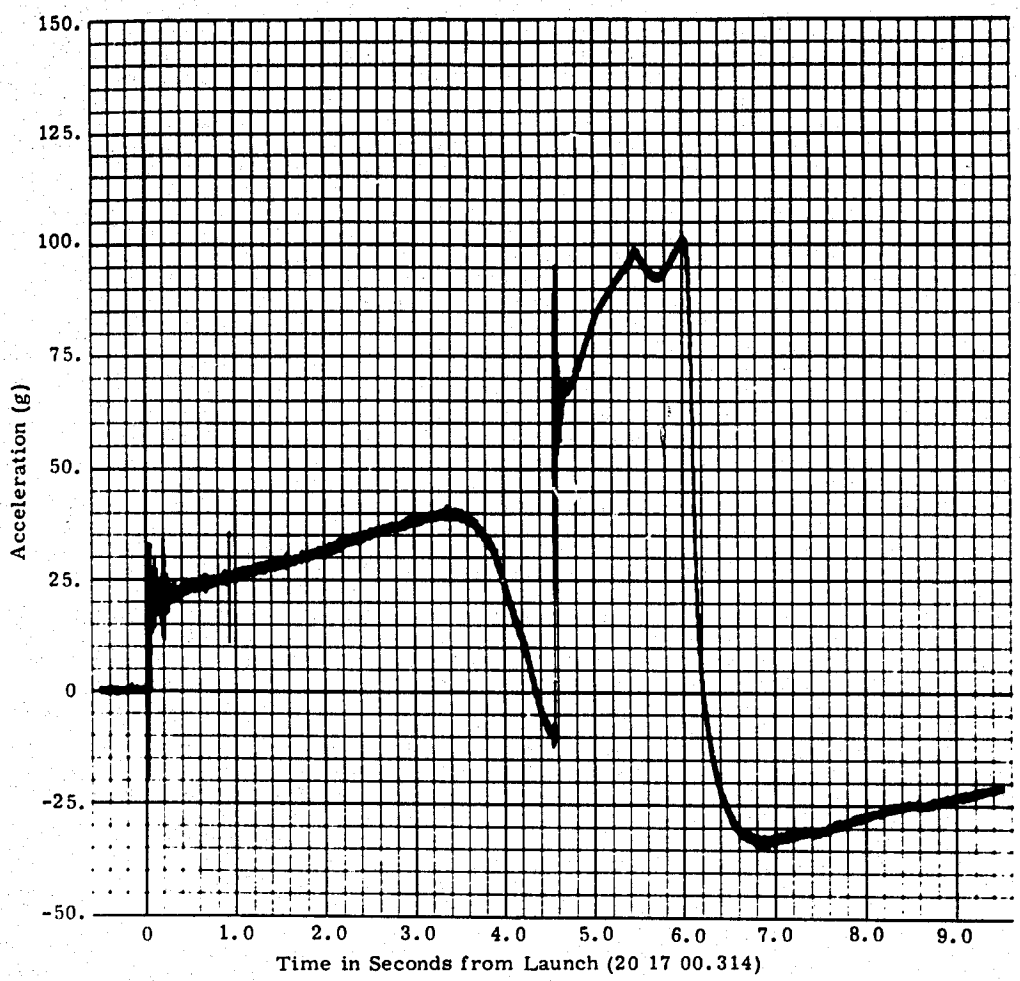

Figure C.3.1a Longitudinal Acceleration Versus Time, Vehicle 3

The thermal resistor element located on the aluminum substructure of the Recruit stabilizing flare indicated a maximum temperature of 163°C (325°F) before it became electrically shorted at T+19.11 seconds. The thermal resistors located in the telemetry transmitter, the substructure of the recovery section, and the umbilical connector wall of the payload indicated temperature increases of less than 14°C (25°F) during the test.

The recession-gage (TC564) output signal shifted from 1.25 volts to 1.8 volts at launch and then decreased to zero volts at T+1.65 seconds; after remaining at zero volts until T+2.3 seconds, it then returned to 1.8 volts by T+2.75 seconds. It again returned to zero volts at second-stage ignition and remained there until after second-stage burnout. At T+6.8 seconds it began to slowly increase and by T+8.0 seconds had stabilized around 3.15 volts. At T+11.0 seconds it exhibited a step increase to 3.5 volts. Subsequent recession measurements at the stagnation point of the recovered nosetip suggest that the step increase in signal at T+11.0 seconds was the loss of ^{182}Ta source number 3. Figure C.3.2 shows the TC564 telemetered output.

[redacted]

[redacted]

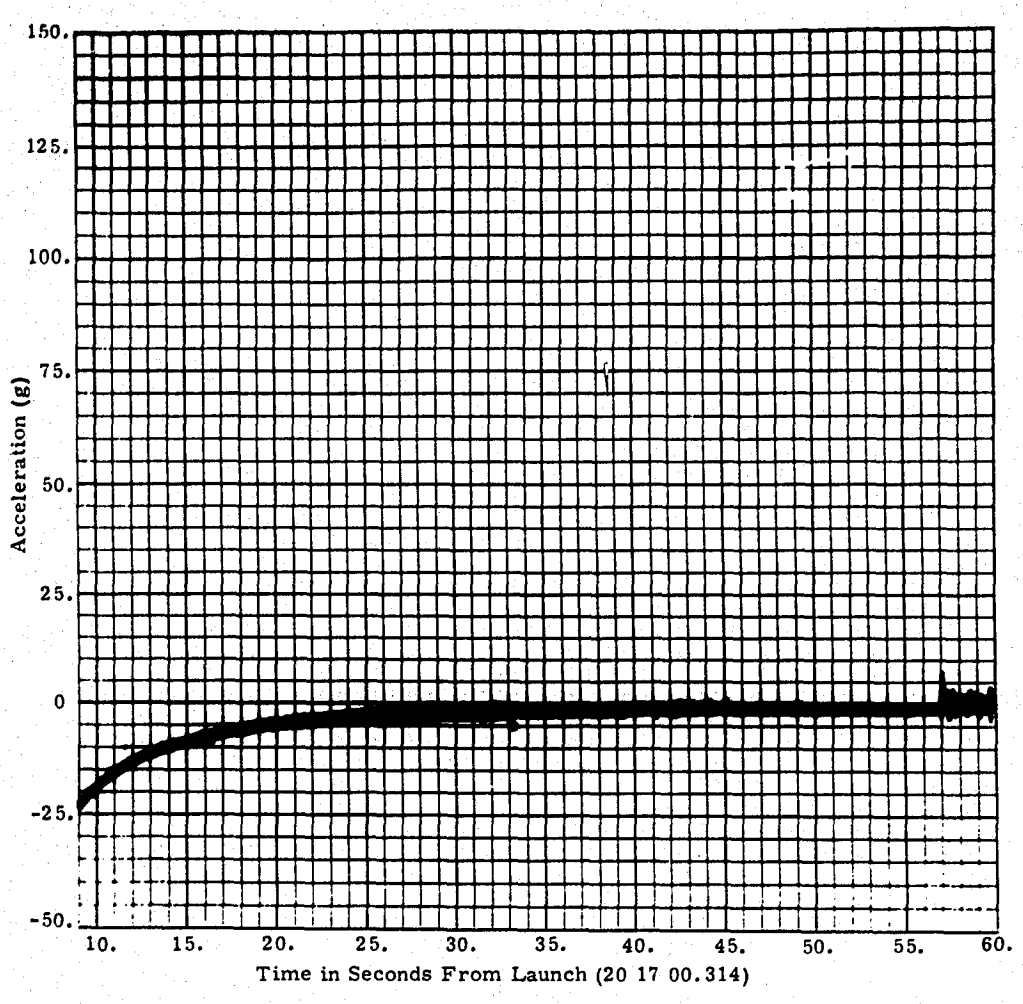

Figure C.3.1b Longitudinal Acceleration Versus Time, Vehicle 3

The telemetry RF signal transmitted from the vehicle payload was received at the NASA ground station with adequate strength throughout the test. Figure C.3.3 exhibits the first 50 seconds of the received signal strength history. All functions of the payload instrumentation and telemetry package were performed satisfactorily and on time, with the exception of the TC564 recession sensor as previously described in Section 3.4.

[redacted]

[redacted]

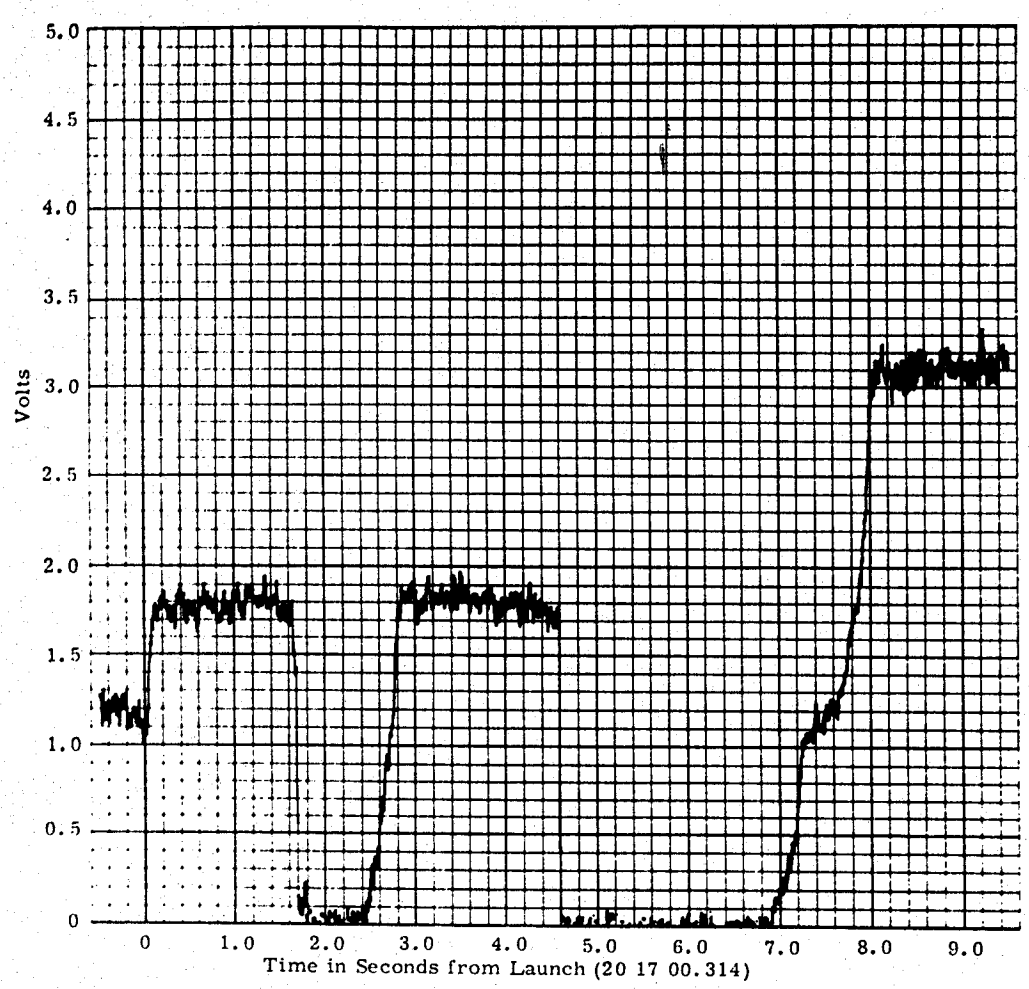

Figure C.3.2a Stagnation Point Recession Versus Time, Vehicle 3

[redacted]

[redacted]

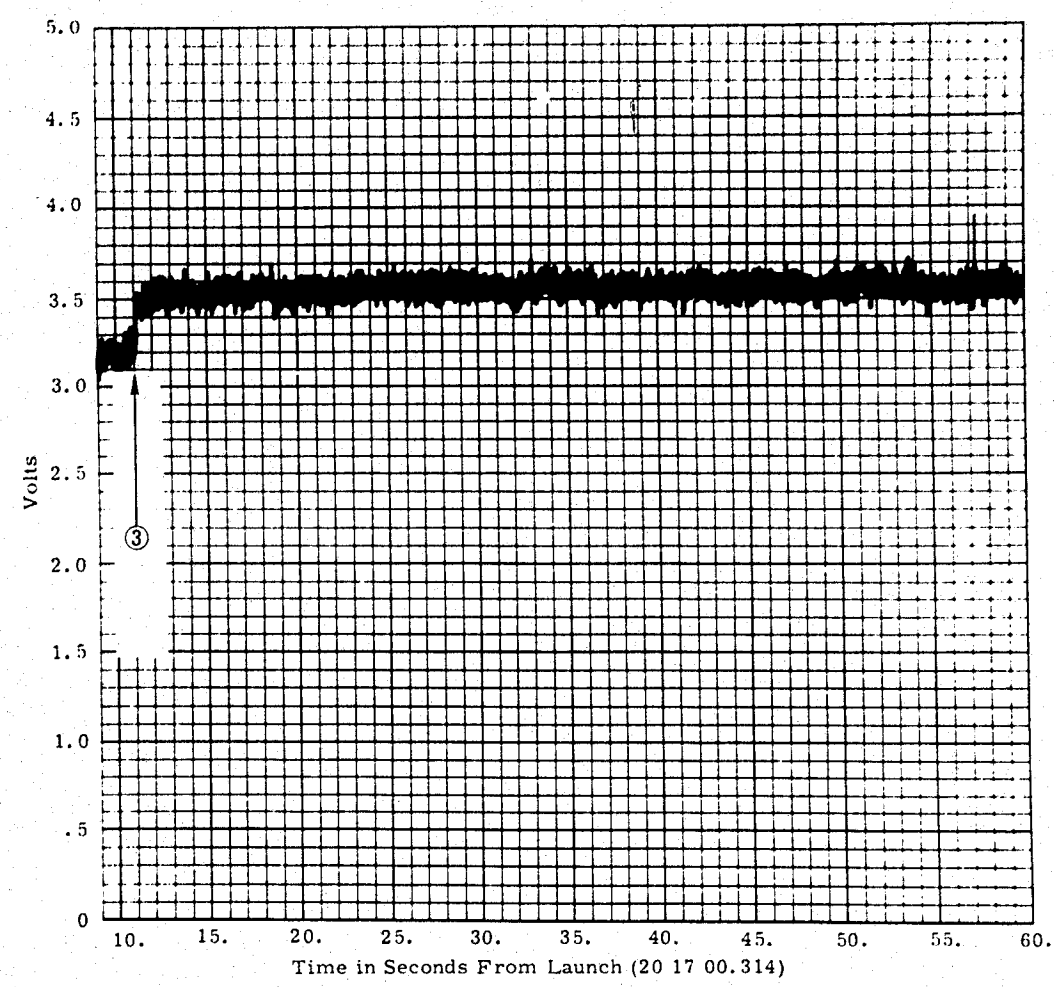

Figure C.3.2b Stagnation Point Recession Versus Time, Vehicle 3

[redacted]

[redacted]

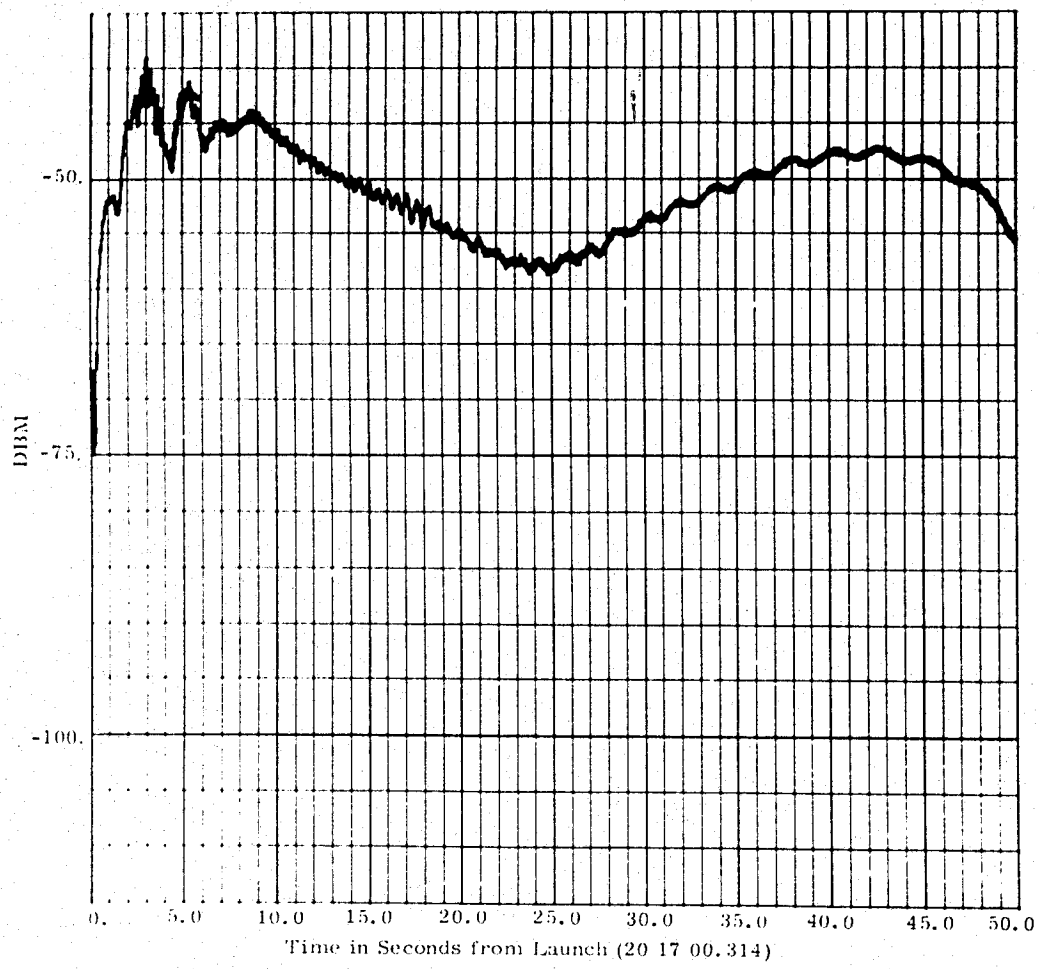

Figure C.3.3 Telemetry Signal Strength Versus Time, Vehicle 3

[redacted]

[redacted]

APPENDIX D

EROSION DATA, VEHICLE 4

[redacted]

[redacted]

[redacted]

(Intentionally left blank)

[redacted]

APPENDIX D

EROSION DATA, VEHICLE 4

D.1 Meteorological Data, Vehicle 4

Synoptic Weather Situation

A surface low pressure system - which the day before had been forecast to be in a position south of Cape Hatteras - was, by 0700, farther north and more intense than had been expected. Rain began falling at Wallops at 0730, at which time the forecast was for occasional rain during the day as the Hatteras low moved northeastward. Figure D.1.1 shows the surface synoptic weather charts for 0700, 1000, and 1300 EST. Notice the large rain area extending northward about 500 km (300 miles) and westward about 900 km (500 miles) from the off-shore low, with Wallops being just north of the northern edge at 0700.

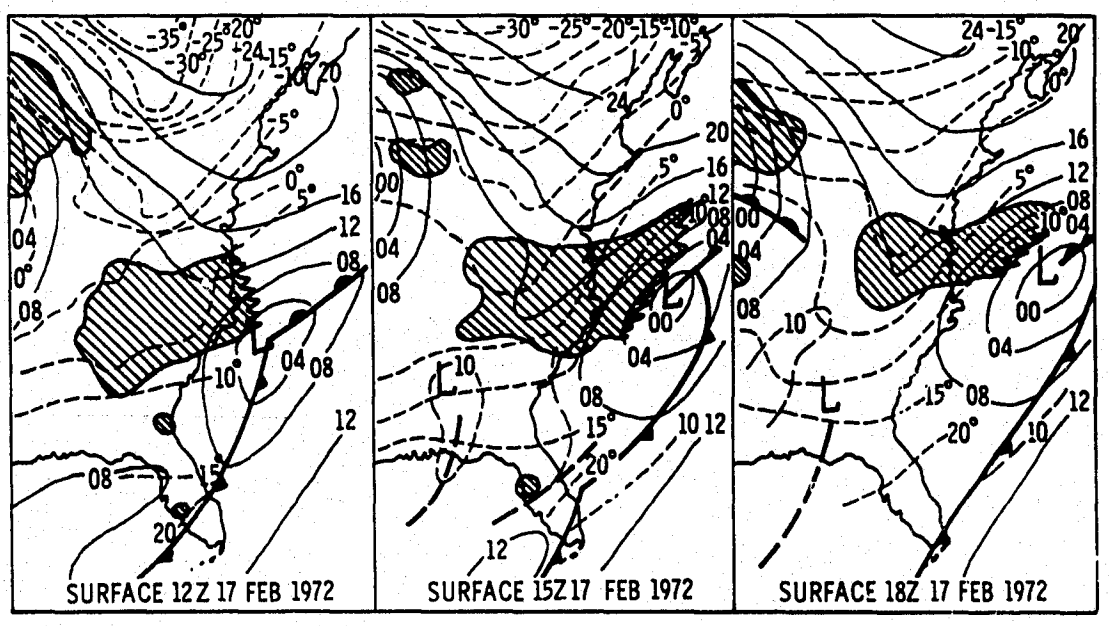

Figure D.1.1 Three Hourly Surface Weather Charts, February 17.

Analysis

At about 0815, the continuous rain started, lasting until almost 2000. The rate reached 2.7 mm/hr at 0840 and remained close to this value for several hours. Figure D.1.2 shows the 5-minute average rain rates derived from the modified weighing rain gages. Figure D.1.3 shows the rate for the 1-hour period 0930-1030, including shot time, derived from the tipping-bucket gage located at the radar site. This device gives an indication for every 0.25 mm of rain collected, or a resolution of 1/2 to 1 minute, depending on the rate. As can be seen from both these figures, the rate was pleasingly constant until about 0955, when a rise to 4 followed by drop to 2.2 mm/hr occurred within 2 minutes, followed by a ragged rise in about 7 minutes to a value in excess of 7 mm/hr. This peak had declined to 3 mm/hr when the shot was fired at 1012. The rate dropped to 2.5 at 1013, spiked to 4.5 at 1015, and then dropped to 2 mm/hr over the next 5 minutes. These small-scale variations, typical of detailed rain data, emphasize the convective cell structure of all precipitation situations, even the seemingly stratified storm systems.

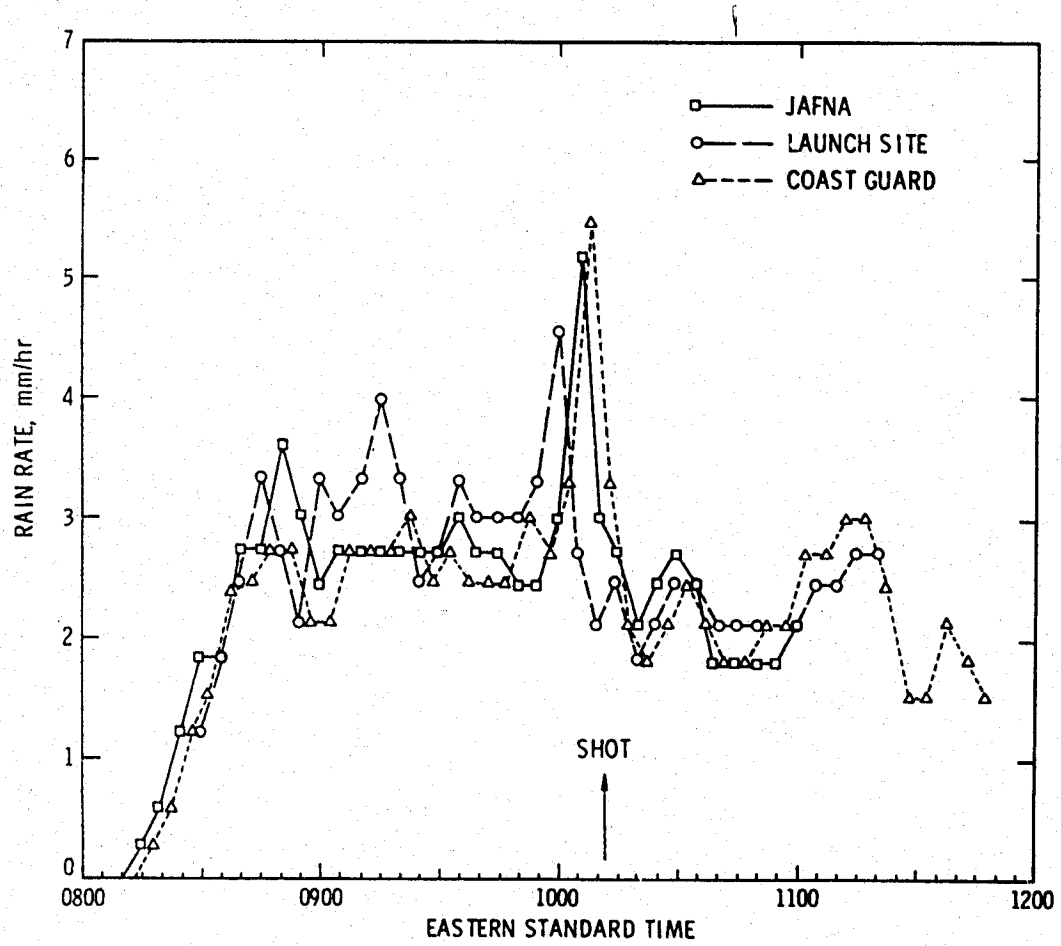

Figure D.1.2 Rain Rate Versus Time, Weighing Gage, February 17

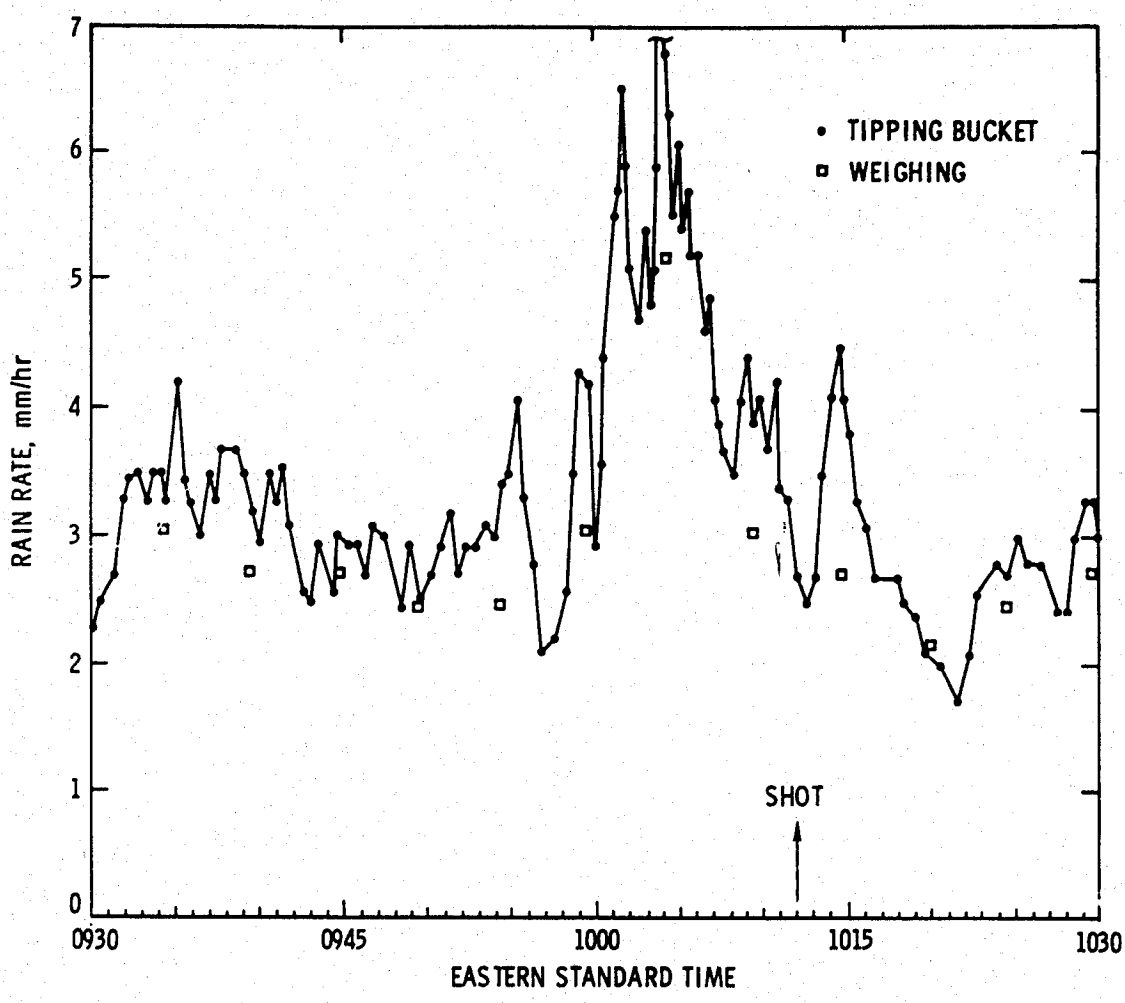

Figure D.1.3 Rain Rate Versus Time, Tipping Bucket Gage, February 17

The temperature, dew-point and winds-aloft profiles are shown in Figure D.1.4 as measured by a rawinsonde released at 1040, 28 minutes after shot time. The complex temperature structure shown from the surface to 2000 m (6500 ft) is an interesting feature which has complicated the analysis of liquid-water content. The radar data suggest two bright bands (melt layers), one from 180 (600 ft) to 420 m (1400 ft) and the other from 1150 m (3800 ft) to 1600 m (5200 ft). The lower one fits in well within the 0°C reading at 420 m (1400 ft) shown in Figure D.1.4. In order for the upper one to exist, however, an error must be assumed in the sonde temperature readings near 1500 m (4900 ft) altitude. Such an error is understandable, since the sonde was released in the rain. Any moisture that may have collected on the temperature element could have frozen in the 1000-m (3300-ft) layer near the ground and then never completely melted in the warm air, perhaps above freezing, at 1500 m (4900 ft). This would tend to give an artificially low reading until freezing was reached again at about 16[illegible] m ([illegible]200 ft). Unfortunately, the temperatures reported by [illegible] sampling aircraft are suspect because they were about 3 to 5°C (5 to 9°F) higher than the sonde values at all levels.

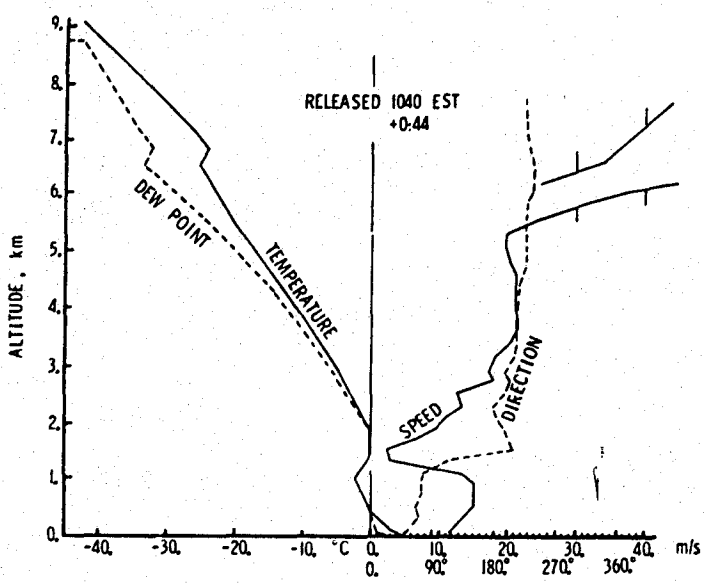

Figure D.1.4 Rawinsonde Observation, February 17

The radar reflectivity profile along the rocket trajectory at shot time is shown in Figure D.1.5. The tape-recorded values and those measured from the RHI photographs by AFCRL are in much closer agreement than for the Vehicle 3 test. Regions of disagreement are below 1 km (3.3 kft), 4.8 km (15.7 kft), and above 6.6 km (21.6 kft). Some of the misfit around the 6-km (20.0-kft) region could be improved by simply applying a -500 to -800 m (-1600 to -2600 ft) correction to the AFCRL profile. The profile of equivalent liquid-water content as derived from radar reflectivity, aircraft sampling and sounding considerations is shown in Figure D.1.7.

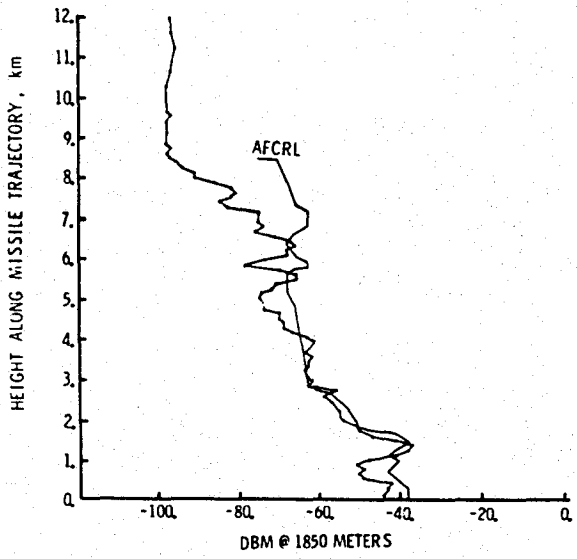

Figure D.1.5 Radar Reflected Power Profile, February 17

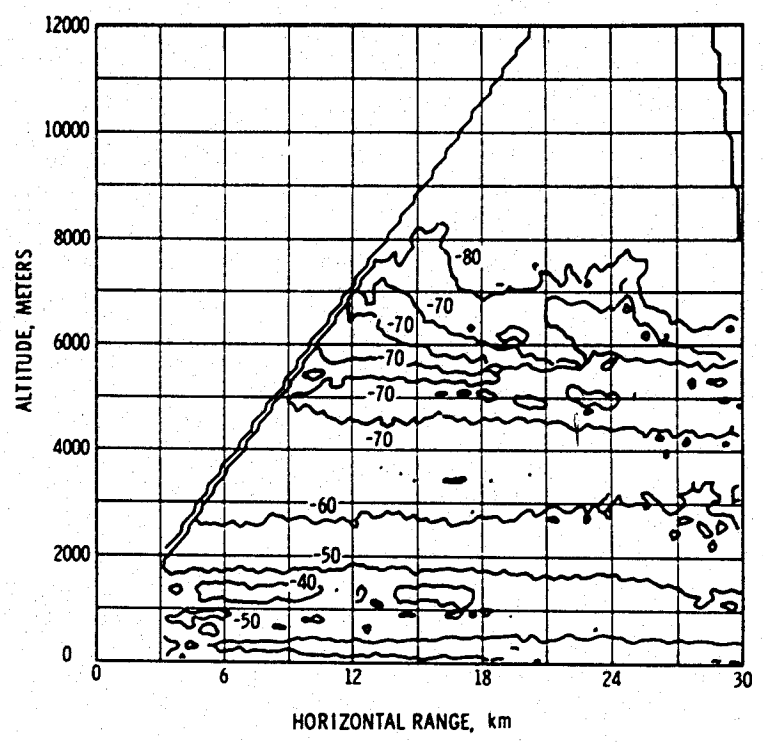

Figure D.1.6 Contoured Reflected Power RHI, February 17

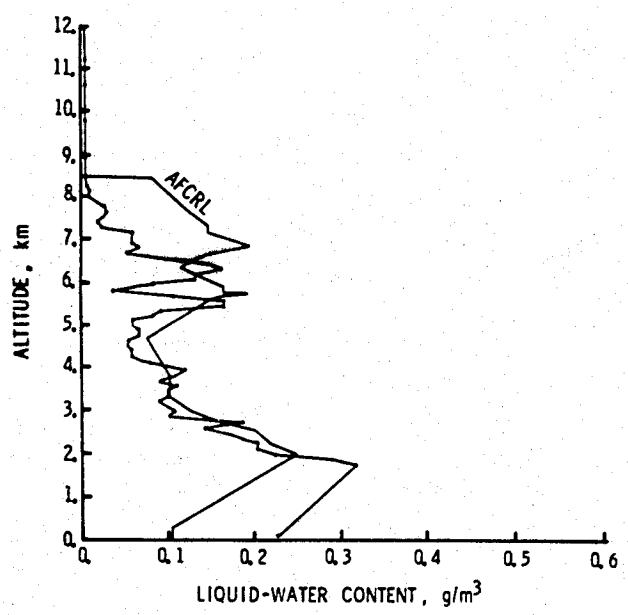

Figure D.1.7 Equivalent Liquid-Water Content Profile, February 17

[redacted]

D.2 Vehicle 4 Performance

The performance of the Terrier-Recruit booster system was nearly nominal during the Vehicle 4 flight test. Radar tracking data (FPQ-6, C-band radar) and the on-board accelerometer data were combined to determine accurate velocity and space position histories. The maximum velocity achieved was 2.585 km/s (8482 fps) at 6.73 seconds and at an altitude of 3.057 km (10029 ft) msl. This velocity and altitude were respectively 2 percent below and 2.7 m (9 ft) above those calculated before launch. The flight-path angle at maximum velocity was 0.7 degrees below nominal. The launcher was set for an elevation angle of 35 degrees with no elevation correction for wind, and an azimuth of 153 degrees, with +7 degrees of correction.

The event history for this flight is presented in Table C.2.1. The measured velocity-time, altitude-time, and altitude-velocity plots are presented, along with the preflight nominals, in Figures D.2.1, D.2.2, and D.2.3, respectively. The elevation and plan tracking data are presented with the preflight nominals in Figures D.2.4 and D.2.5. Table D.2.1 contains a tabulation of the trajectory data for Vehicle 4.

The 2-percent reduction of the measured maximum velocity from the nominal apparently was caused chiefly by the performance degradation of the Terrier motor resulting from the fact that its temperature at launch was 3.9°C (39°F), or about 20°C (36°F) below its specified nominal temperature range. Extended Terrier burn time is also an effect that has been previously observed when the motor propellant was colder than the nominal. (The Recruit's propellant is less susceptible to temperature variations.)

About half of the decrease in the vehicle flight path angle at maximum velocity was caused by variations in the wind velocity between the time of launcher set and launch. The motor temperature effect caused the remainder.

[redacted]

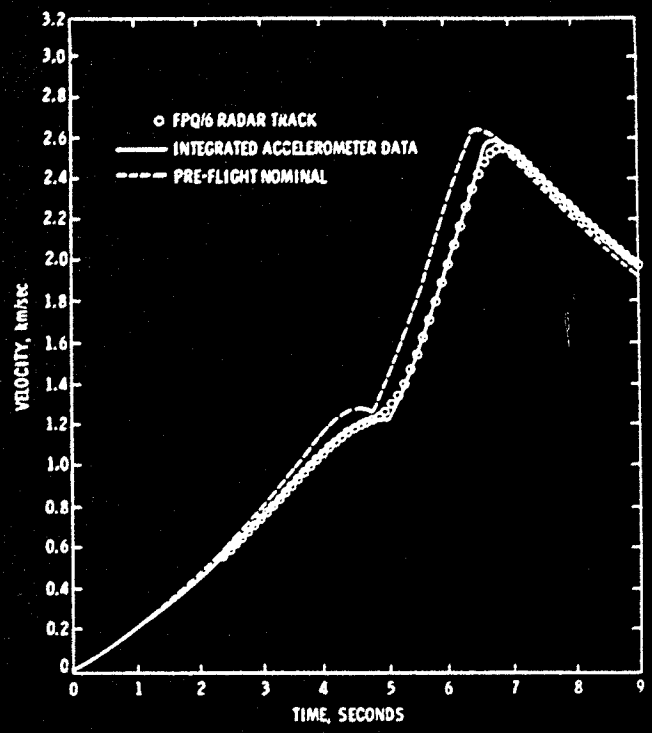

Figure D.2.1a Velocity Versus Time, Vehicle 4

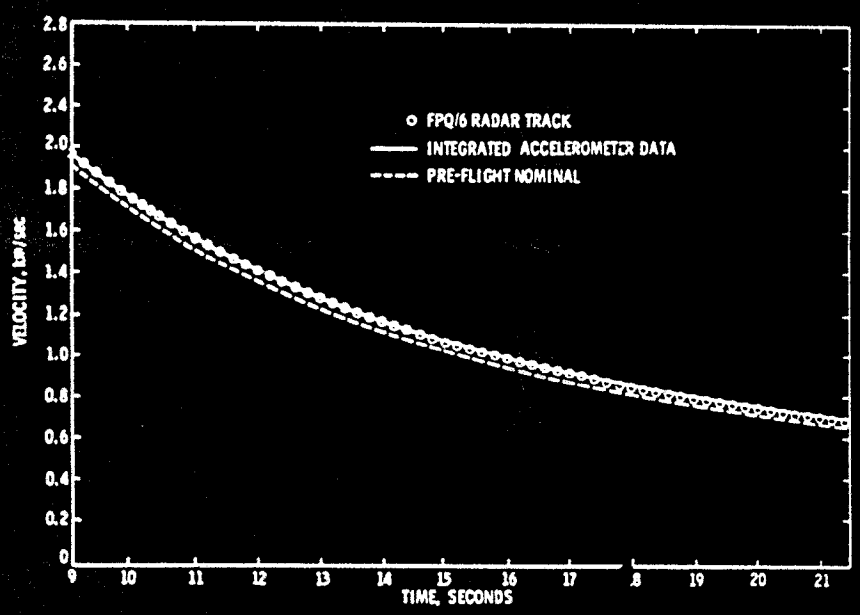

Figure D.2.1b Velocity Versus Time, Vehicle 4

[redacted]

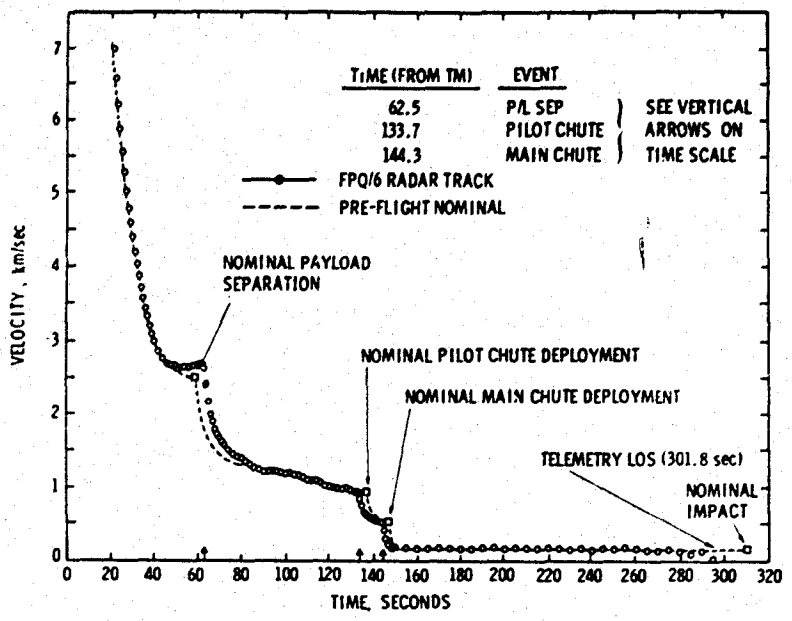

Figure D.2.1c Velocity Versus Time, Vehicle 4

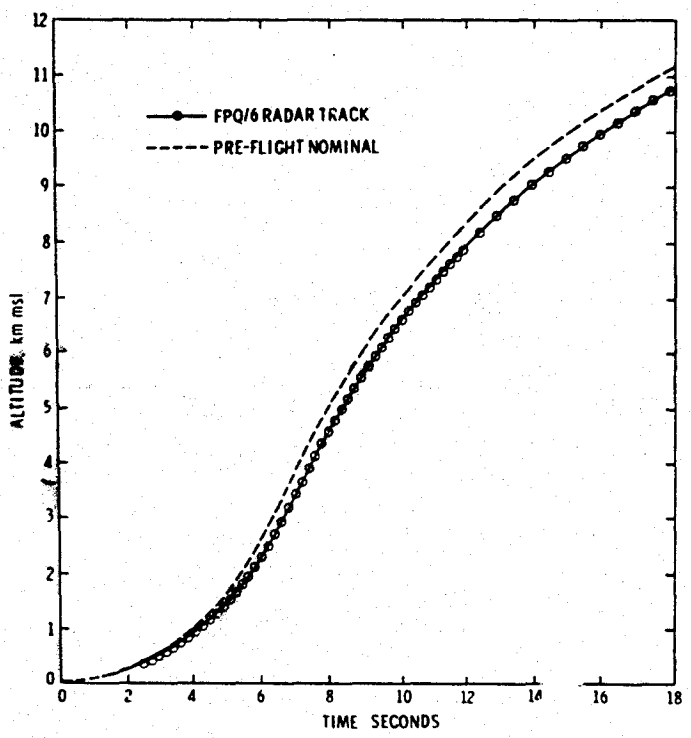

Figure D.2.2 Altitude Versus Time, Vehicle 4

[redacted] UNCLASSIFIED

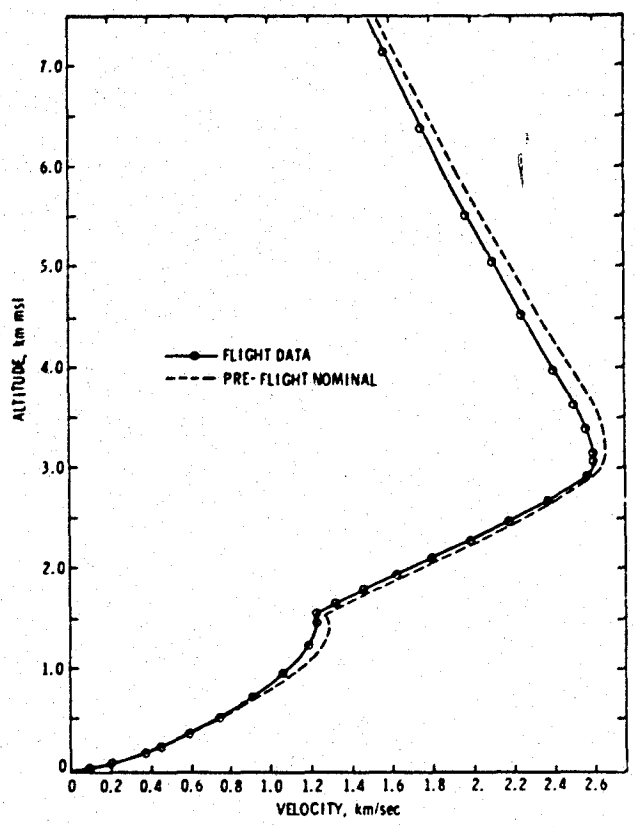

Figure D.2.3 Altitude-Velocity Profile, Vehicle 4

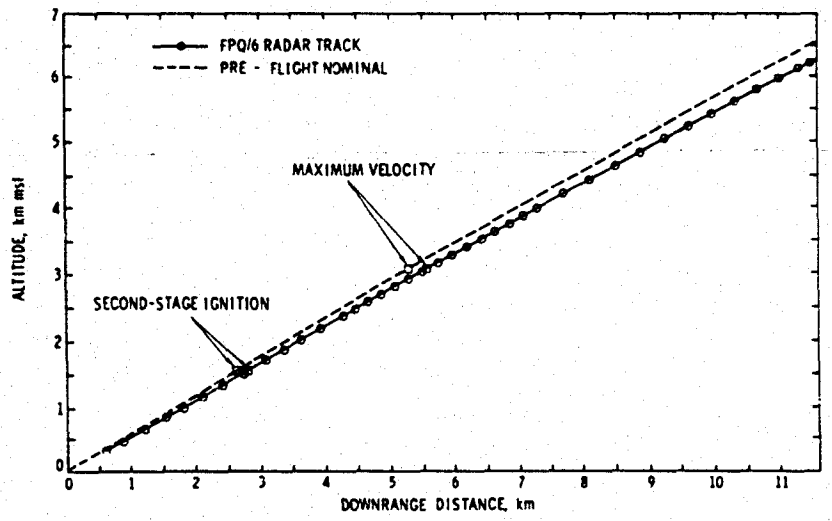

Figure D.2.4a Altitude-Distance Profile, Vehicle 4

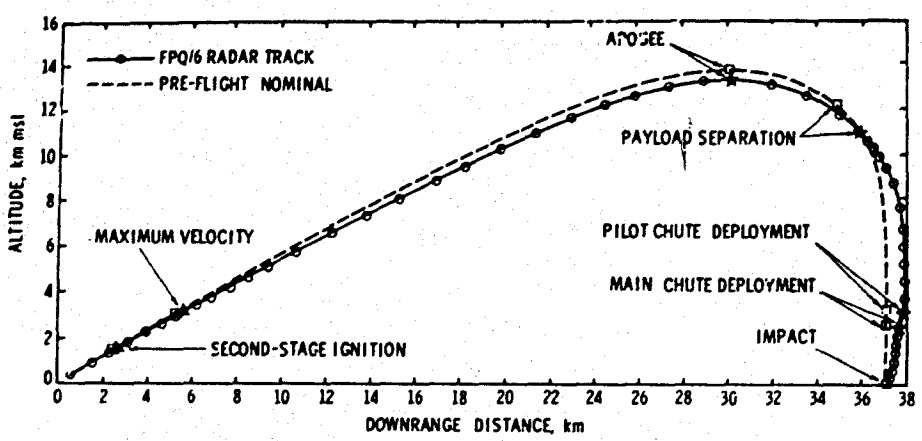

Figure D.2.4b Altitude-Distance Profile, Vehicle 4

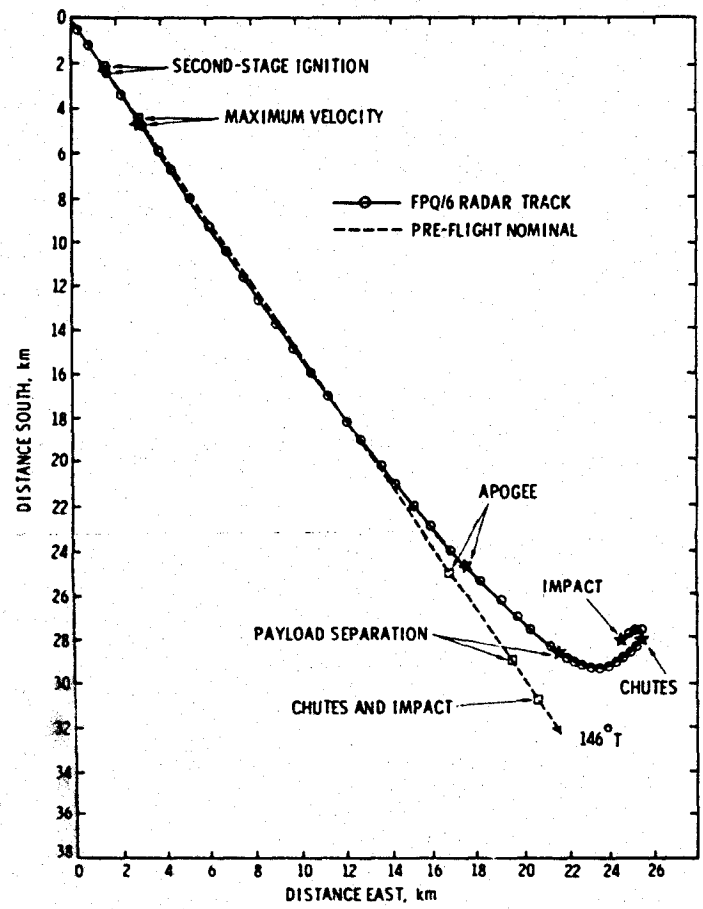

Figure D.2.5 Plan Position Track, Vehicle 4

[redacted]

TABLE D.2.1a

Vehicle 4 Trajectory Data

Time From T_o (sec)	Altitude (ft msl)	Velocity (ft/sec)	Ground Range (ft)
0.5	60	300	120
1.0	220	656	430
1.7	560	1,217	1,050
2.0	760	1,474	1,410
2.5	1,169	1,935	2,118
3.0	1,704	2,442	3,063
3.5	2,362	2,963	4,234
4.0	3,141	3,482	5,632
4.5	4,028	3,895	7,237
4.9	4,797	4,007	8,618
5.045	5,089	3,993	9,139
5.2	5,412	4,312	9,717
5.4	5,855	4,772	10,519
5.6	6,336	5,304	11,404
5.8	6,865	5,887	12,388
6.0	7,447	6,506	13,476
6.2	8,085	7,127	14,673
6.4	8,780	7,742	15,978
6.6	9,525	8,375	17,376
6.73	10,029	8,482	18,319
6.8	10,303	8,470	18,831
7.0	11,095	8,346	20,300
7.2	11,881	8,160	21,748
7.5	13,030	7,850	23,854
8.0	14,835	7,346	27,186
8.5	16,506	6,877	30,315
9.0	18,060	6,450	33,253
10.0	20,867	5,716	38,612
11.0	23,348	5,118	43,392
12.0	25,561	4,614	47,692
13.0	27,534	4,184	51,586
14.0	29,308	3,820	55,145
15.0	30,906	3,510	58,408
16.0	32,349	3,240	61,415
17.0	33,664	2,999	64,210
18.0	34,855	2,792	66,806
21.0	37,830	2,303	73,662

[redacted]

TABLE D.2.1b

Vehicle 4 Trajectory Data

Time From T_o (sec)	Air Density ($lbsm/ft^3$)	Sound Speed (ft/sec)	Dynamic Pressure ($lbsf/ft^2$)	Mach Number
.5	.07893	1094.	110.	.274
1.	.07863	1092.	528.	.601
1.7	.07798	1090.	1795.	1.117
2.	.07760	1089.	2620.	1.354
2.5	.07672	1087.	4464.	1.780
3.	.07539	1085.	6986.	2.251
3.5	.07379	1084.	10067.	2.733
4.	.07185	1082.	13537.	3.218
4.5	.06929	1084.	16336.	5.593
4.90	.06715	1085.	16755.	3.693
5.045	.06636	1085.	16442.	3.680
5.2	.06558	1085.	18949.	3.974
5.4	.06451	1085.	22829.	4.398
5.6	.06340	1085.	27717.	4.888
5.8	.06221	1084.	33504.	5.431
6.0	.06092	1082.	40072.	6.013
6.2	.05954	1080.	46997.	6.599
6.4	.05814	1078.	54154	7.182
6.6	.05673	1077.	61835.	7.769
6.73	.05581	1075.	62396.	7.890
6.8	.05531	1074.	61663.	7.886
7.0	.05388	1071.	58322.	7.792
7.2	.05248	1068.	54303.	7.640
7.5	.05052	1065.	48379.	7.371
8.	.04758	1059.	39900.	6.937
8.5	.04504	1053.	33101.	6.531
8.	.04280	1046.	27670.	6.166
10.	.03874	1038.	19670.	5.507
11.	.03513	1035.	14300.	4.945
12.	.03264	1025.	10798.	4.501
13.	.03063	1014.	8333.	4.126
14.	.02896	1002.	6567.	3.812
15.	.02751	992	5267.	3.538
16.	.02630	981.	4290.	3.303
17.	.02518	972.	3519.	3.085
18.	.02411	966.	2921.	2.890
21.	.02087	967.	1720.	2.382

[redacted]

[redacted]

D.3 Telemetry Measurements

Vehicle 4 was launched from the HAD launcher, Pad 0, at 1012:00 EST. The onset of first-stage acceleration began at 1012:00.3 EST. The first stage Terrier produced a maximum acceleration of 32.4 g's at T+3.4 seconds. The vehicle deceleration reached a maximum of 6.5 g's before second-stage ignition. The second-stage Recruit experienced a maximum acceleration of 101.8 g's at T+6.55 and a maximum deceleration of 32.5 g's at T+7.45 seconds. Figure D.3.1 shows the longitudinal acceleration history for the first 60 seconds of the flight.

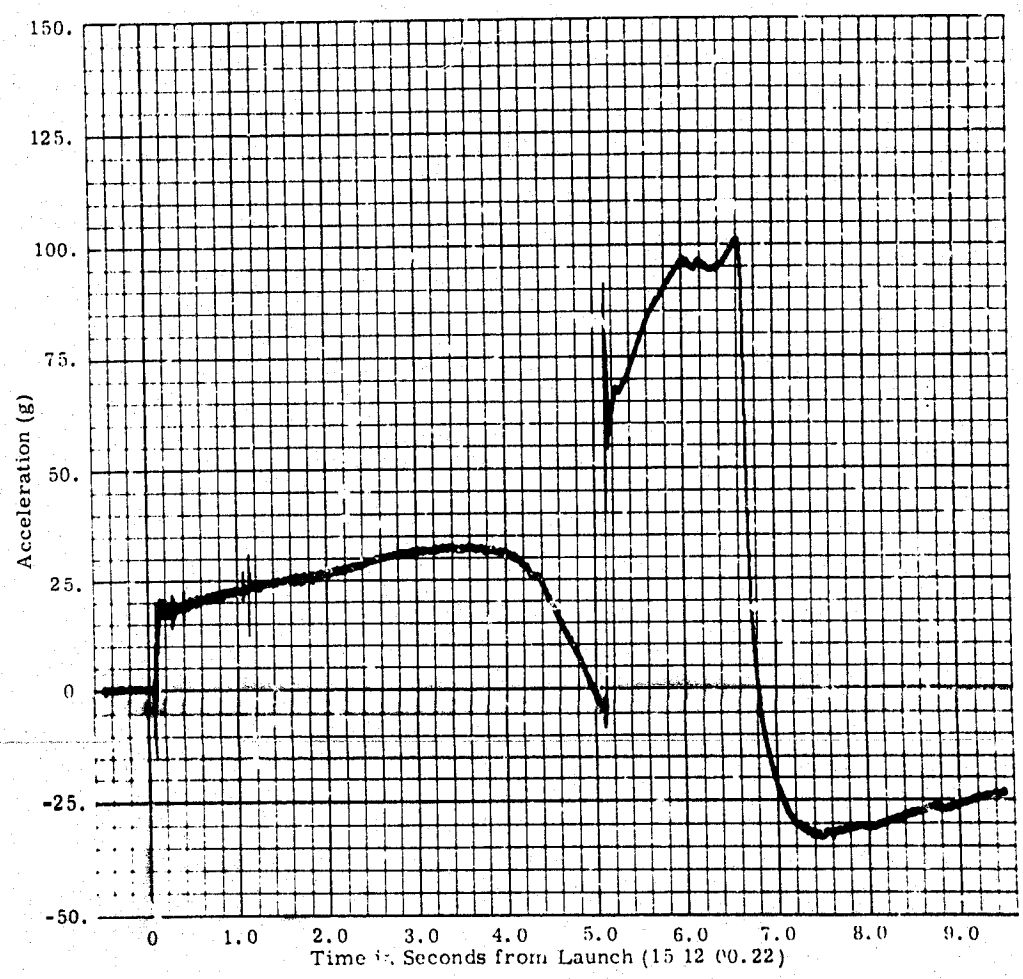

Figure D.3.1a Longitudinal Acceleration Versus Time, Vehicle 4

Vehicle roll commenced at approximately T+0.3 seconds, by T+3.8 seconds had exceeded 400 degrees/second, and remained in excess of 400 degrees/second until parachute deployment was initiated. The vehicle pitch and yaw rates appeared normal throughout the flight.

[redacted]

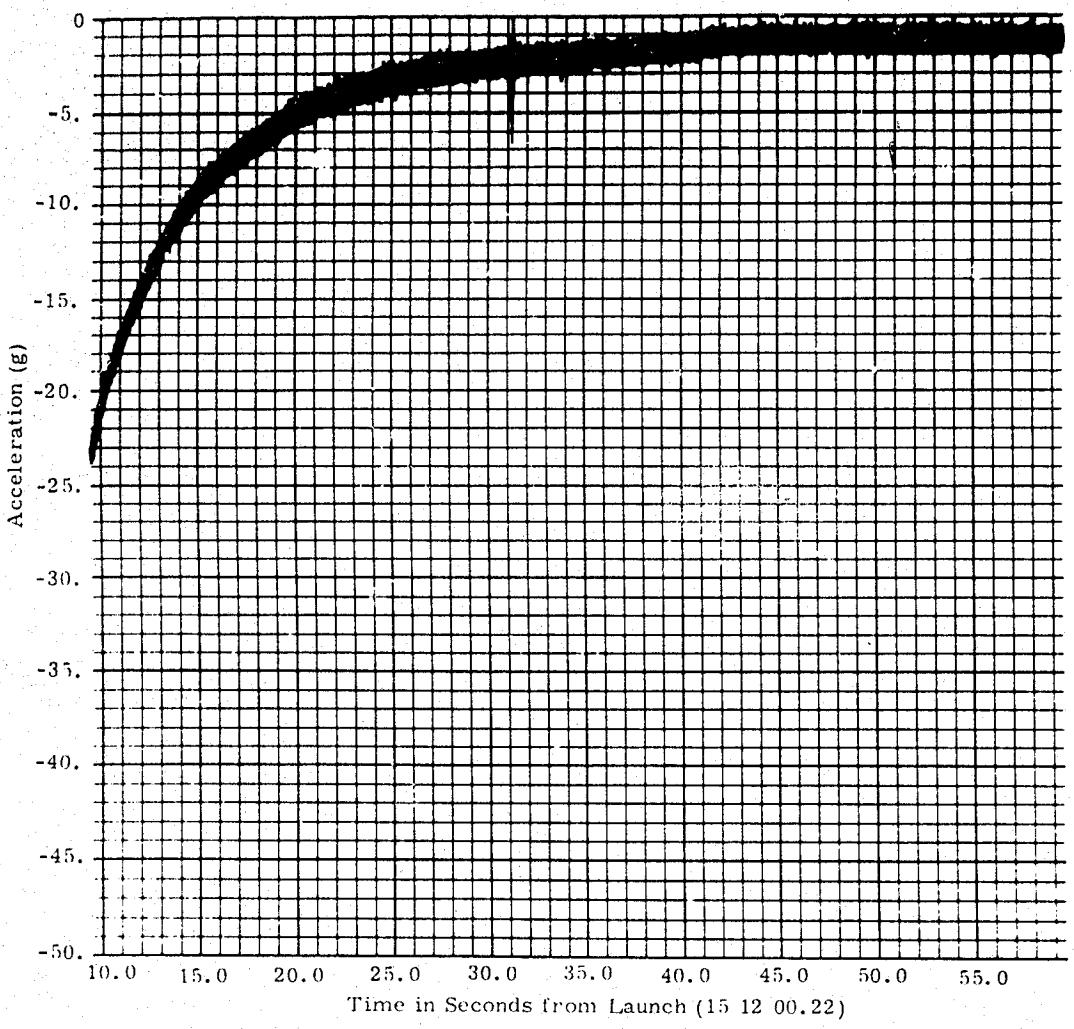

Figure D.3.1b Longitudinal Acceleration Versus Time, Vehicle 4

Payload separation occurred at T+62.5 seconds. The baroswitch which initiates parachute deployment began to close at T±110.3 seconds. The pilot-parachute deployment occurred at T+133.7 seconds, the main-parachute deployment at T+144.25 seconds. Loss of the telemetry signal occurred at 1017:02.05 EST, T+301.75 seconds.

The temperature sensor located on the substructure of the Recruit stabilizing flare reached a maximum temperature of 66°C (151°F) before the sensor electrically shorted at T+16.2 seconds. Other temperature sensors located within the payload at the telemetry transmitter, on the substructure of the recovery section, and on the umbilical connector wall showed less than 15°C (27°F) increase during the test.

The TC564 recession sensor functioned normally during this test, indicating the loss of four ^{182}Ta sources between T+6.45 and T+10.21 seconds.

The telemetered recession data are shown in Figure D.3.2. The telemetry signal, as received at the NASA ground station, had adequate strength throughout the test and is shown in Figure D.3.3.

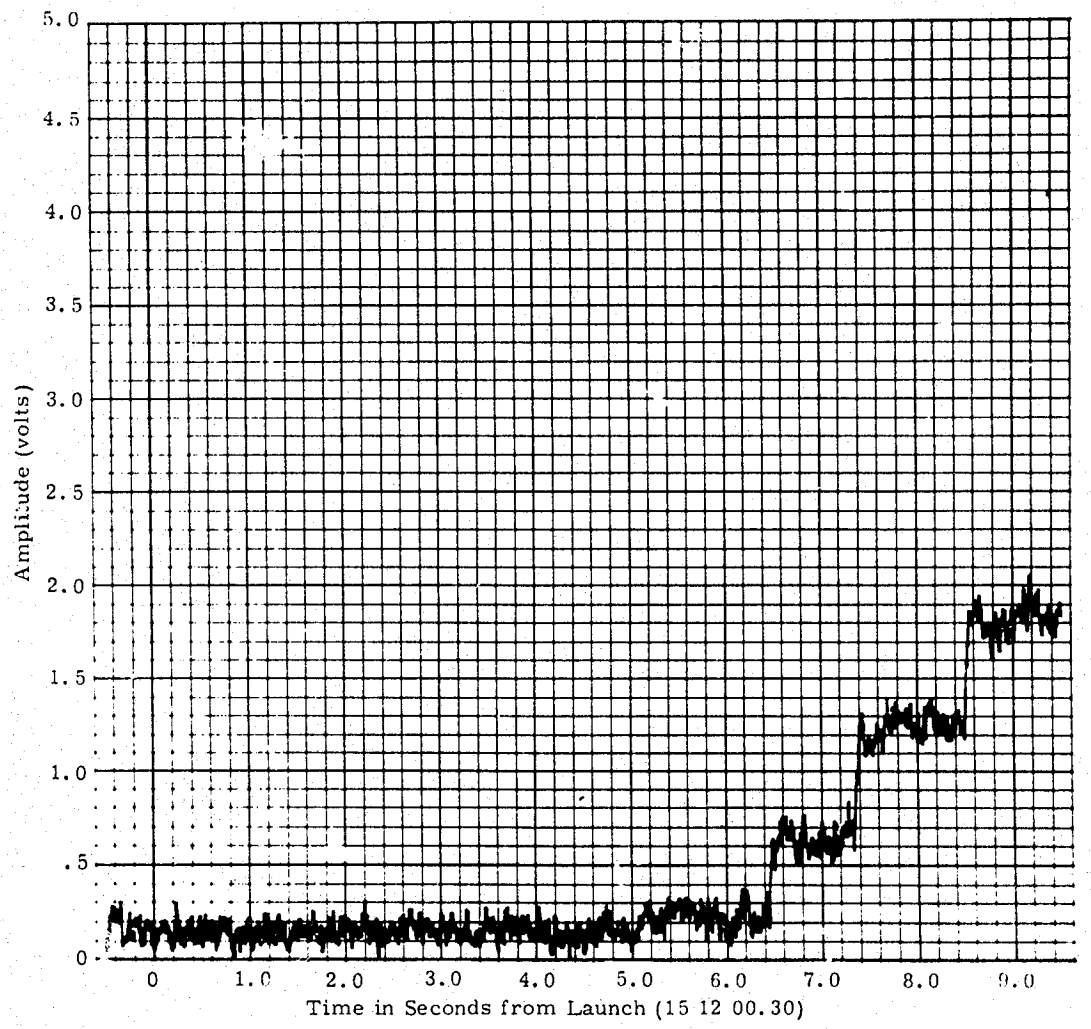

Figure D.3.2a Stagnation Point Recession Versus Time, Vehicle 4

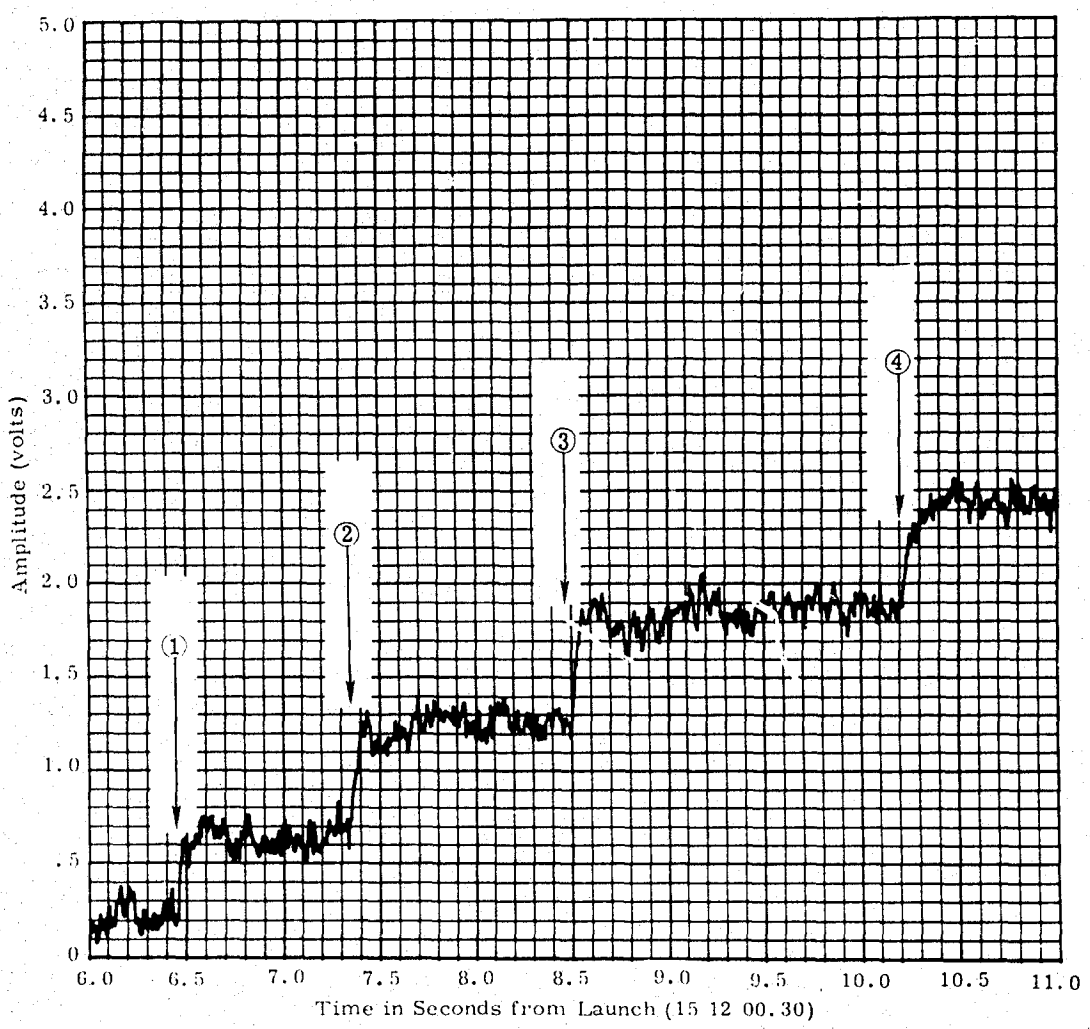

Figure D.3.2b Stagnation Point Recession Versus Time, Vehicle 4

[redacted]

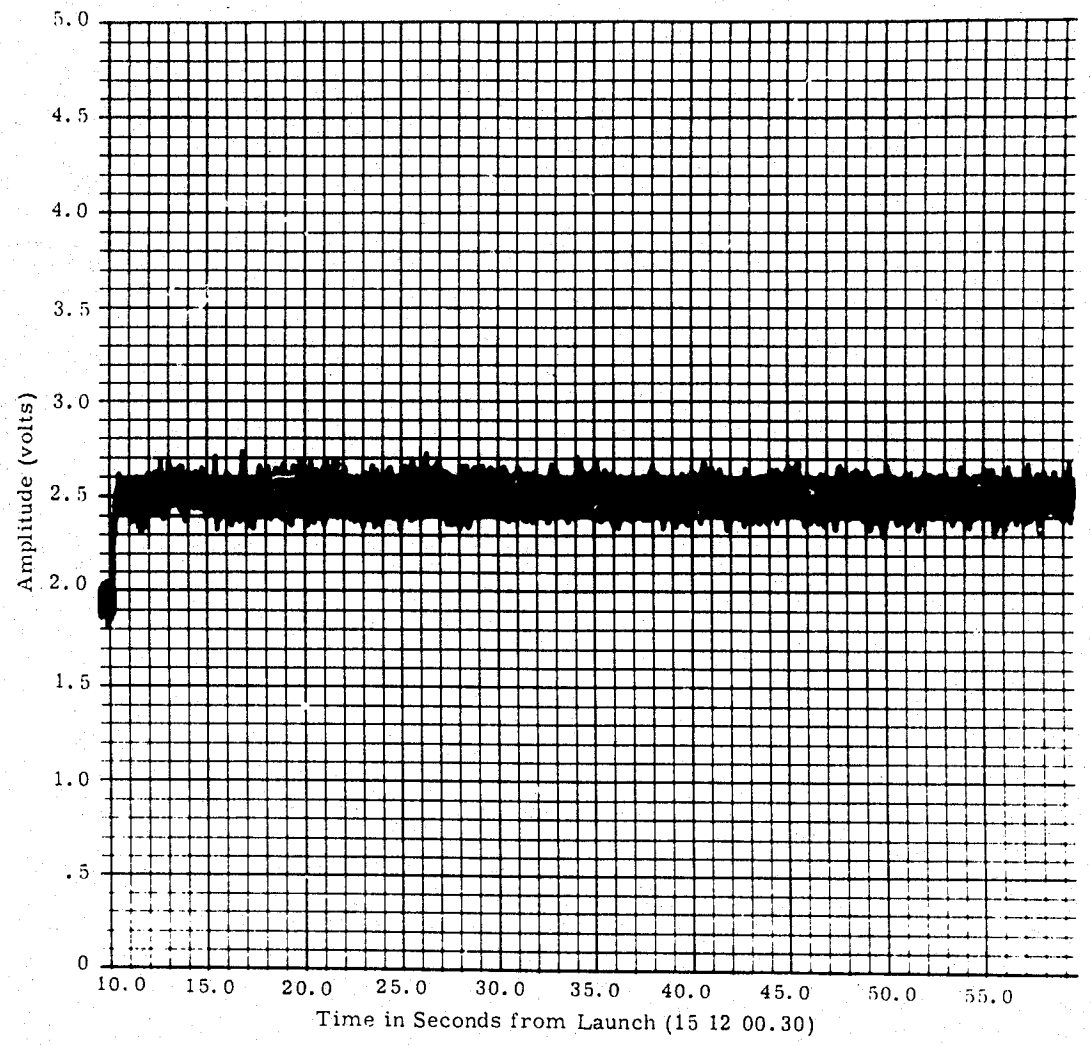

Figure D.3.2c Stagnation Point Recession Versus Time, Vehicle 4

[redacted]

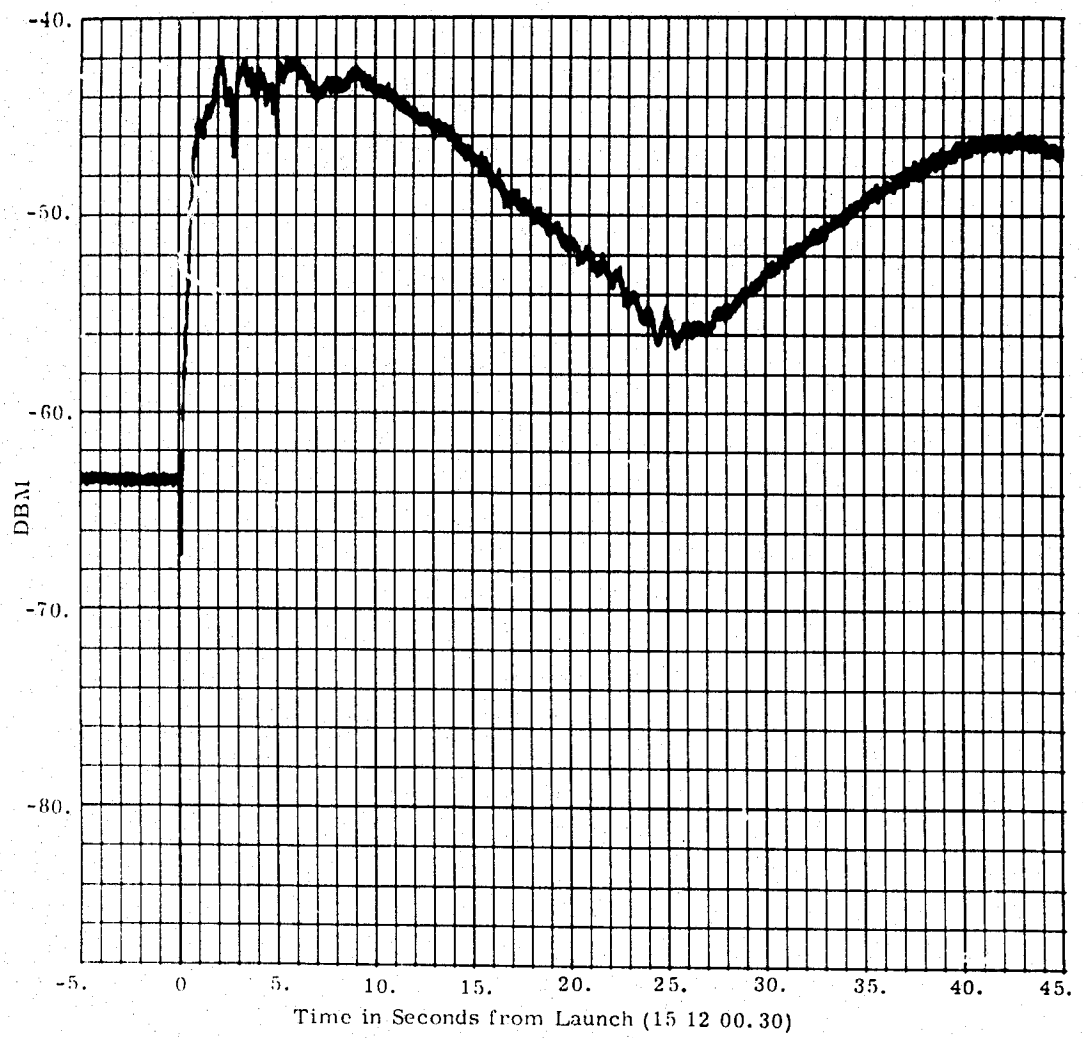

Figure D.3.3 Telemetry Signal Strength Versus Time, Vehicle 4

APPENDIX E

EROSION DATA, VEHICLE 5

(Intentionally left blank)

APPENDIX E

EROSION DATA, VEHICLE 5

E.1 Meteorological Data, Vehicle 5

Synoptic Weather Situation

At 0700 EST, a deep, dual-centered surface low-pressure region was located over lower Ontario, with an occluded front extending southeastward from Buffalo to Philadelphia. From this point the warm front extended east southeastward out to sea while the cold front extended southward and southwestward just east of the Appalachian Mountains (Figure E.1.1). The cold front was ahead of the surface position of the pressure trough by some 170 km (106 miles), and Wallops Island was about 150 km (93 miles) east of the advancing cold front. By 1000 the front had slowed its forward speed to about 5 m/sec (10 knots). This probably resulted from intensification of the associated upper low at the 500-mb level, which at 0700 was centered over Green Bay and by 1900 (next upper-air map time) was centered over Cleveland.

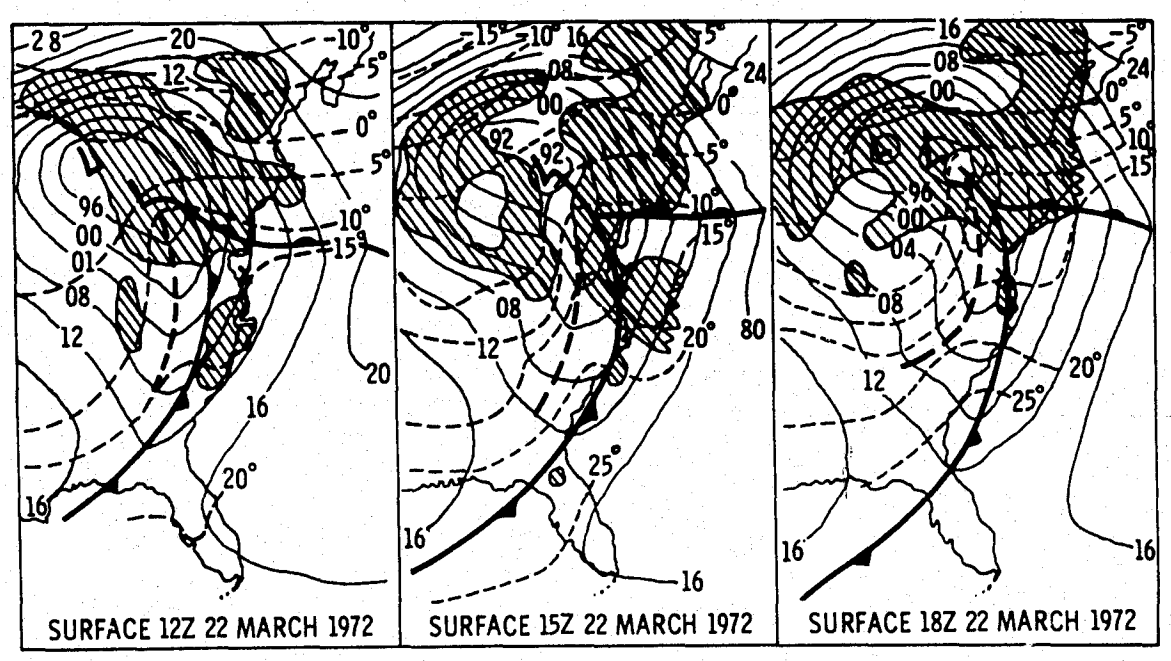

Figure E.1.1 Three Hourly Surface Weather Charts, March 22

Analysis

Light rain began at the Island weather station at 0835. At 0900 surface winds were from the south averaging around 13 m/sec (25 knots) with gusts to 20 m/sec (39 knots). Figure E.1.2 shows the rain-rate-versus-time data from the accelerated weighing gages at JAFNA and launch site (data for Coast Guard Station are available but are not shown in the figure). The earliest record, JAFNA, began at 0857 and shows a shower building to a 3.5-mm/hr rate at about 0905, dropping to 0.3 at 0920, reaching a second peak at 0930, and descending to zero by 0955. At 1000 both records show a third shower building which reached 1.2 to 1.5 mm/hr by 1020. By 1035 both records had dropped back to less than 0.5 and were holding fairly steady through 1043.

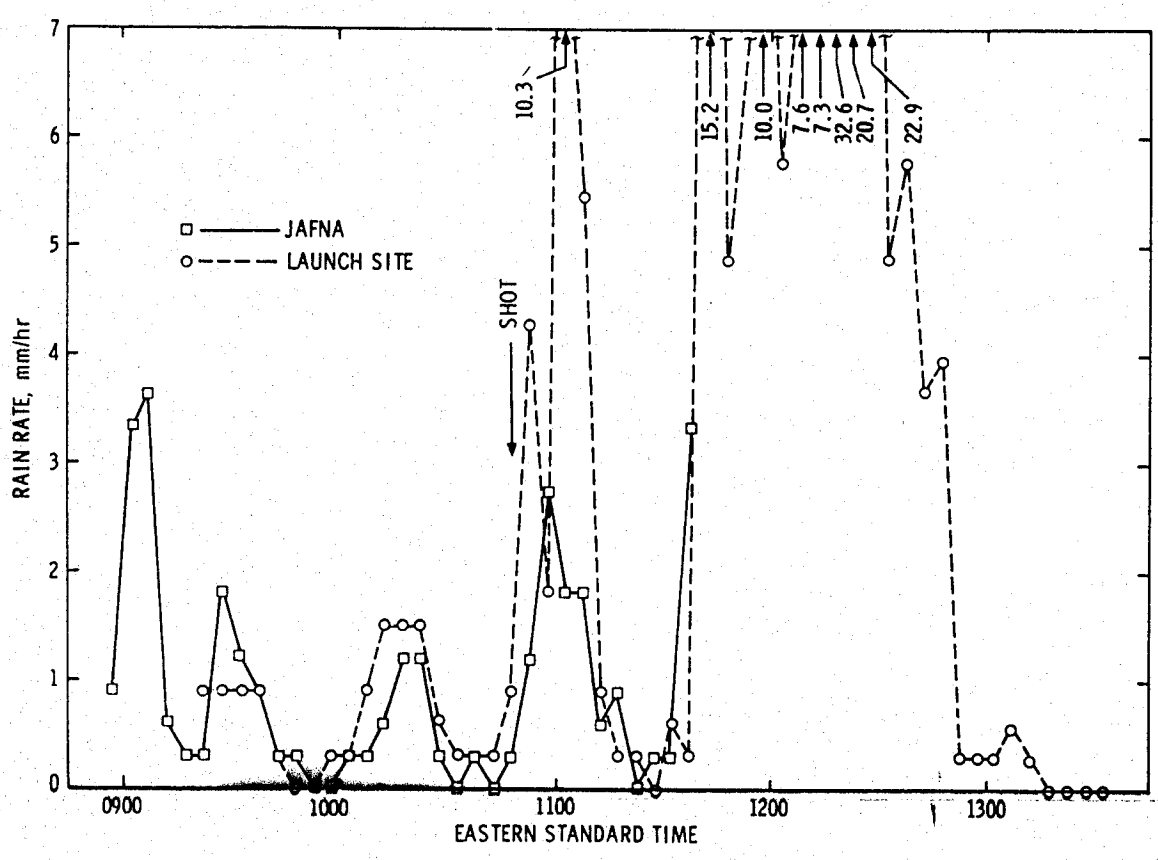

Figure E.1.2 Rain Rate Versus Time Weighing Gage, March 22

Figure E.1.3 is a plot of the high-resolution tipping-bucket gages for the same two locations. Notice that the desired light surface rain rate was maintained up to launch time, 1048. However, immediately after firing, the launch-site rate started an abrupt increase which peaked at 15.2 mm/hr at 4 minutes after launch. Apparently only the edge of this shower reached JAFNA, peaking 7 minutes after launch at 2.5 mm/hr. Both of these figures graphically indicate the shower type of activity predominant with this day's precipitation. The shower which interrupted the recovery helicopter's return flight is shown reaching "heavy" portions (> 7.5 mm/hr) at 1140, remaining

above this value nearly continuously until after 1230. This shower was associated with the frontal passage while the trough line, as noted by a windshift and thunderstorm (3 mm hail reported at Wallops Station), passed at 1440.

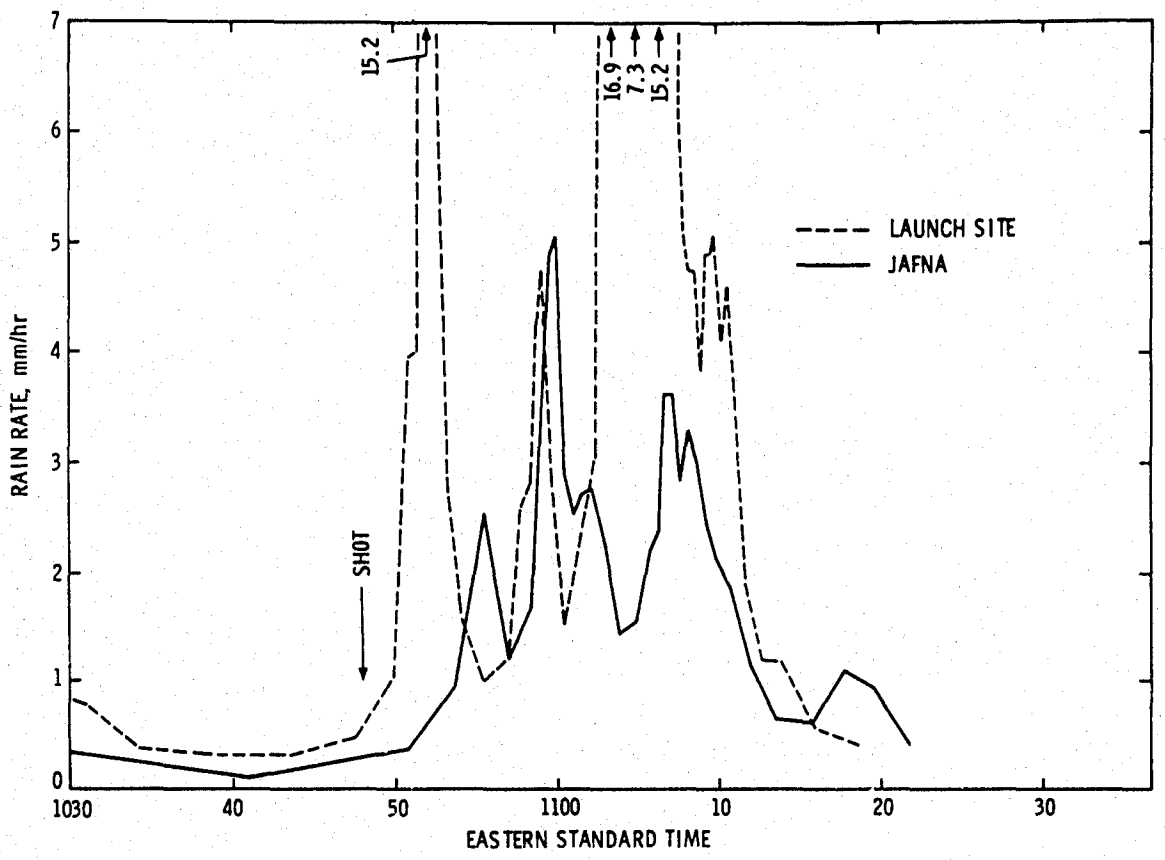

Figure E.1.3 Rain Rate Versus Time, Tipping Bucket Gages, March 22

The temperature, dew-point and winds-aloft profiles are shown in Figure E.1.4 as measured by a balloon-borne radiosonde released at 1113, or 25 minutes after launch. The altitude of 0°C (32°F) is shown at 2.2 km (7.2 kft), which agrees very well with the tabular tape-recorded output of radar reflectivity peak value at 2.22 km (7.28 kft).

The radar reflectivity profile is shown in Figure E.1.5. Here again the agreement between the two processing procedures (contoured RHI photographs and tape-recorded, computer-produced profiles) is quite satisfactory. The only disagreement appears in the altitude region above 8 km (26.0 kft), where the so-called background values from there to 10 km (33.0 kft) above the storm are some 20 db higher than those for 2/17 and 2/3. Contoured reflectivity is shown in Figure E.1.6.

The profile of equivalent liquid-water content as derived from the radar data is shown in Figure E.1.7.

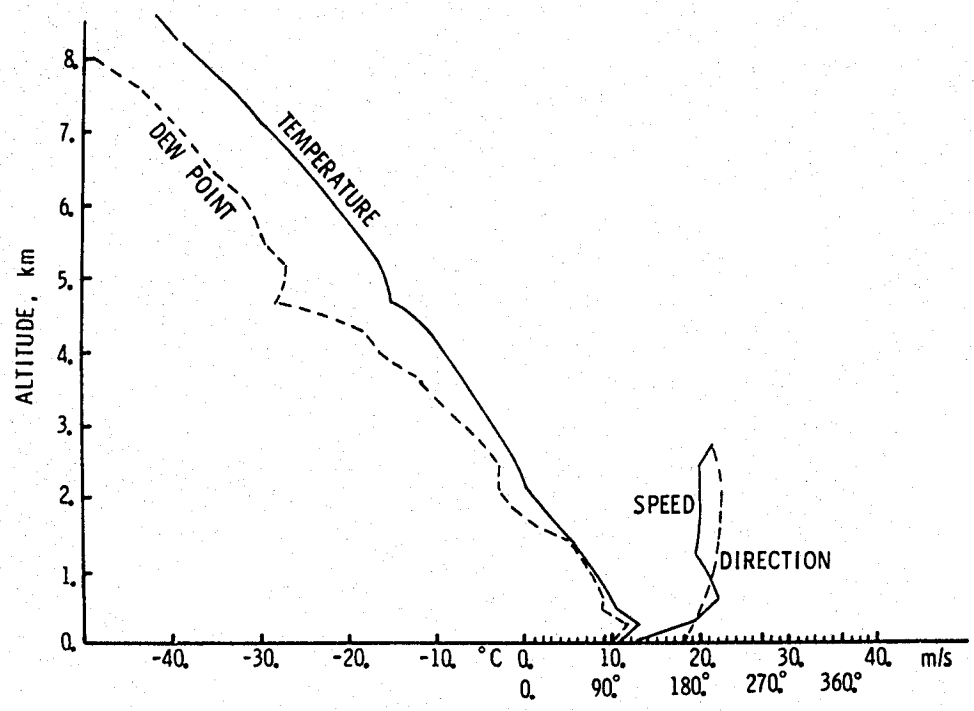

Figure E.1.4 Rawinsonde Observation, March 22

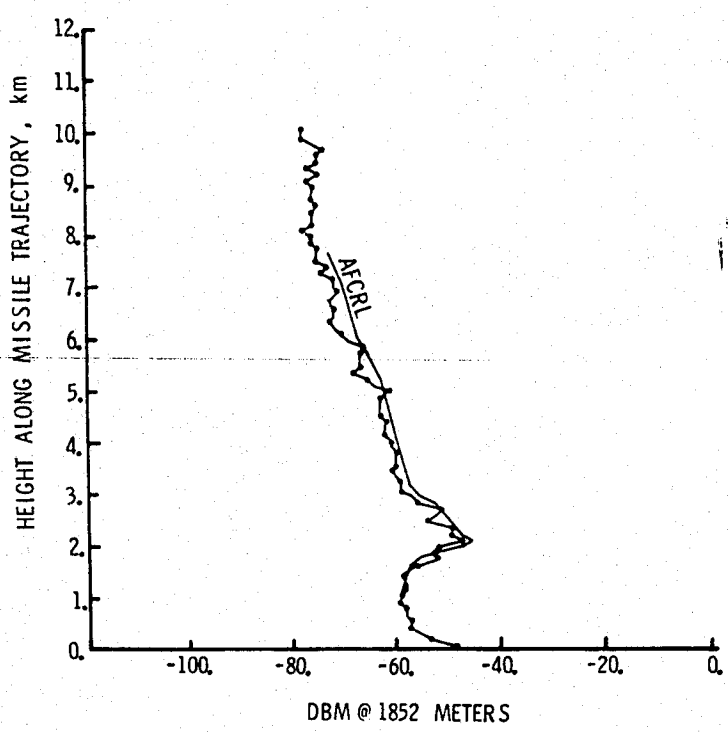

Figure E.1.5 Radar Reflected Power Profile, March 22

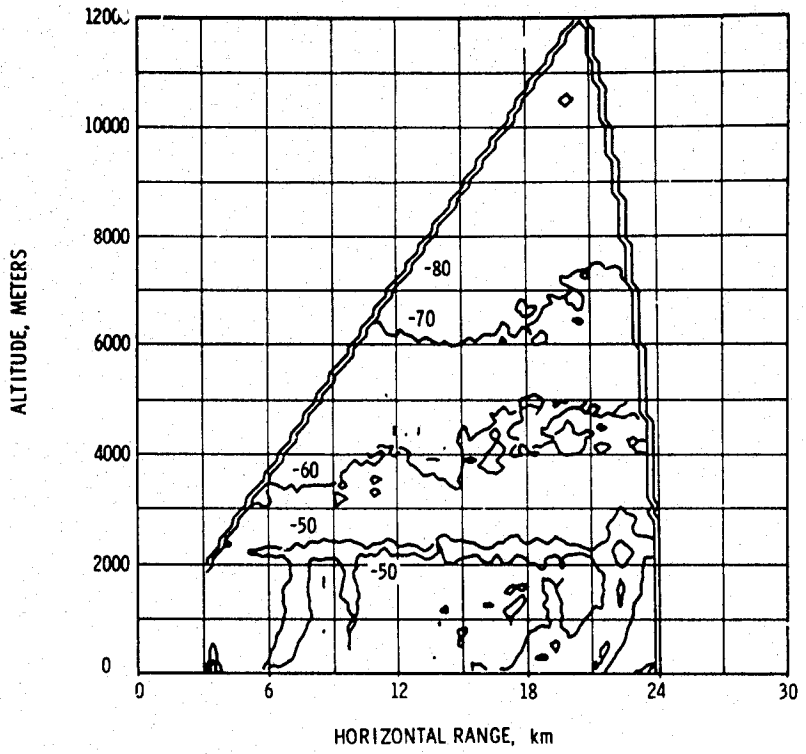

Figure E.1.6 Contoured Reflected Power, March 22

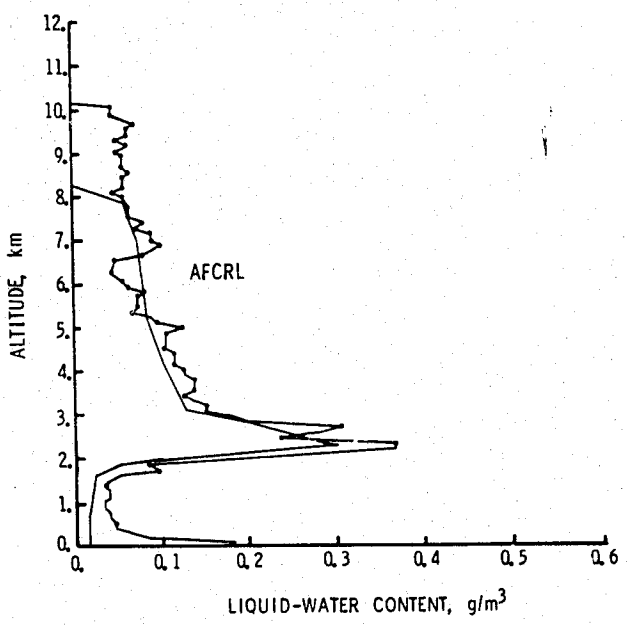

Figure E.1.7 Equivalent Liquid-Water Content Profile, March 22

E.2 Vehicle 5 Performance

The Terrier-Recruit booster-system performance during the flight test of Vehicle 5 was nearly nominal. Radar tracking data (FPQ-6, C-band radar) and the telemetered axial acceleration data were combined to determine accurate velocity and space position histories. The maximum velocity achieved was 2.570 km/sec (8431 fps) at 6.60 seconds and at an altitude of 3.129 km (10265 ft) msl. The maximum velocity was 2.5 percent below the calculated preflight nominal, and the altitude at maximum velocity was 74.7 m (245 ft) higher than the calculated value.

Figures E.2.1 and E.2.2 show the measured velocity-time and altitude-time histories, respectively, along with their calculated preflight nominals. Figure E.2.3 presents the measured and nominal plots of altitude versus velocity. Figures E.2.3 and E.2.5 exhibit the measured and nominal elevation and plan tracks, respectively. Table E.2.1 contains a tabulation of the measured trajectory data. Event history for the flight is included in Table C.2.1.

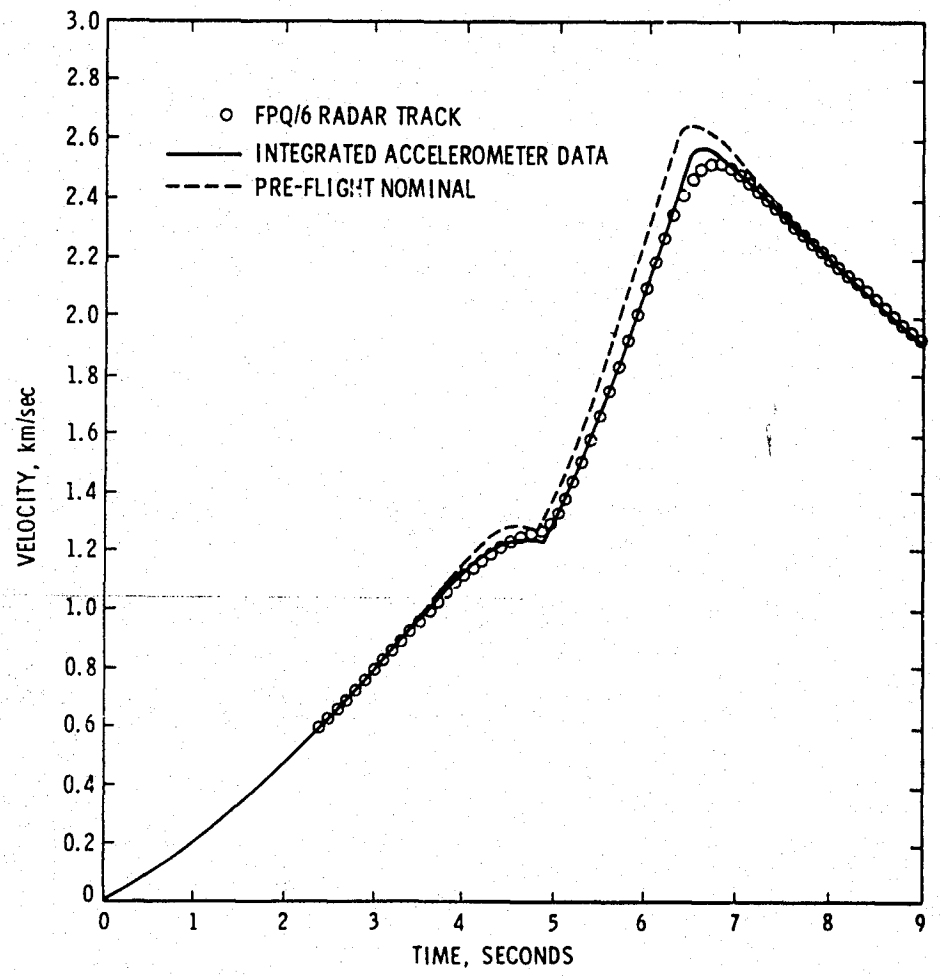

Figure E.2.1a Velocity Versus Time, Vehicle 5

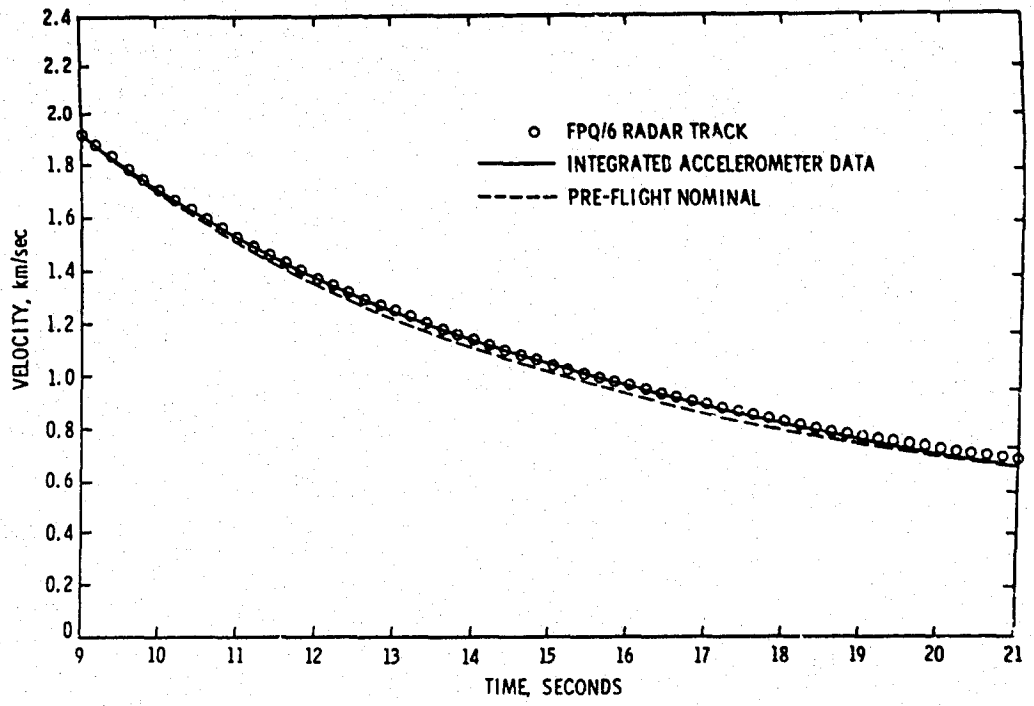

Figure E.2.1b Velocity Versus Time, Vehicle 5

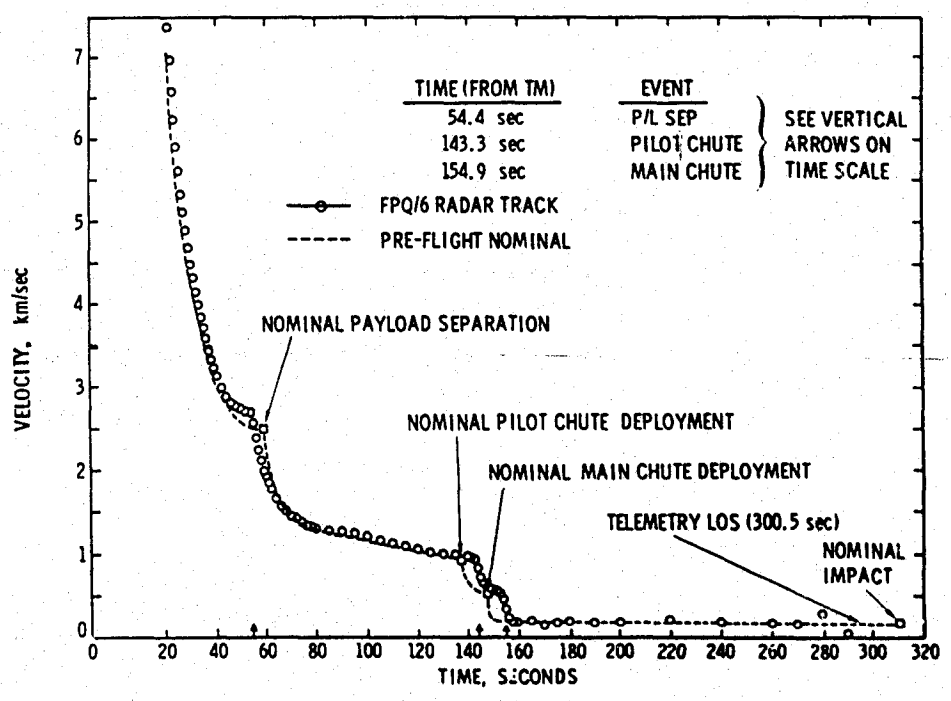

Figure E.2.1c Velocity Versus Time, Vehicle 5

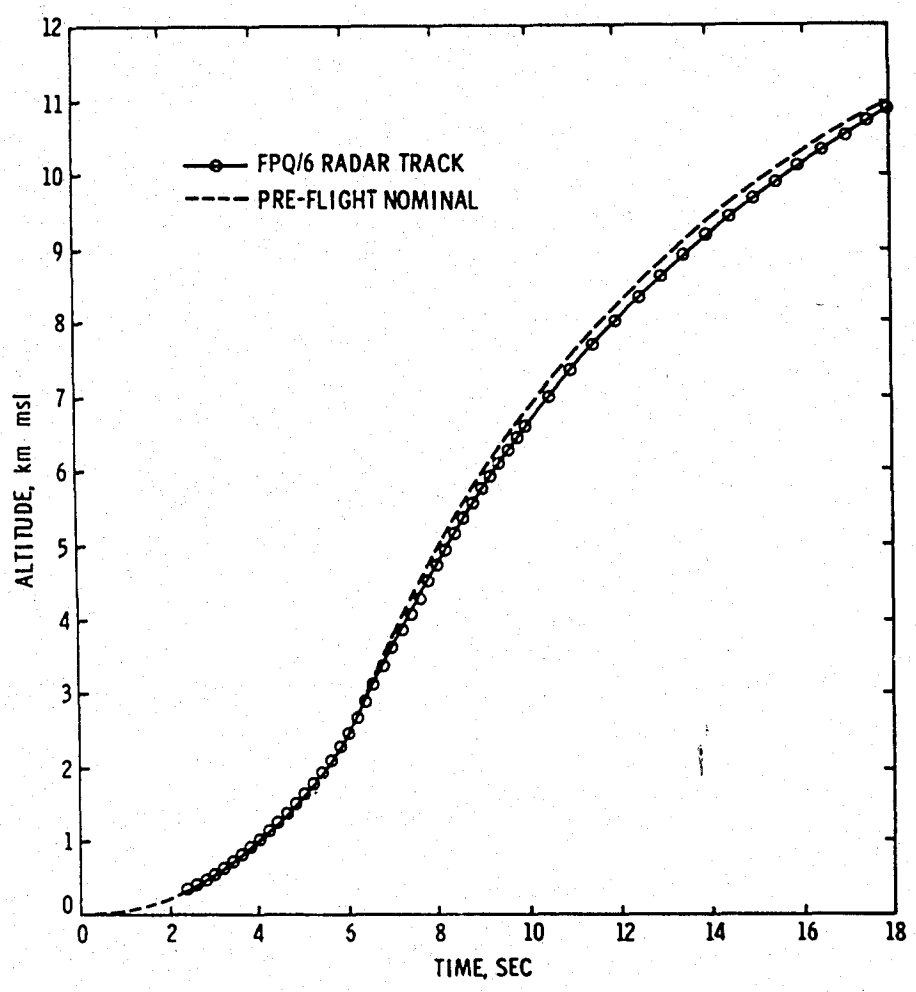

Figure E.2.2 Altitude Versus Time, Vehicle 5

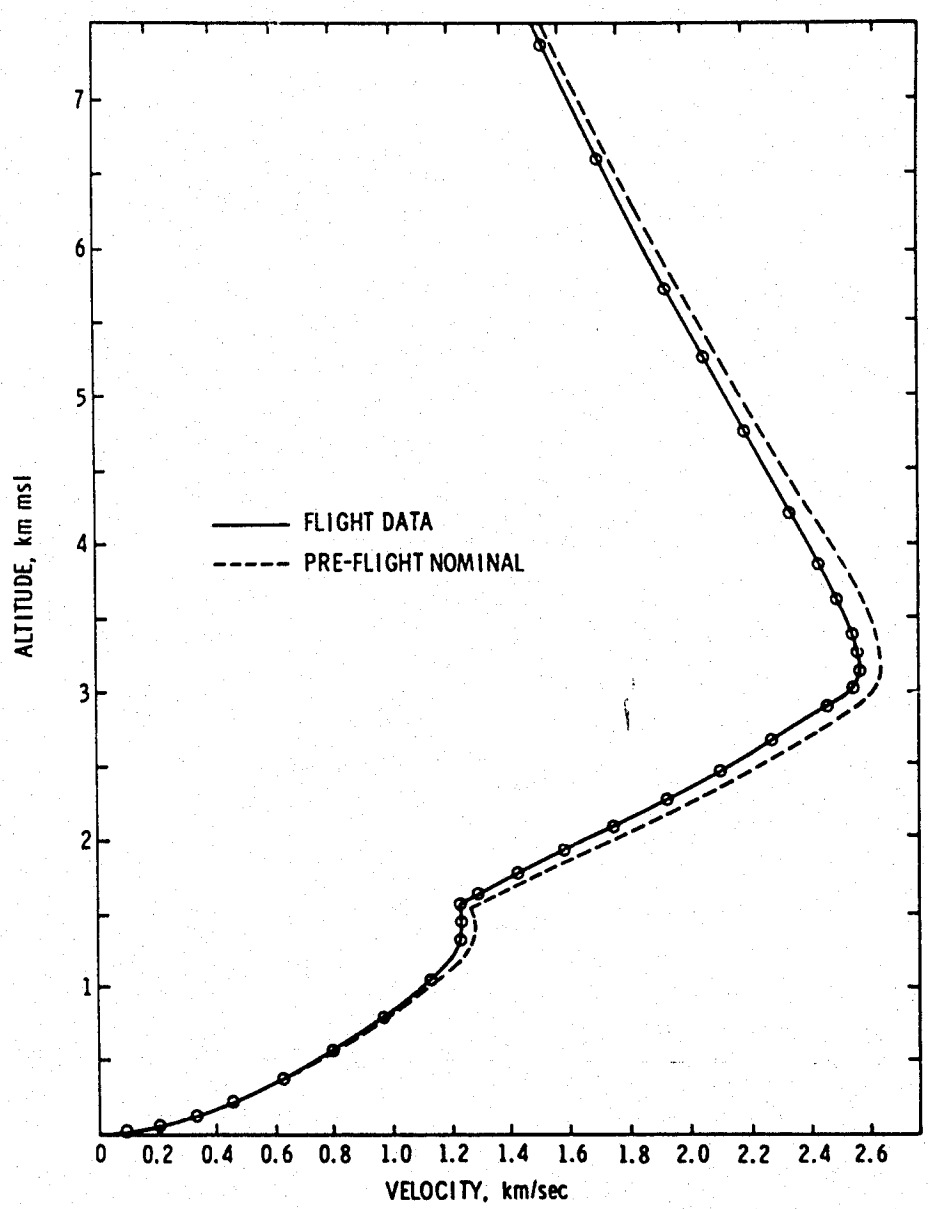

Figure E.2.3 Altitude-Velocity Profile, Vehicle 5

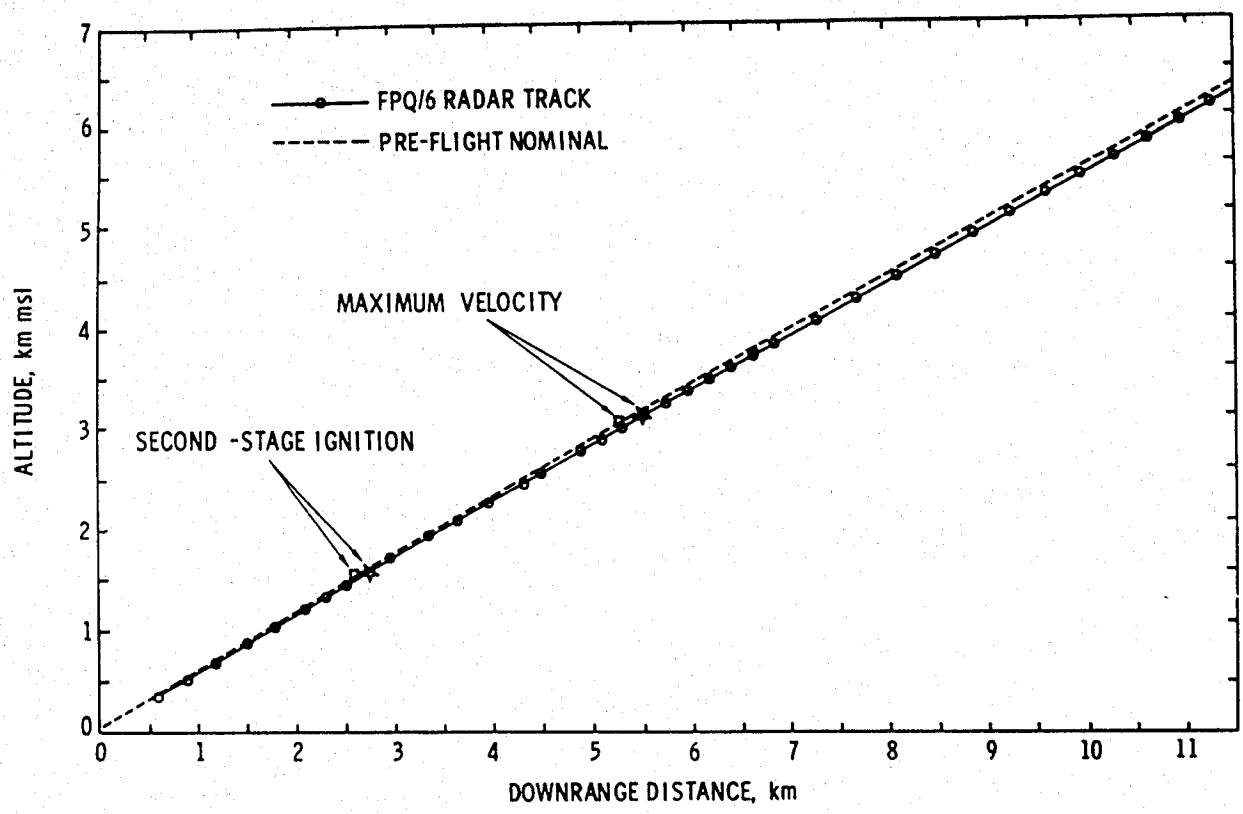

Figure E.2.4a Altitude-Distance Profile, Vehicle 5

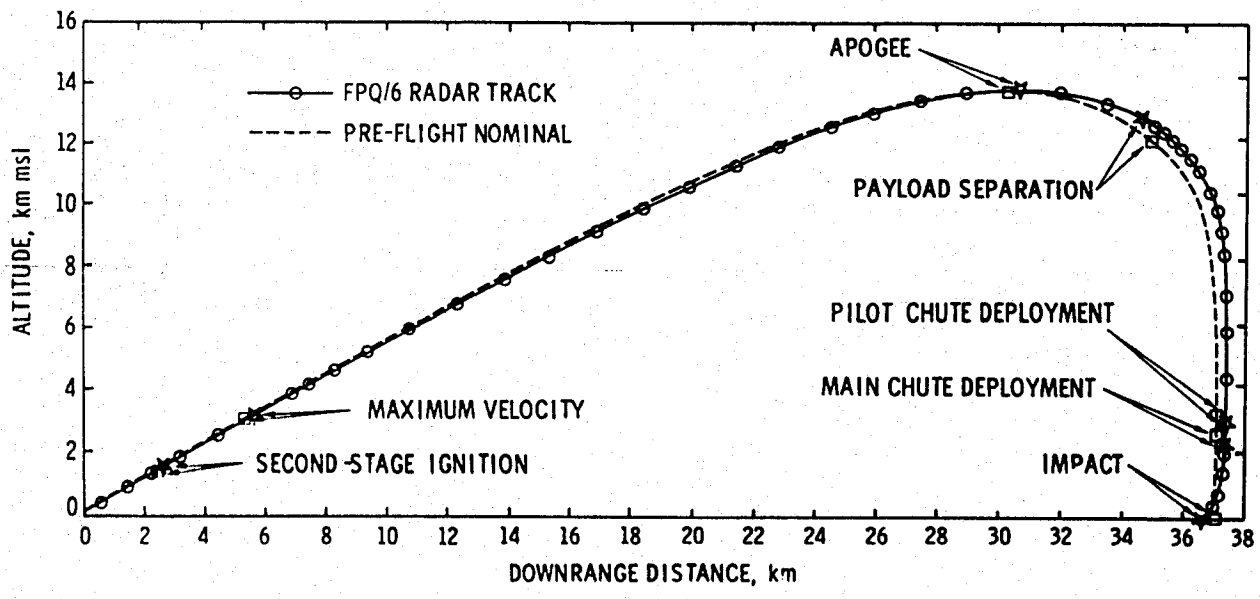

Figure E.2.4b Altitude-Distance Profile, Vehicle 5

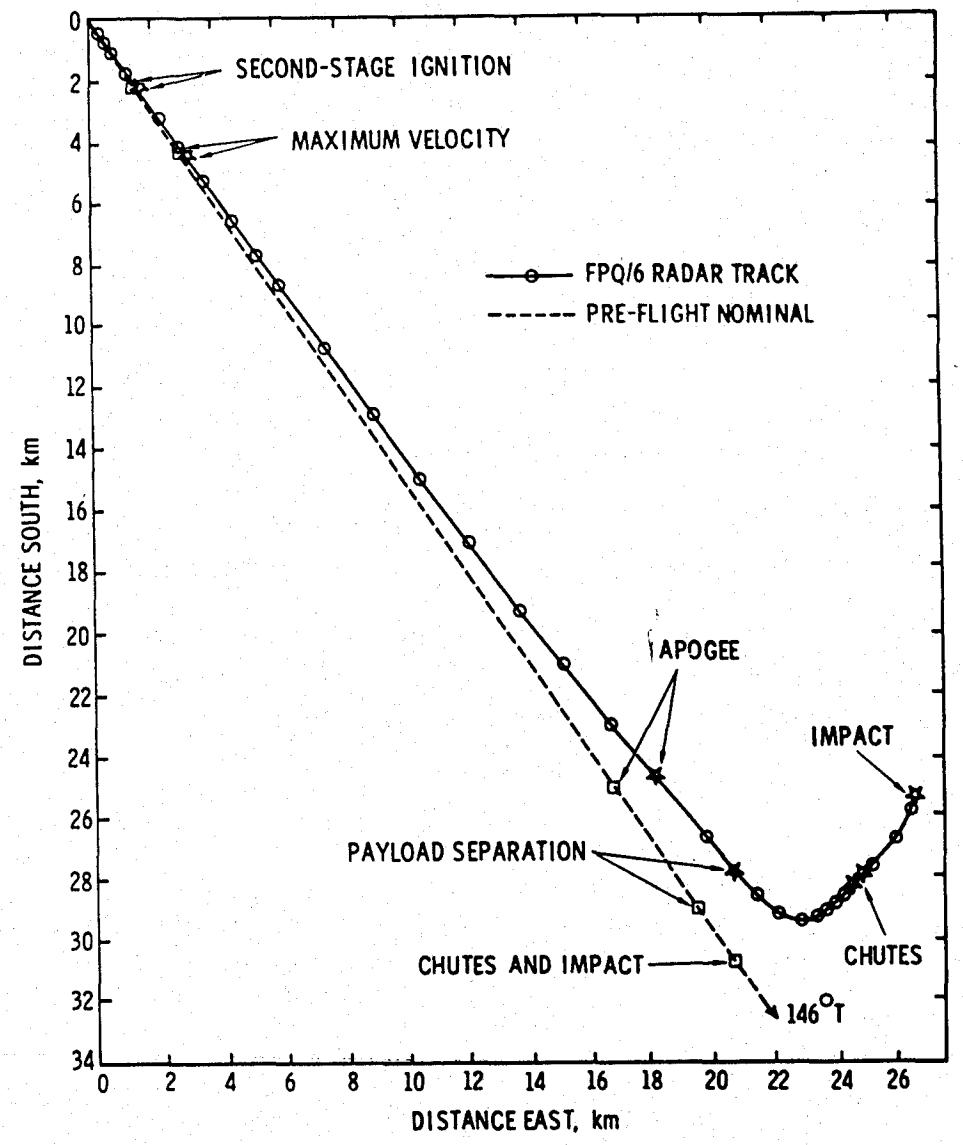

Figure E.2.5 Plan Position Track, Vehicle 5

TABLE E.2.1a

Vehicle 5 Trajectory Data

Time From T_o (sec)	Altitude (ft msl)	Velocity (ft/sec)	Ground Range (ft)
0.5	80	304	110
1.0	200	678	300
1.5	420	1,096	630
2.0	760	1,549	1,200
2.5	1,240	2,053	2,148
3.0	1,856	2,601	3,154
3.5	2,573	3,167	4,396
4.0	3,421	3,701	5,877
4.5	4,373	4,027	7,547
4.7	4,775	4,040	8,248
4.89	5,168	4,019	8,932
5.0	5,403	4,238	9,340
5.2	5,850	4,671	10,124
5.4	6,331	5,171	10,983
5.6	6,858	5,728	11,934
5.8	7,435	6,316	12,985
6.0	8,066	6,897	14,138
6.2	8,752	7,471	15,393
6.4	9,489	8,083	16,743
6.5	9,873	8,368	17,445
6.6	10,265	8,431	18,159
6.7	10,660	8,408	18,879
6.8	11,059	8,354	19,601
7.0	11,853	8,187	21,034
7.2	12,635	7,988	22,441
7.5	13,775	7,681	24,491
8.0	15,566	7,194	27,741
8.5	17,235	6,745	30,801
9.0	18,790	6,324	33,666
10.0	21,611	5,599	38,896
11.0	24,106	5,007	43,569
12.0	26,326	4,518	47,772
13.0	28,320	4,131	51,598
14.0	30,121	3,772	55,100
15.0	31,744	3,446	58,309
16.0	33,208	3,192	61,279
17.0	34,548	2,958	64,034
18.0	35,770	2,758	66,609
19.99	37,887	2,421	71,265

[redacted]

UNCLASSIFIED

TABLE E.2.1b

Vehicle 5 Trajectory Data

Time From T_o (sec)	Air Density ($lbsm/ft^3$)	Sound Speed (ft/sec)	Dynamic Pressure ($lbsf/f^2$)	Mach Number
.5	.07607	1107.	109.	.275
1.0	.07569	1108.	541.	.612
1.5	.07499	1109.	1400.	.988
2.0	.07391	1110.	2756.	1.395
2.5	.07266	1110.	4759.	1.850
3.0	.07140	1106.	7507.	2.352
3.5	.06986	1103.	10889.	2.871
4.0	.06809	1101.	14494.	3.361
4.5	.06618	1098.	16678.	3.666
4.7	.06538	1096.	16583.	3.686
4.89	.06462	1094.	16221.	3.674
5.0	.06420	1092.	17919.	3.881
5.2	.06338	1091.	21490.	4.281
5.4	.06248	1089.	25963.	4.748
5.6	.06149	1087.	31353.	5.270
5.8	.06032	1086.	37395.	5.816
6.0	.05901	1084.	43623.	6.363
6.2	.05770	1082.	50049.	6.905
6.4	.05634	1080.	57204.	7.484
6.5	.05565	1078.	60558.	7.763
6.6	.05495	1077	60700.	7.828
6.7	.05424	1076.	59590.	7.814
6.8	.05353	1075.	58057	7.771
7.0	.05215	1072.	54321.	7.637
7.2	.05090	1069.	50473.	7.472
7.5	.04991	1066.	44935.	7.205
8.0	.04642	1056.	37335.	6.813
8.5	.04375	1052.	30932.	6.412
9.0	.04156	1046.	25830.	6.046
10.	.03785	1033.	18440.	5.420
11.	.03487	1021.	13585.	4.904
12.	.03241	1009.	10281.	4.478
13.	.03030	999.	8036.	4.135
14.	.02852	988.	6306.	3.818
15.	.02702	977.	4986.	3.527
16.	.02562	969.	4057.	3.294
17.	.02429	964.	3303.	3.068
18.	.02292	965.	2709.	2.858
19.99	.02053	967.	1870.	2.504

UNCLASSIFIED

[redacted]

These differences from the nominal maximum velocity and the altitude of its occurrence were probably due to two primary factors. First, the booster-system performance was degraded by the prelaunch temperature of 10°C (50°F). Second, the Recruit booster contained 119.8 kg (264.2 lbs) of propellant, 1 percent less than a nominal Recruit motor. The azimuthal flight-path angle was 1.2 degrees left of the nominal. Analysis of the azimuthal flight-path angle deviation shows that approximately 0.3 degrees of the error can be attributed to the wind variation from the time of measurement until the vehicle launch.

E.3 Telemetry Measurements, Vehicle 5

Vehicle 5 was launched from the HAD launcher at Pad 0 at 1048:00 EST. The onset of the first-stage acceleration began at 1048:00.2 EST. The first-stage Terrier achieved a maximum acceleration of 36 g's at T+3.4 seconds. The vehicle deceleration reached a maximum of 8 g's before second-stage ignition. A maximum acceleration of 101 g's was attained at T+6.4 seconds during Recruit boost. A maximum vehicle deceleration of 32.9 g's was experienced at T+7.25 seconds. Figure E.3.1 shows the longitudinal acceleration history for the first 9.4 seconds of the test. Roll rate was not monitored on this vehicle, but the pitch and yaw rates indicated that the flight was normal.

Payload separation occurred at T+54.4 seconds. The baroswitch for initiation of the parachute recovery system began to close at T+123.35 seconds and closed completely by T+130.95 seconds. Pilot-parachute deployment occurred at T+143.3 seconds, and the main-parachute deployment at T+154.9 seconds. Loss of telemetry signal occurred at T+300.46 seconds, 1053:00.66 EST.

The temperature sensor located on the substructure of the Recruit stabilizing flare indicated a temperature of 116°C (241°F) before it malfunctioned at T+11.3 seconds. The other thermal sensors located in the recovery section, on the umbilical wall and on the transmitter experienced less than a 15°C (27°F) increase during the entire flight.

The TC564 stagnation point recession sensor functioned properly throughout the flight and indicated the removal of four radioactive sources between 6.35 and 9.15 seconds. The telemetered recession data for the stagnation point is shown in Figure E.3.2. The telemetry signal strength was adequate throughout the flight. Figure E.3.3 presents the telemetry signal strength history for the first 55 seconds of the test.

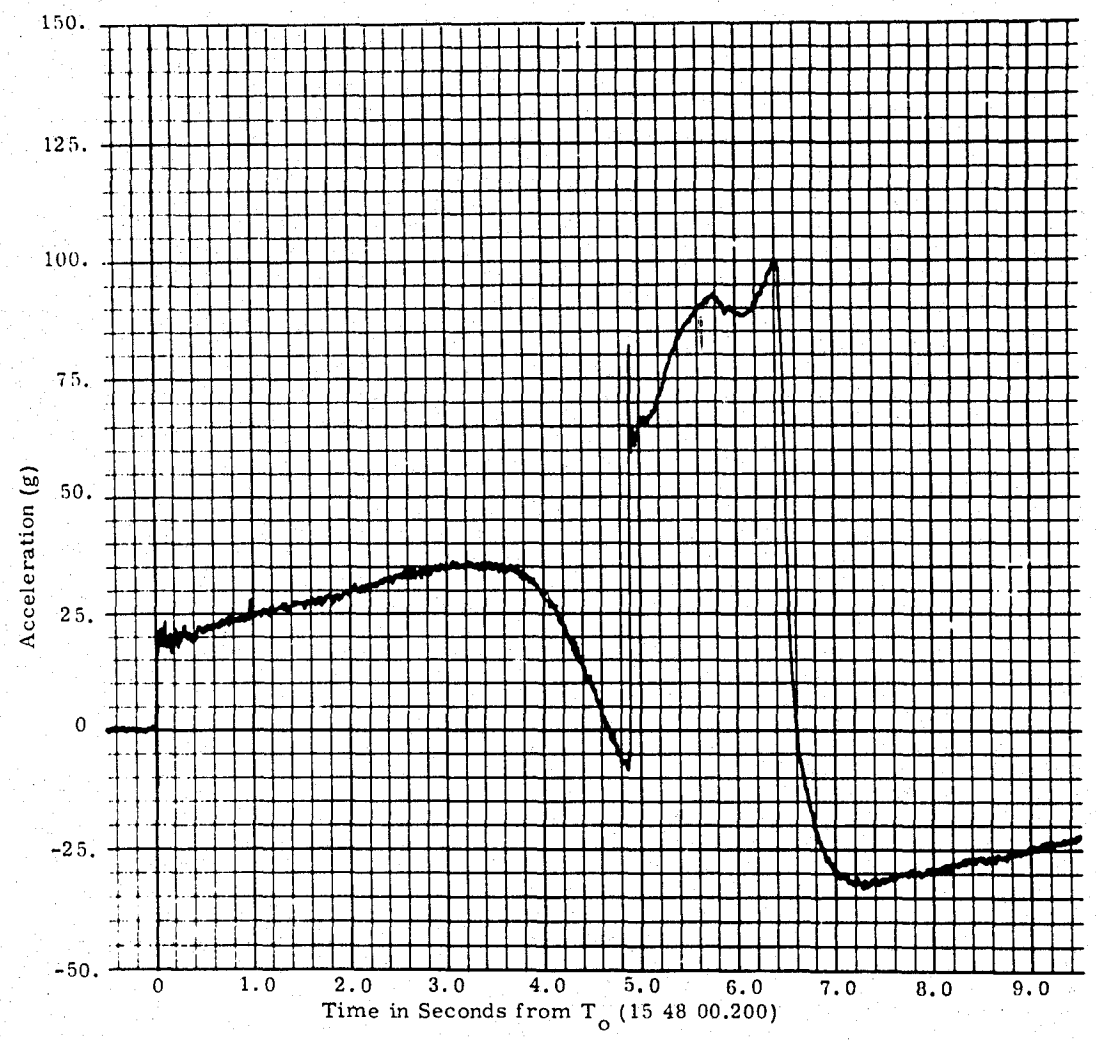

Figure E.3.1 Longitudinal Acceleration Versus Time, Vehicle 5

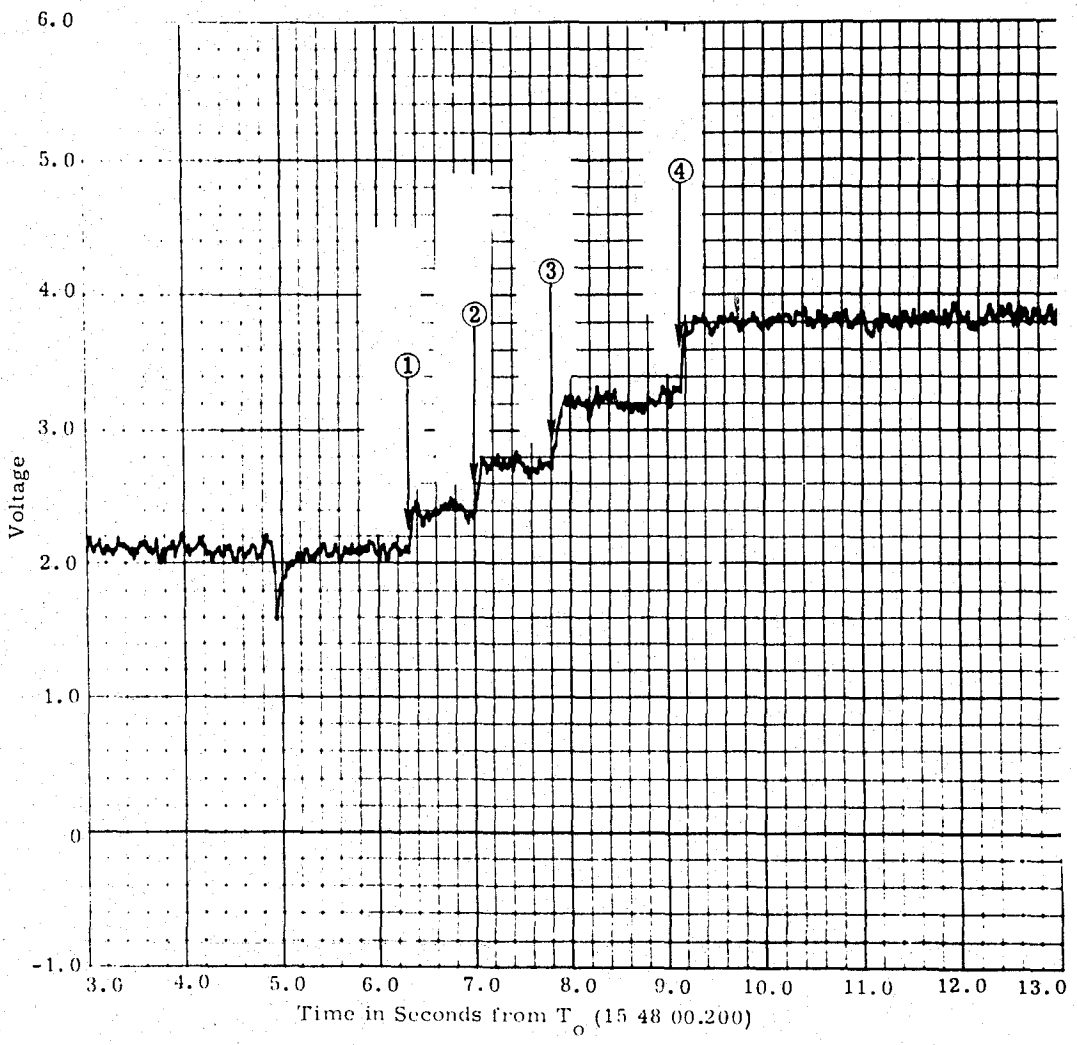

Figure E.3.2 Stagnation Point Recession Versus Time, Vehicle 5

[redacted]

UNCLASSIFIED

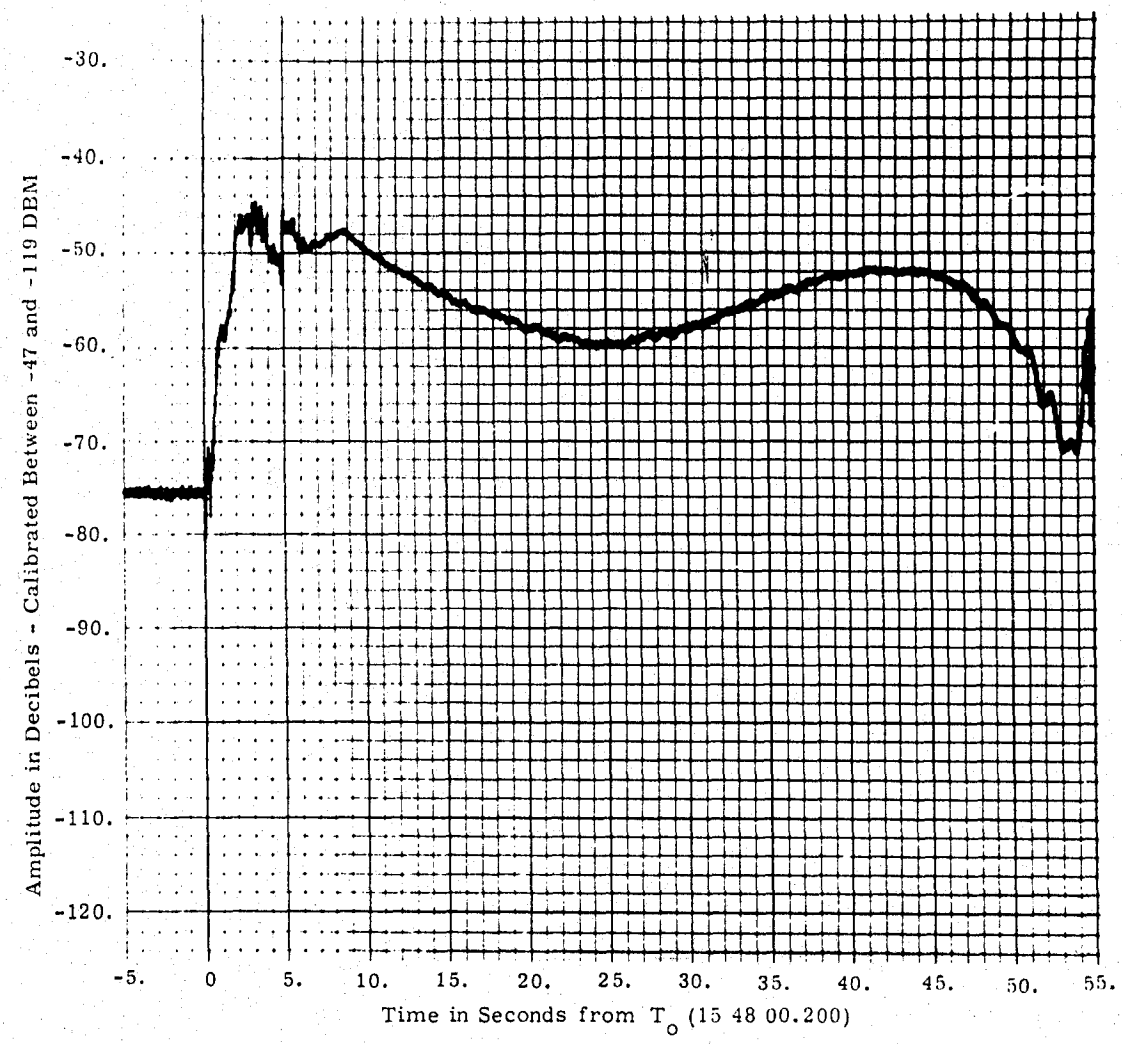

Figure E.3.3 Telemetry Signal Strength Versus Time, Vehicle 5

UNCLASSIFIED

[redacted]

[redacted]

(Intentionally left blank)

[redacted]

[redacted]

APPENDIX F

PRECIPITATION PARTICLE SIZE DISTRIBUTIONS

[redacted]

[redacted]

(Intentionally left blank)

[redacted]

APPENDIX F

PRECIPITATION PARTICLE SIZE DISTRIBUTIONS

An important input needed for estimating vehicle recession rate is knowledge of how the equivalent liquid-water content is distributed among the various precipitation particle sizes present. This section describes an approach used for specifying this distribution as a function of particle type and total liquid-water content.

Much has appeared in the literature on particle size distributions for precipitation; however, two articles, one for snow by Sekhon and Srivastava (1970) and one for rain, by Sekhon and Srivastava (1971) have proved most helpful in pointing out the interrelations among liquid-water content, radar reflectivity, mean diameter, precipitation rate, and number concentration by size or size distribution. The starting point for their treatment is that the average size distribution for raindrops is well represented by an exponential relation of the form

$$N_D = N_o e^{-\lambda D}$$

where $N_D \cdot \Delta D$ is the number of drops with diameters between D and $D + \Delta D$, and N_o and λ are parameters of the distribution. Marshall and Palmer (1948) had suggested that $N_o = 8000$ $(mm^{-1}m^{-3})$ and $\lambda = 4.1R^{-0.21}(mm^{-1})$ where R is rainfall rate in mm/hr. Gunn and Marshall (1958) had suggested that the same exponential distribution held well for aggregate snow but with $N_o = 3800\ R^{-0.87}$ and $\lambda = 2.55\ R^{-0.48}$, where D is now the melted diameter of snowflakes.

Sekhon and Srivastava (1971) gave the results of more recent radar rain data and suggested that $N_o = 7000\ R^{0.37}$ and $\lambda = 3.8\ R^{-0.14}$ was a more suitable fit for rain (note dependence of N_o on R). It was also shown that these parameters would vary somewhat depending on where the exponential distribution was truncated for both the low and high end. Cunningham (1972) calculated new parameters based on a somewhat different diameter distribution truncation value for snow, as well as producing some numbers for individual ice crystals. With these and the appropriate relations between rain rate R and liquid-water content $M(gm^{-3})$ a complete and consistent set of parameters can be described for the desired particle type.

For the rain-erosion flights of 1972 only three principal types of precipitation particles were specified by Cunningham and Plank (1972) as being present: (1) rain, (2) Cunningham aggregate snow, and (3) plane dendritic ice crystals. The following table summarizes all the parameters selected for describing the appropriate distribution.

TABLE F.1

List of Parameters for Particle Size Distributions*

$$N_o = aM^b \quad , \quad \lambda = cM^d \quad , \quad M = f\,R^g$$

Particle Type	a	b	c	d	f	g
Rain	23,000	0.40	2.5	-0.15	0.52	0.94
Snow	731	-1.1	1.21	-0.526	0.25	0.86
Crystals	41,840	-0.372	3.31	-0.343	0.406	0.887
MP Rain	8,000	0	2.2	-0.239	0.072	0.88

*$N_D = N_o e^{-\lambda D}$

In order to obtain the distribution of liquid-water content, or mass, by particle diameter, it is necessary to integrate the product of the number distribution function by the volume, or diameter cubed. In other words, the mass, M_{12} contained on diameters from D_1 through D_2 is

$$M_{12} = \frac{\pi\rho}{6} \int_{D_1}^{D_2} D^3 N_D \, dD$$

Integration of this expression results in a third-degree polynominal in λD evaluated at D_1 and D_2. However, it was considered simpler to evaluate numerically by desk calculator in the above form for various values of M encountered in the rain-erosion flights. Evaluation was performed by selecting 11 size classes between 0- and 5-mm diameter and assigning to each class an average diameter which was cubed and multiplied by the appropriate size class interval. This product was then multiplied by the proper N_D, which was calculated for each particle type and liquid-water content and summed for all size classes. The desired distribution was obtained by forming the fraction for each size class of $N_D D^3 \Delta D$ to the sum for all size classes.

Plots of the cumulative fraction are shown in Figures F.1, F.2, and F.3 for rain, snow and crystals, respectively, on log diameter-probability scales.

The curves graphically show how the liquid water (equivalent for ice) shifts to larger sizes as total mass increases. Also note that the shift is much greater for snow and ice than for rain. This is a result of the smaller fall rates and of the lesser dependence of fall rates on particle size for snow and ice than for rain.

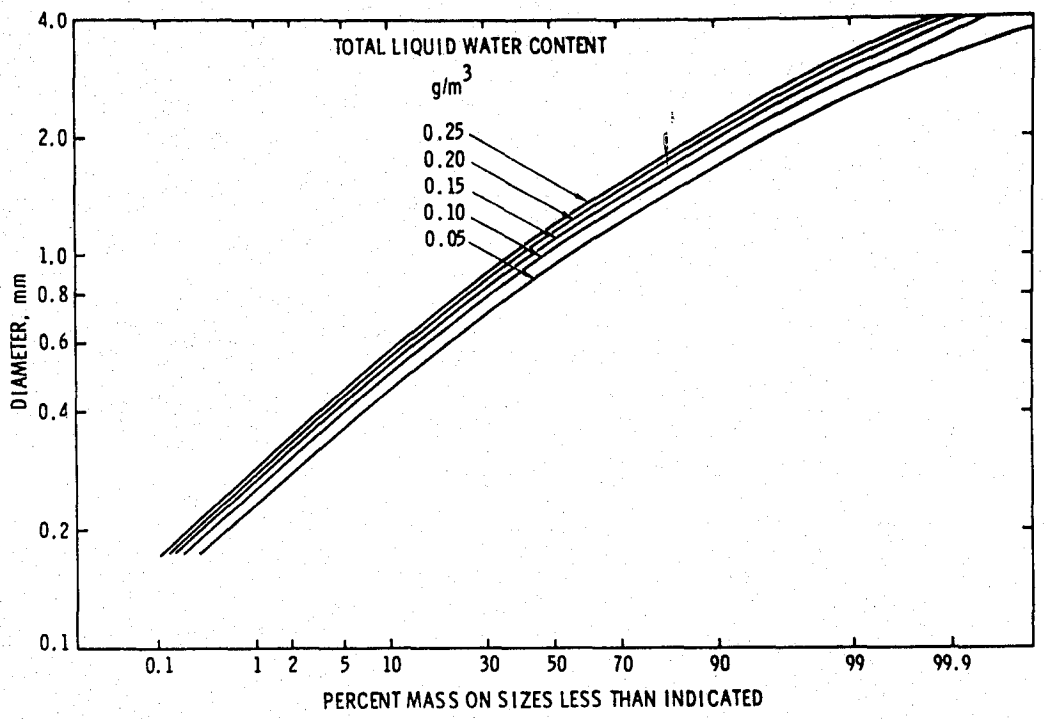

Figure F.1.1 Cumulative Mass Versus Size for Rain Drops

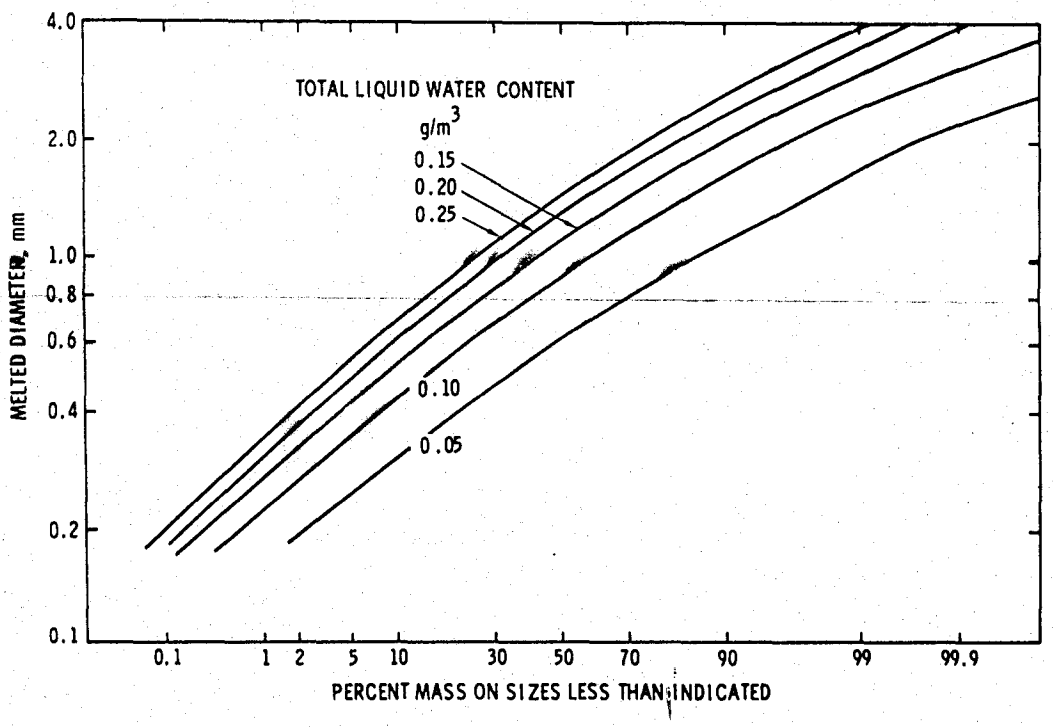

Figure F.1.2 Cumulative Mass Versus Size for Snow Flakes

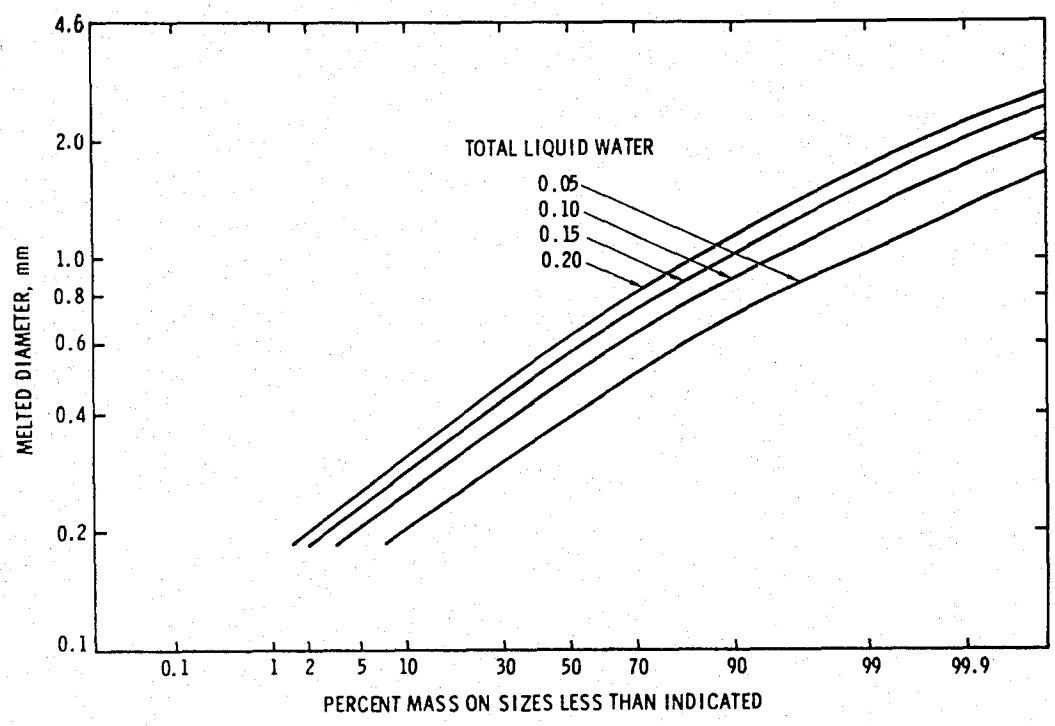

Figure F.1.3 Cumulative Mass Versus Size for Ice Crystals

[redacted]

APPENDIX G

COMPARISON OF REDUCED WEATHER RADAR DATA

[redacted]

[redacted]

(Intentionally left blank)

[redacted]

APPENDIX G

COMPARISON OF REDUCED WEATHER RADAR DATA

The JAFNA S-band radar reflectivities from spatial volumes of clouds and precipitation particles were recorded by two separate techniques. AFCRL photographically recorded the reflected power as displayed on cathode-ray tubes of the RHI (range height indicator) and A-scope (amplitude vs range). The reflected power data had been processed by a digital video integrator and contouring device described by Glover (1972).

Sandia made magnetic-tape analog recordings (dynamic response of 0-6 MHz) of the output from the log IF video amplifier of the radar. Also recorded on the tape were step calibration levels, range synchronization pulses, elevation angle, azimuth, time and voice channel of remarks. Relative timing was believed to be good to about 0.1 μs.

These tapes, containing signals analogous to A-scope displays, were later digitized at a 5-MHz rate (slightly oversampled since the transmitted pulse duration was 0.5 μs). Although the radar transmitted pulses at a rate of 960 Hz, only the returns from every fourth pulse, from 3 to 33 km range, were digitized in order to reduce the data handling to manageable proportions. This resulted in some 7 million digitized points per RHI scan (0° - 30° elevation). The data were further compressed by forming the average of the log of reflected power over a rectangular grid in horizontal range and altitude of 300 by 120 m, respectively, per grid point. This reduced the number of data points to 10^4. Before averaging, each reflected power value was normalized by $1/r^2$ to 1852 m (1 nmi) range.

Inspection of the individual values which went into making up the averages showed that the logs of the reflected power were typically distributed in a nearly Gaussian manner with a standard deviation of ~ 0.5 (5 db) or what amounts to a lognormal distribution of power with a geometric standard deviation of 3. Thus, in general, a quoted value of reflected power in dbm (decibels below one milliwatt) is made up of several hundred individual values within a 300-by-120-m box, with 68 percent of them lying within $\pm$ 5 db of the quoted value.

[redacted]

UNCLASSIFIED

BIBLIOGRAPHY

Cole, James K., SAMS Program Test Plan, SC-DR-70-850, Sandia Laboratories, December 1970.

Cole, J. K. and M. A. Ellis, SPLAT Computer Code for Prediction of Hydrometeor Impact Erosion on High-Speed Sphere-Cone Vehicles, SC-DR-70-373, Sandia Laboratories, August 1970.

Cole, J. K. and R. D. Robinett, Jr., December 1971, Test Report for SAMS Rain Erosion Flights I and II, SC-DR-71 0649, Sandia Laboratories, December 1971.

Cole, J. K., L. R. Rollstin, H. W. Church, and B. W. Marshall, Test Report for SAMS Rain Erosion Flights 6, 7, and 8, SLA-73-0813, Sandia Laboratories, to be published.

Cunningham, R. M., 1972 (private communication).

Cunningham, R. M. and V. G. Plank, "Interim Report on Environmental Definitions for the SAMS Program, 1971-1972," AFCRL, Bedford, Massachusetts, October 1972.

Glover, K. M., "A Precision Digital Video Integrator," in Proceedings of the Fifteenth Radar Meteorology Conference, American Meteorology Society, October 1972.

Gunn, K. L. S. and J. S. Marshall, "The Distribution with Size of Aggregate Snowflakes," J. Meteor. 15, 452-461, 1958.

Marshall, J. S. and W. McK. Palmer, "The Distribution of Raindrops with Size," J. Meteor., 5, 165-166, 1948.

National Aeronautics and Space Administration, Wallops Station Handbook, April 6, 1964.

National Center for Atmospheric Research, "Radar Atmospheric Research Facility," in Facilities for Atmospheric Research, No. 11, p. 16, December 1969.

Reinecke, W. G., W. L. McKay, and G. D. Waldman, Experiments and Analysis in High-Speed Erosion, AFML-TR-72-130, December 1972.

Riggan, W. C., TC564 Ablation Detector, SC-DR-70-730, Sandia Laboratories, December 1970.

Sekhon, R. S. and R. C. Srivastava, "Snow Size Spectra and Radar Reflectivity," J. Atmos. Sci., 27, 299-307, 1970.

Sekhon, R. S. and R. C. Srivastava, "Doppler Radar Observations of Drop-Size Distributions in a Thunderstorm," J. Atmos. Sci., 28, 983-994, 1971.

UNCLASSIFIED

[redacted]

DISTRIBUTION:

1/138A -	Acurex Corporation 485 Clyde Avenue Mountain View, CA 94040 Attn: Robert M. Kendall (1)	M3709
2-9/138A -	Aerospace Corporation P. O. Box 92957 Los Angeles, CA 90009 Attn: D. C. Glenn (6) R. A. Hartunian (1) R. B. Mortensen (1)	M4051
10-12/138A -	AVCO, Government Products Group 201 Lowell Street Wilmington, MA 01887 Attn: John M. Gilmore (1) Victor Dicristina (1) W. G. Reinecke (1)	M4072
13-15/138A -	General Electric Company Re-Entry Environmental Systems Division P. O. Box 7722 Philadelphia, PA 19101 Attn: Philip B. Cline (1) Robert J. Sullivan (1) J. Stewart (1)	M4034
16/138A -	Kaman Sciences Corporation 1500 Garden of the Gods Road Colorado Springs, CO 80907 Attn: Jerry L. Harper (1)	M1713
17-19/138A -	Lockheed Missile and Space Company, Inc. Division of Lockheed Aircraft Corporation P. O. Box 504 Synnyvale, CA 94088 Attn: Jerry E. Carlyle (1) J. O. Hedlund (1) D. Tellup (1)	M1056
20/138A -	Martin-Marietta Corporation Orlando Division P. O. Box 5837 Orlando, FL 32805 Attn: W. A. Gray (1)	M1761
21-22/138A -	McDonnell-Douglas Corporation 5301 Bolsa Avenue Huntington Beach, CA 92647 Attn: K. P. Kratsch (1) J. S. Murphy (1)	M3489
23-24/138A -	TRW Systems Group San Bernardino Operations P. O. Box 1310 San Bernardino, CA 92402 Attn: Leo Burger (1) A. L. Seward (1)	M3706

DISTRIBUTION (CONT):

25/138A -	TRW Systems Group One Space Park Redondo Beach, CA 90278 Attn: R. J. Myer (1)	M3761
26/138A -	ARO, Inc. Arnold AF Station, TN 37389 Attn: J. D. Whitfield E. E. Callens	M3123
27-29/138A -	Air Force Cambridge Research Laboratory L. G. Hanscom Field Bedford, MA 01730 Attn: M. L. Barad (1) R. M. Cunningham (1) K. J. Hardy (1)	
30/138A -	Air Force Materials Laboratory Wright-Patterson Air Force Base Dayton, Ohio 45433 Attn: G. F. Schmitt	M3660
31/138A -	Headquarters Air Force Systems Command Andrews AFB Washington, D.C. 20331 Attn: Maj. Lawrence J. Hillebrand (1)	M1766
32/138A -	Chief of Staff U. S. Air Force Washington, D.C. 20330 Attn: Maj. Lewis L. Tew (1)	M1521
33-38/138A -	Space and Missile Systems Organization P. O. Box 92960 Worldway Postal Center Los Angeles, CA 90009 Attn: Maj. Richard A. Rene (1) Capt. George R. Pisarczyk (5)	M3390
39/138A -	Air Force Weapons Laboratory Kirtland AFB, NM 87117 Attn: Charles Stein Scientific Support Branch DYX	M3743
40/138A -	Space and Missile Systems Organization Norton AFB, CA 92409 Attn: Capt. Larry J. Hudack (1)	M4100
41/138A -	Department of the Army Harry Diamond Laboratories Washington, D.C. 20438 Attn: James Gwaltney (1)	M4119
42/138A -	Director U.S. Army Ballistic Research Laboratories Aberdeen Proving Ground, MD 21005 Attn: Robert C. Tompkins (1)	M3742
43/138A -	Commander U.S. Army Material Command Washington, D.C. 20315 Attn: John J. Corrigan (1)	M0776

[redacted]

UNCLASSIFIED

DISTRIBUTION (CONT):

44-45/138A -	Commander U.S. Army Materials and Mechanics Research Center Watertown, MA 02172 Attn: Lewis R. Ananin (1) John F. Dignam (1)	M4048
46/138A -	Safeguard Systems Manager Safeguard Systems Office 1300 Wilson Blvd Arlington, VA 22209 Attn: Willis F. Teale (1)	M3318
47-48/138A -	Commander Naval Ordnance Laboratory Silver Spring, MD 20910 Attn: R. K. Lobb (1) W. C. Lyons, Jr. (1)	M1097
49/138A -	Commander Naval Ordnance Systems Command Headquarters Washington, D.C. 20360 Attn: Martin A. Kinna (1)	M0681
50/138A -	Chief of Naval Operations Navy Department Washington, D. C. 20350 Attn: R. Blaise (1)	M0770
51-52/138A -	Director Strategic Systems Project Office Crystal Mall No. 3 Washington, D.C. 20390 Attn: Marcus Meserole (1) H. A. McMasters (1)	M1409
53-54/138A -	Headquarters Defense Nuclear Agency Department of Defense Washington, D.C. 20307 Attn: J. A. Northrup (1) M. Rubenstein (1)	M0654
55-56/138A -	Director of Defense Research and Engineering Washington, D.C. 20301 Attn: Jerome Persh (1) Robert A. Moore (1)	M1946
57/138A -	NASA Ames Research Center Moffett Field, CA 94035 Attn: D. R. Chapman	M3291
58-59/138A -	NASA Langley Research Center Langley Station Hampton, VA 23365 Attn: R. L. Trimpi (1) R. T. Long, NASA Wallops (1)	M3684
60/138A -	Los Alamos Scientific Laboratory P. O. Box 1663 Los Alamos, NM 87544 Attn: L. D. P. King	M0737
61/138A -	U. S. Atomic Energy Commission Division of Military Applications Washington, D.C. 20545 Attn: D. McBride	M1163

UNCLASSIFIED [redacted]

DISTRIBUTION (CONT):

62/138A - University of California
Lawrence Livermore Laboratory
P. O. Box 808
Livermore, CA 94550
Attn: C. A. McDonald

M0828

63/138A - Morgan Sparks, 1
64/138A - W. J. Howard, 2
65/138A - G. A. Fowler, 1000
66/138A - W. A. Gardner, 1200
67/138A - J. C. Eckhart, 1250
68/138A - R. L. Peurifoy, 1500
69/138A - C. H. Mauney, 1530
70/138A - T. B. Lane, 1540
71/138A - V. E. Blake, Jr., 1550
72/138A - R. S. Claassen, 2400
73/138A - J. C. Crawford, 2410
74/138A - R. C. Dougherty, 2411
75/138A - D. B. Shuster, 4700
76/138A - R. G. Clem, 4730
77/138A - W. F. Roherty, 4731
78/138A - A. W. Snyder, 4760
79/138A - A. Narath, 5000
80/138A - O. E. Jones, 5100
81/138A - E. H. Beckner, 5200
82/138A - J. E. McDonald, 5300
83/138A - H. M. Stoller, 5310
84/138A - L. M. Berry, 5500
85/138A - A. Y. Pope, 5600
86/138A - R. C. Maydew, 5620
87/138A - E. C. Rightley, 5623
88/138A - W. R. Barton, 5624
89/138A - L. R. Rollstin, 5624
90/138A - H. R. Vaughn, 5625
91/138A - D. F. McVey, 5626
92/138A - S. McAlees, Jr., 5628
93/138A - K. J. Touryan, 5640
94/138A - R. A. Hill, 5642
95/138A - F. G. Blottner, 5643
96-100/138A - J. K. Cole, 5644 (5)
101/138A - H. W. Church, 5644
102/138A - C. W. Peterson, 5645
103/138A - J. H. Scott, 5700
104/138A - G. E. Brandvold, 5710
105/138A - M. L. Kramm, 5720
106/138A - R. D. Andreas, 5722
107/138A - H. W. Schmitt, 5723
108/138A - D. J. Rigali, 5725
109/138A - E. R. Frye, 7123
110/138A - T. B. Cook, Jr., 8000
111/138A - L. Gutierrez, 8100
112/138A - A. N. Blackwell, 8110
113/138A - A. R. Willis, 8111
114/138A - D. E. Gregson, 8150
115/138A - B. F. Murphey, 8300
116/138A - R. H. Meinken, 8310
117/138A - G. W. Anderson, Jr., 8330
118/138A - J. F. Barham, Jr., 8360
119/138A - G. R. Otey, 8362
120/138A - L. J. Paddison, 9300
121/138A - A. J. Clark, Jr., 9330
122/138A - F. W. Neilson, 9350
123/138A - R. L. Brin, 9410
124/138A - M. J. Navratil, 9415
125/138A - J. E. Stiegler, 9480
126/138A - M. V. Hereford, 9483
127-129/138A - Division 3151
For AEC/TIC (SNSI)
130-131/138A - Division 8266-2
132-138/138A - Division 3141